Study of the roles of two pore channels (TPCs) in metabolism

Doctoral Dissertation



Yuxuan Layla Zhang

Supervisor: Prof. John Parrington & Prof. Ming Lei

Worcester College

Department of Pharmacology

University of Oxford

Acknowledgements

On completion of this thesis, I owe a great deal of thanks to many people. First, I would like to thank my supervisor, Professor John Parrington, for offering me the position in this department to work with so many talented colleagues and for his mentorship throughout my DPhil to make this thesis possible. The experience during my DPhil has been a real privilege and I will be eternally grateful for having had this. I am also thankful to my second supervisor, Professor Ming Lei, for his kind advice and technical help.

I would like to thank Dr. Ali Hanbashi and Dr. Roshan Sahu for their hand-by-hand teaching about various techniques and experiments. I would also like to thank Dr. Ruth Tunn and Dr. Hayley Chan for their useful materials and kind help when I started my projects; many of the ideas in my study were greatly advanced by conversations with them. I would also like to pay extra special tribute to Professor Wei Huang and his group members for their kind collaboration in the Raman spectra experiments. In the same spirit, I would like to thank Prof. Jun Guo for kindly providing pseudo-virus. Particularly, I would like to thank Professor Jose Cancela for teaching me how to isolate cells, and Dr. Margarida Ruas and Dr. Pamela Lear for their kind advice which helped me decide the direction of my research. I am extremely appreciative to Professor Hong Yu for kindly letting me use her lab during the COVID-19 pandemic, and I would like to thank all members in her group for their kind advice and encouragement when I felt

frustrated. I would also like to express my thanks and appreciation to all my colleagues and my dear friends, Xuhui Jin, Faroq Kamli, Dr. Abeer Alharbi, Dr. Tianyi Sun, Zhiyu Qu, and Dr. Yunfang Yang, and for their warm company.

Personally, I would like to thank my parents and my grandparents for their unselfish love and support at every stage of my life. Words fail to express how lucky and proud I am to be your daughter and granddaughter. And I would like to thank my husband Dr. Chen Gong for his love and understanding all the time. I could not have achieved this without you by my side.

Abstract of thesis

Second messengers play roles in communication between and within cells and are critical in various physiological functions at cellular level. As an important second messenger, Ca^{2+}, through spatiotemporal changes in its cytosolic concentration in the cell, regulates multiple physiological processes. One source of cytosolic Ca^{2+} is the intracellular Ca^{2+} stores which mainly include the endoplasmic reticulum (ER) and the endolysosomal system. In past decades, research has identified the different triggers and mechanisms of Ca^{2+} release from different organelles. NAADP, as the most potent trigger, initiates Ca^{2+} release from the endolysosomal system, and there is evidence that two pore channels (TPCs), a type of cation channel located in endolysosomes, can mediate such Ca^{2+} release. Much previous research has successfully investigated the functions of TPCs in various physiological and pathological processes. In my studies, I have employed TPC gene-edited animal and cell models to investigate the function of TPCs in metabolism, particularly adipocyte differentiation, and pancreatic digestive enzyme secretion.

Obesity and related metabolic diseases have become a major problem; in the UK they are estimated to affect around 25% of adults and around 20% of children. Drug treatments with a minimum of adverse reactions could be an important tool alongside preventative measures. TPCs were investigated as a potential target for anti-obesity treatment in two different aspects: adipogenesis and lipid absorption. The studies were

based on unpublished evidence that Tpcn1-null mice are leaner with less lipid absorption in the intestine; also, the differentiation from mesenchymal stem cells to adipocytes in a Tpcn2 knock-down cell line is significantly reduced.

In this study I showed that pancreatic acinar cells isolated from Tpcn1-null mice have reduced lipase activity, and also that activities of other pancreatic enzymes are reduced. Moreover, Raman spectroscopy of Tpcn1/2 double-knockout pancreatic acinar cells show a reduction in the abundance of cytochrome C, which is the first study that connects TPCs with cytochrome C and should further lead to understanding of the relationship between TPCs and cell apoptosis. With regard to adipocyte differentiation, a shRNA knock-down mesenchymal stem cell model as well as preadipocytes isolated from Tpcn2-null mice showed reduced adipogenesis and the reduction seems to be led by an alteration in cyclic AMP signalling levels that induces Tpcn2 gene expression with calpain as a downstream modulator. In addition, hepatocytes isolated from Tpcn1-null mice were used as a model for SARS-CoV-2 pseudo-virus infection study, and the results showed that TPC1 may have functions in the infection of senile high-fat diet mice, and TPC1 may be regulating expression of TIMP-1 after infection.

The study of TPCs' role in lipid metabolism has expanded our understanding of this pathophysiological process and could lead to the identification of new therapeutic drug targets for anti-obesity treatment.

Publications during DPhil

1 **Zhang, Yuxuan** & Gong, Chen & Li, Dawei & Wang, Zhi-Wei & Pu, Shengda & Robertson, Alex & Yu, Hong & Parrington, John. (2021). A prognostic dynamic model applicable to infectious diseases providing easily visualized guides: a case study of COVID-19 in the UK. Scientific Reports. DOI: 10.1038/s41598-021-87882-9.

2 **Zhang, Yuxuan** & Chan, Lai-Hing & Tunn, Ruth & Ruas, Margarida & Gay, David & Todorcevic, Marijana & Christodoulides, Costas & Parrington, John. (2021). Two-pore channel 2 is a key regulator of adipocyte differentiation via the cAMP signalling pathway with calpain as downstream effector. (Preprint) DOI: 10.1101/2021.03.20.436264.

3 Alharbi, Abeer & **Zhang, Yuxuan** & Parrington, John. (2021). Deciphering the Role of Ca^{2+} Signalling in Cancer Metastasis: From the Bench to the Bedside. Cancers. DOI: 10.3390/cancers13020179.

4 Jin, Xuhui & **Zhang, Yuxuan** & Hanbashi, Ali & Alhoshani, Ali & Parrington, John. (2020). Targeting Two-Pore Channels: Current Progress and Future Challenges. Trends in Pharmacological Sciences. DOI: 10.1016/j.tips.2020.06.002.

5 Zhu, Lin & Xia, Chunyan & Wu, Lin & **Zhang, Yuxuan** & Liu, Junling & Chen,

Yinan & Liu, Jing & Xiao, Yongxin & Nie, Kai & Huang, Liyu & Qu, Ning & Yu, Hong. (2019). The critical role of RasGRP4 in the growth of diffuse large B cell lymphoma. Cell Communication and Signalling. DOI: 10.1186/s12964-019-0415-6.

Contents

Statement for author contribution 16

Experiments partly performed by collaborators. 16

Materials obtained from collaborators. 17

Chapter 1: Introduction 18

1.1 NAADP-triggered endolysosomal Ca^{2+} signalling. 18

1.1.1 Calcium distribution in the human body. 18

1.1.2 The function of Ca^{2+} as a secondary messenger in cells. 19

1.1.3 Intracellular calcium homeostasis. 21

1.1.4 How NAADP mediates intracellular Ca^{2+} mobilization. 24

1.2 Two pore channels. 28

1.2.1 Multifarious calcium channels in cells and how they work. 28

1.2.2 How TPCs were discovered, and how their cellular function was revealed. 30

1.2.3 Updates by recent research (structure and pharmacological regulation). 32

1.2.4 The roles of TPCs in various pathological processes. 33

1.2.5 Cognitive updates on TPCs and possible impact on the observations in this thesis. 35

1.2.6 The unsolved problems and possible future research directions. 38

1.3 Ca^{2+} signalling in metabolism. 41

1.3.1 Pancreatic digestive enzyme secretion. 41

1.3.2 Ca^{2+} signalling in adipocyte differentiation. 52

1.4 Intracellular Ca^{2+} signalling in virus infection with a particular focus on SARS-CoV-2. 67

1.4.1 The function of the Ca^{2+} signalling system in viral infection, particularly SARS-CoV-2 infection. 67

1.4.2 TPC-mediated endo-lysosomal Ca^{2+} signalling in virus infection, and its potential functions in COVID-19. 68

1.5 The aims, questions, and hypothesis before this study, and proposed solutions. 71

Chapter 2: Materials and Methods 74

2.1 Materials. 74

2.1.1 Animals. 74

2.1.2 TPC KO mice line. 74

2.1.3 High-fat-diet mice model establishment. 76

2.1.4 Culture of C3H10T1/2 cells. 77

2.1.5 Adipocyte differentiation of C3H10T1/2 cells. 77

2.1.6 Isolation, culture, and differentiation of primary preadipocyte cells. . 79

2.1.7 Primary mesenchymal stem cell isolation. 80

2.1.8 Hepatocyte isolation. 81

2.2 Cell transfection and infection. 81

2.2.1 Tpcn1 gene silencing (siRNA). 81

2.2.2 Lentiviral expression of TPC2. 83

2.2.3 Pseudo-virus (PSV) infection. 83

2.3 Cell staining. 85

2.3.1 Oil red O staining. 85

2.3.2 AdipoRed staining and quantification. 85

2.4 Proteomic analysis. 87

2.4.1 Pancreatic acinar cell protein extraction. 87

2.4.2 BCA method for determination of protein concentration. 87

2.4.3 Fluorescence and immunofluorescence imaging. 88

2.4.4 TIMP-1 expression level detection (Western Blot). 89

2.4.5 p-CREB and cytochrome c expression level detection (Western Blot). 90

2.4.6 iTRAQ and DIA proteomics and their data analysis. 91

2.4.7 Proteomics results analysis. 92

2.5 Other quantitative analysis. 93

2.5.1 Quantitative PCR analysis. 93

2.5.2 Tpcn2 level measurements (qPCR). 94

2.5.3 TD-NMR scanning for mice body composition. 95

2.5.4 Calpain activity analysis. 95

2.5.5 CREB phosphorylation analysis. 96

2.5.6 The quantified analysis of the activation of pancreatic lipase, elastase, and amylase. 97

2.5.7 Analysis of TPCN2 genetic variants in humans. 97

2.5.8 Single-Cell Raman Spectra (SCRS) measurements and data analysis. 98

2.6 Statistical analysis. 100

Chapter 3: The role of TPC1/2 in the secretion of digestive enzymes by the pancreas 101

3.1 Background and the aim of study. 101

3.2 Lipase activity is lower in Tpcn1 knockout pancreatic acinar cells. 103

3.3 Amylase and elastase activities are lower in Tpcn1 KO PACs. 106

3.4 Fatty acid β-oxidation is suppressed in Tpcn1 knockout pancreatic acinar cells. 109

3.6 Cytochrome C expression was suppressed in Tpcn1/2 DKO but not in TPC1 KO and WT pancreatic acinar cells. 119

3.7 LSM12 expression was suppressed in Tpcn1/2 DKO PAC and localized on the periphery of pancreatic acini. 125

3.8 Conclusion. 128

Chapter 4: The role of TPC2 in adipocyte differentiation 131

4.1 *Tpcn2* KO mice of both sexes have abnormal adipogenesis compared to wild type controls. 131

4.2 TPC2 mRNA expression is transiently up regulated during *in vitro* adipocyte differentiation. 135

4.3 TPC2 mRNA expression during adipocyte differentiation is up regulated by a cAMP signal. 138

4.4 TPC2 plays a functional role during adipocyte differentiation in vitro. 145

4.5 TPC2 regulation of adipocyte differentiation is mediated by calpain. 147

4.6 CREB phosphorylation during adipocyte differentiation is regulated by TPC2. 148

4.7 Genetic variation at the TPCN2 locus is associated with altered fat distribution. 155

4.8 Discussion and conclusion. 159

Chapter 5: The function of TPCs in SARS-CoV-2 pseudo-virus infection of hepatocytes..... 165

5.1 Expression level of Tpcn1 and Tpcn2 in SARS-CoV-2 pseudo-virus infected senile female hepatocytes. 165

5.2 Pseudo-virus infected hepatocytes from female senile mice on a high-fat-diet show higher Tpcn2 mRNA levels. 169

5.3 Previous research has shown that TIMP1 plays an important role in SARS-CoV-2 infection. 171

5.4 Pseudo-virus infection triggered TIMP1 up-regulation which was rescued by

Tpcn1 KD in hepatocytes.....174

5.5 Discussion.....177

Chapter 6: Conclusion and future work.....182

6.1 Conclusion.....182

6.2 Future work.....187

References.....189

Supplementary Materials.....214

Statement about author contribution

In this study, some of the work was obtained by working in collaboration with colleagues and collaborators which is listed as below. All collaborators were informed and allowed the data and figures to be presented in this thesis.

Experiments partly performed by collaborators.

Raman Spectroscopy (Figure 18-20) was conducted in collaboration with Dr. Jiabao Xu from the Department of Engineering, University of Oxford. The instrument operation and data collection were done by Dr. Xu (60%). The sample preparation and data processing (including plotting) were done by Yuxuan Zhang (40%).

Some of the preliminary mice work in Chapter 4 was done by Dr. Ruth Tunn and Dr. Hayley Chan who studied as DPhil students before 2018 in the Department of Pharmacology, University of Oxford. The body mass and fat mass detection by TD-NMR (Figure 25, 26), as well as the intraperitoneal glucose tolerance test (IPGTT) (Figure 27) were conducted by Dr. Tunn (100%). The mRNA levels of adipogenic marker genes in C3H10T1/2 cells (Figure 29) were firstly measured by Dr. Chan (60%) but were repeated by Yuxuan Zhang (40%).

The human TPCN2 biostatistical study was conducted in collaboration with Dr. Marijana Todorcevic from the Oxford Centre for Diabetes, Endocrinology and

Metabolism, University of Oxford. The database access, data analysis and plotting were done by Dr. Todorcevic (100%).

Materials obtained from collaborators.

High-fat diet mice fed on a combined diet with the addition of both fat and cholesterol, used for primary hepatocyte isolation in Chapter 5, were obtained from Dr. Kai Nie from Shanghai Chest Hospital, Shanghai Jiaotong University. The mice model was 100% established and maintained by Dr. Nie.

The TPC gene-edited mice line, used for pancreatic acinar cell isolation, and preadipocyte isolation in Chapter 3 and 4, was established by Dr. Margarida Ruas from the Department of Pharmacology, University of Oxford. The mice line was established by Dr. Ruas (50%) by Cre-loxP and maintained by group members in our lab (50%): Dr. Roshan Sahu (30%), Dr. Ali Hanbashi (30%), Faroq Kamli (20%) and Yuxuan Zhang (20%).

Pseudo virus (SARS-Cov-2), used for cell infection in Chapter 5, was obtained from Dr. Shi-Hao Zhou from the Central China Normal University. The pseudo virus was composed and GFP-tagged by Dr. Zhou.

Chapter 1: Introduction

1.1 NAADP-triggered endolysosomal Ca^{2+} signalling.

1.1.1 Calcium distribution in the human body.

Normally, calcium content in the adult human body is 700-1500 g, accounting for 1.5%-2.2% of body weight, and calcium content in men is higher than in women. 99% of the calcium is in the form of bone mineral salts in bones and teeth. The main component of bone salt crystals is hydroxyapatite, in which the ratio of phosphorus to calcium is 6:10. About 1% of calcium in the human body is often in the free or combined ion state in soft tissue, extracellular fluid, and peripheral blood, collectively known as the miscible calcium pool.

The miscible calcium pool maintains a dynamic balance with the calcium in the bone, that is the calcium in the bone is continuously released from the osteoclasts into the miscible calcium pool, and the calcium in the miscible calcium pool is continuously deposited into the osteoblasts in the form of "bone salts".

In mammals, almost all physiological activities are regulated by miscible calcium (Ca^{2+}); indeed, it is possible that Ca^{2+} is the most pervasive signalling molecule in organisms. The basis of Ca^{2+} as a cellular messenger is that there exist concentration

gradients between cytoplasmic Ca^{2+}, intracellular Ca^{2+} stores, and extracellular Ca^{2+}. When a certain stimulus causes a substantial increase in intracellular Ca^{2+} concentration, it plays a role in transmitting signals. The molecular properties of Ca^{2+} itself are very conducive to binding to target proteins and thus transmitting information between the internal and external aspects of cells.[1]

Due to its rich variety of functionality, Ca^{2+} signalling must be very flexible and, at the same time, it must be subject to strict regulation and control. Therefore, Ca^{2+} signals at different times may have different intermediaries and play different roles. In addition, different types of cells, or cells in different tissues, use different combinations of Ca^{2+} signals to perform their specific physiological functions. All of this makes Ca^{2+} signalling a very complex and diverse system of physiological and biochemical reactions.[2]

1.1.2 The function of Ca^{2+} as a secondary messenger in cells.

Information transduction between cells in mammals can be achieved through direct contact, but in most cases the information is transduced through the secretion of information substances by cells which regulate functions of their own and other cells, and this process is called cell signalling. The information substances which initiate cell signalling are called messengers.[3]

Information substances can be divided into intercellular information substances and

intracellular information molecules. Chemicals secreted by cells to regulate the activities of target cells are referred to as intercellular message substances, that is, the first messenger. First messengers include neurotransmitters, endocrine hormones, local chemical mediators, and gas signalling molecules. The chemicals that transmit cellular regulatory signals within the cell are called intracellular information molecules, that is, the second messenger. Second messengers are usually small molecular agents such as Ca^{2+}, cAMP, cGMP, diacylglycerol (DAG), inositol 1,4,5-trisphosphate (IP_3) and arachidonic acid. Substances responsible for the transmission of information inside and outside the nucleus are called third messengers, which can bind to specific sequences of target genes and play the role of transcription factors or transcription regulatory factors.[4]

Ca^{2+} is one of the second messengers that are important components in the initiation of cell signalling. But unlike other messengers which are secreted or destroyed during cell signalling, Ca^{2+} changes its concentration to play its role by moving around, inside and outside of cells, via transporters or through calcium channels.[1] There are generally two action modes of Ca^{2+} as a second messenger. One is direct action, for example, Ca^{2+} directly combines with troponin in skeletal muscle to cause muscle contraction. Another is via an indirect effect, this being the main action mode in the induction of phosphorylation of a series of proteins by activating protein kinases, and ultimately causing cellular effects.[5,6]

As a key modulator of cellular processes, Ca^{2+} is crucial in regulating cell growth, cell development, cell survival, and other basic cell functions. Such regulating effects of Ca^{2+} signalling have been elaborately studied during the past few decades, for example, Ca^{2+} signalling through the TRP/Orai pathway has been shown to play vital roles in programmed cell death processes such as autophagy, which plays a role in a spectrum of pathological neurodegenerative diseases including Alzheimer's, Parkinson's, and Huntington's diseases.[7] There are also many studies showing that Ca^{2+} flux from mitochondria plays a bioenergetic role in metabolism-secretion coupling in pancreatic β-cells.[8]

1.1.3 Intracellular calcium homeostasis.

Cytosolic calcium usually exists in two forms which are calcium in its bound state and calcium in its free ionic state (Ca^{2+}). Without stimulation, the concentration of Ca^{2+} in mammalian cells is quite low, about 10^{-7} mol/L, while the extracellular Ca^{2+} concentration is 10^{-3} mol/L, which means there is a concentration difference of 10^4 times. Meanwhile, in some organelles including mitochondria, endolysosomes, and the endoplasmic reticulum (ER), the Ca^{2+} concentrations can be as high as 10^{-3} mol/L, which is thousands of times higher than in the cytoplasm, which is why they are named intracellular calcium pools.[2] The ER is the main intracellular calcium store since it accounts for 90% of the total volume of the organelles storing intracellular Ca^{2+}, while other acidic organelles account for 10%.[9] Therefore, there are two main sources of

cytosolic Ca^{2+}, which are almost infinite extracellular Ca^{2+} and finite Ca^{2+} from intracellular calcium pools. The homeostasis among Ca^{2+} in the extracellular matrix, cytosolic Ca^{2+}, and Ca^{2+} in intracellular stores is very delicate (Figure 1).

Ca^{2+} enters the cell in three ways, which are the voltage operated calcium channel (VOC), receptor operated calcium channel (ROC), and store operated calcium entry (SOCE). As well as VOC and ROC which initiate a mass of Ca^{2+} influx in a short time, SOCE produces a tiny but continuous Ca^{2+} influx. SOCE is regulated by the filling state of intracellular calcium stores. It is activated when the concentration of Ca^{2+} in the ER is reduced. Studies in the past 15 years have confirmed Orai proteins as a primary component of SOCE. When the Ca^{2+} concentration drops in the ER, STIM proteins start to accumulate at ER-plasma membrane (PM) junctions, and these STIM proteins activate Orai channels to allow Ca^{2+} influx.[10]

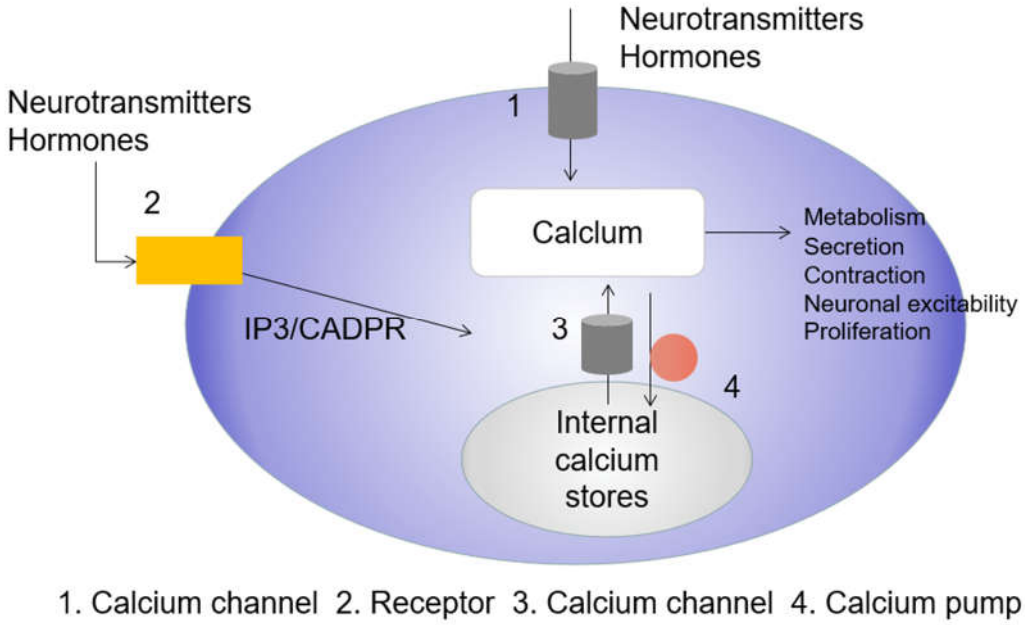


Figure 1. Calcium homeostasis achieved by calcium flux from extracellular matrix and internal calcium stores through four ways which are calcium channel, hormone receptor, internal calcium channel, and calcium pump.

Another source of cytosolic Ca^{2+} is the intracellular calcium stores which include mitochondria, the ER/SR, and endolysosomes. Two typical Ca^{2+} release channels on the ER intracellular calcium store are ryanodine receptors (RyRs) and IP_3 receptors (IP_3Rs), which mediate Ca^{2+} flux from the ER to the cytoplasm and are regulated by Ca^{2+}. When the Ca^{2+} concentration is enhanced in intracellular stores, the channels are more sensitive to Ca^{2+}, and thus tend to open and allow Ca^{2+} outflow.[11] In contrast, when the Ca^{2+} concentration is enhanced in the cytosol, the channels inhibit the liberation of Ca^{2+} from the intracellular organelles to ensure that the cytosolic Ca^{2+} is

enough to trigger cellular functions while not destroying the cells. The above mechanism is named calcium-induced calcium release (CICR).[11] In addition, RyRs and IP_3Rs are also activated by depolarization of the plasma membrane and IP_3, respectively.[12] IP_3 is a secondary messenger itself, that is why it can directly trigger Ca^{2+} release, however, in normal physiological condition, the amount of IP_3 is not high enough to trigger Ca^{2+} release; alternatively, IP_3 makes IP_3Rs more sensitive to Ca^{2+} so that signalling is facilitated.[13] Similar mechanisms exist for RyRs; cyclic adenosine diphosphate ribose (cADPR), which is a metabolite of nicotinamide adenine dinucleotide (NAD^+), makes RyRs more sensitive to Ca^{2+} and thus mediates Ca^{2+} mobilization.[14] Initially NAD^+ was recognized as the key messenger for RyR and IP_3 mediated CICR, however, researchers found that there was a prominent delay in the Ca^{2+} mobilization by NAD^+, and this delay was confirmed as due to an enzymatic conversion from NAD^+ to cADPR which is the direct Ca^{2+} mobilizer, by ADP-ribosyl cyclases.[15]

1.1.4 How NAADP mediates intracellular Ca^{2+} mobilization.

Similar to IP_3 and cADPR, nicotinic acid adenine dinucleotide phosphate (NAADP) is a Ca^{2+} mobilizing messenger which triggers Ca^{2+} flux from intracellular stores. Like cADPR, NAADP is another metabolite of NAD^+ in a set of oxidation-reduction reactions.

The discovery of NAADP was accidental. When researchers used NAD^+ to trigger Ca^{2+} release, they found a prominent delay, and as previously mentioned, we now know that this is because of cADPR production. However, when researchers used nicotinamide adenine dinucleotide phosphate (NADP) to trigger Ca^{2+} release, they found that Ca^{2+} signals happened instantaneously, and after chromatographical resolution, they identified NAADP, which is an alkaline derivative of NADP, as the molecule that actually triggers that instantaneous Ca^{2+} release.[15,16]

NAADP was first discovered using the sea urchin egg homogenate system and its action has subsequently been shown in a wide variety of multicellular organisms indicating its generality. NAADP was recognized to mobilize intracellular Ca^{2+} signals independently, although in many cases, it interacts with IP_3 and cADPR in mobilizing cytosolic Ca^{2+} signals.[16,17] Compared to IP_3 and cADPR, NAADP is more potent in triggering Ca^{2+} release from intracellular stores with an EC50 of 30nM.[18] In addition, as a CICR mediator, NAADP is more sensitive to Ca^{2+}.

There has been some controversy about whether RyR is the key downstream mediator of NAADP for Ca^{2+} mobilization. In some cell models such as myocardial cells and skeletal muscle cells, NAADP seems to directly activate RyRs in lipid planar bilayers and release Ca^{2+} from intracellular stores.[19] However this conclusion was challenged by findings in pancreatic acinar cells showing that NAADP triggers Ca^{2+} release from lysosomes, with this Ca^{2+} subsequently triggering CICR through RyRs.[20] In contrast a

study in 2003 showed that the NAADP triggered Ca^{2+} release was through a certain binding protein which acted on RyRs.[21] However, the identity of such a binding protein remained unconfirmed. In addition, RyR was shown to be irresponsive to NAADP stimulation in HEK cells.[22] Today a general conclusion is that in pancreatic acinar cells and many other cell types, NAADP tends to release Ca^{2+} from the endolysosomal system through two-pore channels (TPC), while it tends to release Ca^{2+} from the ER/SR through direct or indirect activation of RyRs.

The two pore channels (TPCs), which are the core objective of my research, are located on the acidic endolysosomal stores and were confirmed to mobilize Ca^{2+} release triggered by NAADP.[23,24] However a contrasting view has emerged in recent years that TPCs are actually Na^{+} channels activated by phosphatidyl inositol 3,5-bisphosphate instead of Ca^{2+} channels activated by NAADP.[25,26] Yet the physiological evidence that genetically editing TPCs results in weakened Ca^{2+} mobilization triggered by NAADP cannot be ignored.[23]

A still partially unsolved question about NAADP and TPCs is whether NAADP directly activates TPCs. Currently, the activation of TPCs by NAADP is thought to be indirect. This conclusion is based on studies that used isotope labelled or photoaffinity labelled NAADP to identify the binding protein through which NAADP activates TPCs. Such binding proteins were only identified recently and in general the activation process in various cell types seems very complex.[27,28] Jupiter microtubule-associated homolog 2

(JPT2) was shown to interact with TPC1 and is essential for NAADP-evoked Ca^{2+} signalling in the HEK293 cell line.[29] In addition, an Sm-like protein LSM12 was shown to be necessary for TPC activation by NAADP.[30] However the specific and detailed mechanisms involved in the activation of TPCs by NAADP remain far from clear.

1.2 Two pore channels.

1.2.1 Multifarious calcium channels in cells and how they work.

Essentially, cation channels are passages for ions such as Na^+, K^+, and Ca^{2+} in intracellular milieu and extracellular fluid to cross the lipid barriers of the plasma membrane and the membranes of intracellular organelles.[31] Calcium channels exist in a wide variety of forms, in various types of cells in organisms, regulating the transport of Ca^{2+}. Calcium channels are transmembrane glycoproteins that form a funnel-like hydrophilic pore that acts as a selective valve for calcium ions.

In Ca^{2+} homeostatic regulation, Ca^{2+} flows into the cytosol from either the extracellular matrix or from intracellular stores. The calcium channels can be classified according to their location, thus there are calcium channels in plasma membranes and calcium channels on intracellular Ca^{2+} stores. Calcium channels in plasma membranes are generally considered to be of two types, which are voltage-dependent calcium channels (VDC) and receptor-operated calcium channels (ROC).

VDCs are transmembrane heterogeneous polymer proteins located in the plasma membrane, and their opening is voltage dependent. They are further divided into L, T, and N subtypes according to their conductivity and sensitivity to voltage. The membrane potential required for the opening of different VDCs is different, and the

cellular effects mediated by Ca^{2+} flowing through each subtype are also different.[32] The long-lasting calcium channel (L-type Ca^{2+} channel) has the most pharmacological significance. Its activation potential is -10 mV and it requires strong depolarization for activation. After activation, the channel opens for a long time and deactivates slowly, which makes L-type calcium channels the main pathway for Ca^{2+} to flow into cells during cell excitation. L-type Ca^{2+} channels exist widely in all kinds of cells, especially cardiac muscle and cardiovascular smooth muscle cells, and are functionally closely related to excitation-contractile coupling and excitation-secretory coupling.[33] The transient calcium channel (T-type Ca^{2+} channel) activation potential is -70mV, and strong depolarization is not required for its activation. The duration of opening after activation is short and the deactivation is fast. It mainly exists in myocardium, neurons, and vascular smooth muscle cells, participates in pacing activity and repeated release of myocardial sinoatrial node and neurons, maintains cell automaticity, is related to transmembrane movement of Ca^{2+} at low membrane potential (close to resting membrane potential), and regulates cell growth and proliferation. The neuronal calcium channel (N-type Ca^{2+} channel) can be activated under strong depolarization, and the deactivation rate is moderate. N-type Ca^{2+} channels are found only in nervous tissues, and they mainly trigger the release of neural transmitters.[32,34]

The receptor-operated calcium channel (ROC) is coupled with receptors on the plasma membrane. When specific receptor agonists bind to the receptor, the ROC opens

directly, and its opening is independent of changes in membrane voltage. ROC exists widely in different tissues and is involved in platelet aggregation, vasoconstriction, nitric oxide (NO) release, pain conduction, and glandular secretion.[35]

Ca^{2+} flux from intracellular stores is through Ca^{2+} channels on acidic organelles; such Ca^{2+} channels include SERCA which is an ATP-dependent cationic transporter, and two pore channel (TPC) which is a cation channel on endolysosome system and mobilizes Ca^{2+} release activated by complex mechanisms with the participation of NAADP.[36]

1.2.2 How TPCs were discovered, and how their cellular function was revealed.

Two pore channel (TPC) was first discovered in rat kidney in 2000. It contains two domains, and each domain includes six transmembrane segments found in voltage gated Ca^{2+} and Na^{+} channels. Based on the primary structure, it was suspected to be a novel voltage-gated cation channel and was named two pore channel (TPC).[37] Subsequently these channels, with two homologous sequences, TPC1 and TPC2, were identified in human and many other vertebrate species, while TPC3 and other subtypes were found in plants and some lower animal species such as lancelets, sea urchins, and sea squirts but also in some mammals.[38] From the perspective of biological evolution, TPCs might have existed more widely in ancient creatures, and have become extinct during evolution.[31]

The cellular functions of TPCs were not revealed in earlier studies because of technical restrictions in that the electrophysiological techniques failed to detect functional currents in CHO cells and Xenopus oocytes.[37] The functions of TPCs were mysterious until a study revealed that fluorescent probes targeting lysosomes colocalized with HA-tagged human TPC2.[39] Then people realized that these channels are actually on intracellular acidic organelles instead of on the cell membrane. Further studies confirmed that all subtypes of TPCs occur on acidic organelles in human cells, although some differences exist in detailed distribution so that TPC1 is located on late endosomes while TPC2 is located on lysosomes, and it has also been reported that TPC2 transiently overexpresses in the ER.[39,40] After confirming the exact location of TPCs in cells, researchers started to focus on functional studies of TPCs and confirmed that TPCs as cation channels mediate Ca^{2+} release from acidic organelles triggered by NAADP.[41] As reviewed in the previous paragraphs, NAADP was proven to be a potent Ca^{2+} mobilizing molecule which specifically triggers Ca^{2+} release from intracellular Ca^{2+} stores. Although the detailed mechanisms and receptors remain unclear, the involvement of TPCs was demonstrated in different ways, for example inhibition of TPC2 expression by shRNA in HEK293 cells significantly depressed NAADP-triggered Ca^{2+} signals, and overexpression of TPC2 increased the affinity of NAADP for the organelle membranes.[42,43] Further research proved that TPCs play vital roles in NAADP-related physiological functions in various mammalian cells such as pancreatic acinar and β cells, cardiac muscle cells, T lymphocytes, and platelets.[31]

1.2.3 Updates by recent research (structure and pharmacological regulation).

It is well-known that TPC is a homodimer with two homologous 6-TM repeats.[44] The 3D architecture of Arabidopsis thaliana TPC1 (AtTPC1) was first detected by X-ray crystallography.[45] However, the detailed structure of mammalian TPCs was not reported until 2018-2019.[46,47] Researchers employed electron cryo-microscopy to reveal the high-resolution structure of TPCs with details of a phosphatidylinositol 3,5-bisphosphate (IP3)-binding pocket. Unlike other cation channels, the gating role and ion selectivity of mammalian TPCs relies on a steric hydrophobic gate which opens only when ligands bind to specific activators and allows cations of a certain size (Na^+ and Ca^{2+}) to flow out.[48] These studies also revealed a non-negligible result that IP_3 is necessary for the activation of TPCs and acts in an direct way while the studies did not mention NAADP.[46,47] This makes the actual activation mechanisms and molecular functions of TPCs complicated to understand.

It has been known for some time that rapamycin and sphingosine activate TPCs endogenously, by either direct or indirect stimulation of Ca^{2+} from endolysosomes. Recently, some pharmacologic activators were discovered by electrophysiology-based high-throughput screening. Some tricyclic antidepressants (TCAs) are believed to activate a lysosomal Na^+ channel that may be a TPC, by a voltage-dependent mechanism.[49]

Similar methods have been used to search for TPC inhibitors. Naringenin, a natural flavonoid in grapefruit, was shown to be an inhibitor of TRPM3 and TRPP2 channels.[50,51] Recent studies used electrophysiological analysis of naringenin's effects and showed that naringenin can reversibly block the current conduction of TPCs.[52] A further study used molecular docking to predict the selectivity and reveal the binding sites for naringenin in TPC inhibition.[53]

Previously, some pore-blockers such as verapamil and tetrandrine, have been shown to act as inhibitors of TPCs,.[54,55] As the structures of TPCs are increasingly clear, structure-based virtual screening (SBVS) has been used to search for pharmacological modulators of TPCs. Some existing pharmaceutical molecules, including bepridil, clomiphene, fluphenazine, pimozide, raloxifene, and tamoxifen, were confirmed as TPC2 inhibitors; these selectively block NAADP-elicited Ca^{2+} responses and stop TPC2 opening. Ned-19 is an antagonist of NAADP and also an indirect inhibitor of TPCs, which is widely used in the lab. It was first identified by a ligand-based virtual screening (LBVS). Ned-19 was shown to block not only NAADP-mediated Ca^{2+} release but also NAADP binding to its receptors.[56,57] The minimally modified analogue of Ned-19, is also regarded as an NAADP antagonist and is named Ned-K.[58]

1.2.4 The roles of TPCs in various pathological processes.

The main physiological role of TPCs is ion trafficking in the endolysosome system,

which is related to various pathological processes.

Viral and bacterial infections often make use of the endolysosome systems of host cells. Since TPCs are regulators of endocytosis, micropinocytosis, and phagocytosis, they are likely to play key roles in the process of infection. Indeed, some studies have shown that inhibition of TPCs reduced infectivity of Ebola virus, MERS, and Covid-19. Recently, researchers have become very interested in the possibility of TPCs as drug targets for Covid-19 treatment, since naringenin, a reversible inhibitor of TPC, was proven to be a powerful inhibitor of SARS-CoV-2 infection *in vitro*.[59] However, the first study revealing a role of TPC in infection was in 2014, which showed that TPC1 knockout impaired the trafficking of cholera toxin to the Golgi apparatus.[60] Similar toxin trafficking through the endolysosomal system associated with TPCs was shown to play a role in diphtheria and anthrax.[61]

The impairment of the endolysosomal pathways has been associated with common neurodegenerative diseases, such as Alzheimer's, Parkinson's, and Huntington's.[62] A recent study revealed that exaggerated TPC2-mediated Ca^{2+} outflow caused an enhanced pH in lysosomes and compromised the autophagy-lysosomal pathway (ALP) degradation, which is a main cause of the amyloid plaque accumulation in Alzheimer’s disease.[63] Exaggerated lysosomal Ca^{2+} outflow also plays a vital role in Parkinson’s disease (PD); thus studies have shown that the Ca^{2+} store content in both ER and lysosomes was reduced in fibroblasts from PD patients but not in cells from healthy

people.[64] A further study proved that this is related to a pathogenic LRRK2 cascade which disrupts normal Ca^{2+} flow from TPC2.[65]

As well as the explicit roles of TPCs in infection and neurodegenerative diseases, TPCs have been shown to play a role in cancer. The roles of TPCs in cancer are in three main areas. Firstly, TPC-mediated NAADP-triggered Ca^{2+} signalling can help tumour growth and vascularization in B16 melanoma cells through driving angiogenesis by promoting VEGF secretion.[66] Secondly, migration and metastatic invasion of cancer cells is also dependent on TPCs, which was shown in a study of the lung metastasis of mammary mouse cancer cells. This showed that inhibition of TPCs disrupted trafficking of β1-integrin which led to β1-integrin accumulation in EEA1-positive early endosomes. The accumulation of β1-integrin resulted in the inability of invasive cancer cells to form leading edges required for migration.[67] Finally, TPC2 controls tumour proliferation in melanoma. Reduced TPC levels resulted in reduced protein levels of microphthalmia-associated transcription factor (MITF), which is a major regulator of melanoma progression by promoting tyrosinase activity. This suggests that TPCs in melanosomes and endolysosomes are important regulators of melanoma tumourigenesis.[68]

1.2.5 Cognitive updates on TPCs and possible impact on the observations in this thesis.

TPCs were regarded as NAADP-triggered Ca^{2+} ion channels located on endo-

lysosomes since they were discovered. However, ten years ago, a research team published a completely new perspective that TPCs are sodium-selective channels activated by phosphatidylinositol-3,5-bisphosphate $PI(3,5)P_2$, and are not activated by NAADP; thus they provided evidence that $PI(3,5)P_2$-activated currents through TPCs are Na^+-selective, and also, in TPC-double-knockout mice pancreatic β-cells, NAADP-induced lysosomal Ca^{2+} release does not disappear.[69]

Also, TPCs were reported to be related to ATP-mediated inhibition of Na^+ through forming a mTOR-TPC complex.[70]

Therefore, later researchers concluded that TPCs are activated via a complicated mechanism. NAADP triggers Ca^{2+} release from the endolysosomal lumen through TPCs, $PI(3,5)P_2$ triggers Na^+ release from endolysosomes through TPCs, and voltage variation triggers Ca^{2+}, Na^+ and H^+ outflux from endolysosomes through TPC1 and is regulated by Ca_v/Na_v modifiers.[71]

In general, it has been widely accepted that TPCs are multifunctional cation channels regulated by complicated mechanisms. However, there is still a theory that TPC is merely a channel that induces Na^+ outflow and has nothing to do with NAADP triggered Ca^{2+} signalling. In contrast to the function of Ca^{2+} as second messengers, changes in the concentration of Na^+ in cytosol lead to completely different physiological effects. The main result of Na^+ overload is cell swelling, Na^+ outflow from endolysosome may

also suppress Ca^{2+} outflow. Based on these understandings, many existing conclusions will be overturned.

Regarding the conclusions in my study, TPC2 was suspected to have reciprocal interactions with cAMP-response element binding protein (CREB) through PKA/PKC, but the detailed mechanism remains unclear. If TPC2 not only mediates Ca^{2+} but also mediates Na^{+}, the interactions between CREB and TPC2 transcription may be through different mechanisms (Figure 2).

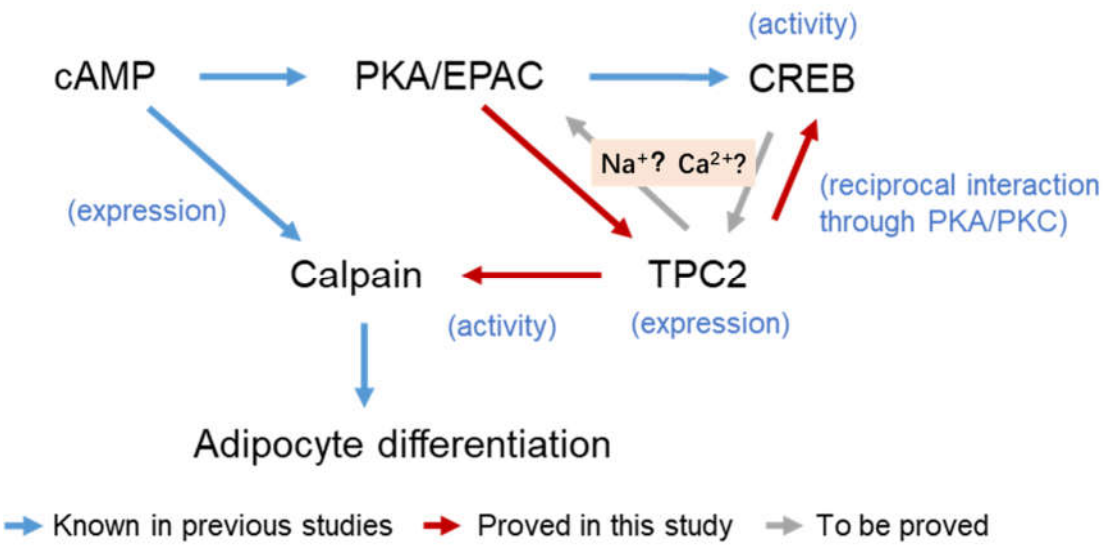


Figure 2. The mechanism by which TPC2 is involved in cAMP induced adipocyte differentiation. NAADP triggered Ca^{2+} and $PI(3,5)P_2$ triggered Na^{+} are both likely to play a role in the interaction between CREB and TPC2.

In terms of TPC1, the research in this thesis aims to study TPC1 as a possible drug target, therefore, emphasis was put on how the existence of TPC1 would alter cellular

functions. This thesis raises the following conclusions about the cellular function of TPC1. First, TPC1 plays a vital role in the production and activation of digestive enzymes in pancreatic acinar cells. Second, in terms of cellular biological processes, TPC1 participates in fatty acid β-oxidation, probably by regulating the activity of acyl-CoA dehydrogenase. Besides, analysis of cellular components indicates that TPC1 regulates cytochrome C expression. Last but not the least, in the chapter about TPC functions in infectious disease, TPC1 is shown to have an inhibiting effect on TIMP-1 over-expression caused by SARS-CoV-2 pseudo virus infection. In my study of TPC1, the hypothesis and conclusions have no correlation with Ca^{2+} signalling, and therefore will not be overturned if TPCs are proved to be Na^{+} selective channels and have no relationship with Ca^{2+}.

1.2.6 The unsolved problems and possible future research directions.

Until recently, apart from mediating NAADP-triggered Ca^{2+} release, little has been known about the NAADP-independent physiological functions of TPCs. The exact functions of TPCs without inevitable involvement of NAADP would be a promising research direction in future. In recent years, the discovery of TPC1 and TPC2 probes has made it possible to study the independent functions of TPCs in various cell types.

One possible future direction for research is the function of TPC2 in melanosomes,

which are lysosome related organelles in melanocytes responsible for melanin production. A study has shown that the polymorphic variants of Tpcn2 gene are related to hair colour of Northern Europeans, indicating that TPC2 may regulate melanin production in melanocytes and melanin release to keratinocytes where pigmentation occurs.[72]

Cancer, with a particular emphasis on metastasis and autophagy, is another promising direction to continue exploring. It was revealed that the TPCN2 gene is markedly overexpressed in primary tumours of human oral cancer, and researchers attributed this phenomenon to the intraluminal alkalinization caused by Ca^{2+} outflow from TPC2 which led to the inhibition of fusion among endosomes, autophagosomes, and lysosomes.[73]

Intracellular pH is crucial in almost all cellular activities. Lysosomes are acidic organelles with a pH range of 4.0-5.5, which is necessary to maintain the activity of hydrolytic enzymes in lysosomes. Under normal pH conditions, lysozyme can effectively degrade and digest exogenous biomolecules. Abnormal pH can lead to cell dysfunction and lysosome storage disorders. TPC-dependent intraluminal alkalinization is a mechanism to regulate pH in lysosomes. Down to the inner mechanism, the pH value represents the concentration of active H^+. The import and export of ions in lysosomes are controlled by H^+ pumps such as V-ATPase and cation channels such as TPCs. When the pH value is higher than the range of 4.0-5.5,

indicating that the lysosome is too alkaline, the V-ATPase gains more activity through hydrolyzing ATP and pumping in more H^+, and meanwhile, TPCs are activated and trigger Ca^{2+} and Na^+ outflux, which enhances acidity in lysosomes. In contrast, when the pH value is too low, indicating the lysosomes are too acidic, TPCs close to contain Ca^{2+} and Na^+ to cause intraluminal alkalinization (Figure 3).[74]

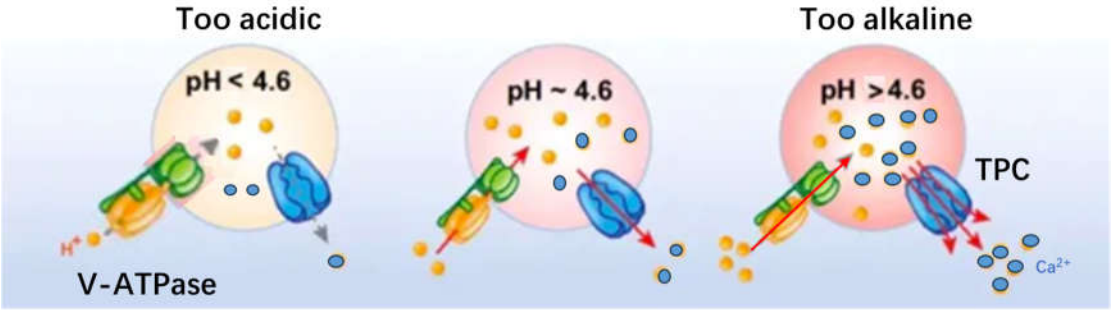


Figure 3. [74] A schematic diagram of the mechanism of lysosomal pH regulation. (V-ATPase: Vacuolar ATPase.)

However, in a pathological state, TPC dysfunction leads to pathological intraluminal alkalinization in lysosomes which is related to the activation of pH-sensitive hydrolytic enzymes including glucocerebrosidase and acid sphingomyelinase. These enzymes regulate the levels of glucocerebroside and sphingomyelin. The deactivation of these hydrolytic enzymes may lead to the accumulation of glucocerebroside and sphingomyelin which results in Gaucher's disease and Niemann-Pick disease.[75,76]

1.3 Ca^{2+} signalling in metabolism.

1.3.1 Pancreatic digestive enzyme secretion.

1.3.1.1 The exocrine function of the pancreas.

The pancreas is the second largest exocrine organ in the human body after the liver. The pancreas is divided into exocrine and endocrine parts. The exocrine part of the pancreas is composed of the acinar duct and interstitium. The acinus is involved in synthesis, storage and secretion of digestive enzymes, while the main function of the catheter is to secrete water and electrolytes, and it is also a conduit for transporting pancreatic fluid. The endocrine part of the pancreas is the islet; the islet cells produce insulin, glucagon and other hormones, which are released into the blood circulation to act on a number of target organs.[77]

The pancreas is covered by a thin connective tissue capsule, which extends into the gland and divides the parenchyma into lobules, but the boundary between the lobules of the human pancreas is not obvious. The glandular parenchyma consists of an exocrine part and an endocrine part. The exocrine part is the serous complex tubular vesicular gland. The interlobular connective tissue contains ducts, blood vessels, lymphatic vessels, and nerves (Figure 4).[78] Nerve endings are distributed in blood vessels, acinus, pancreatic duct cells, and islet cells. Cholinergic nerves regulate the exocrine pancreas, and sympathetic nerves reduce pancreatic fluid secretion mainly by

reducing pancreatic blood vessel flow (Figure 4).[77]

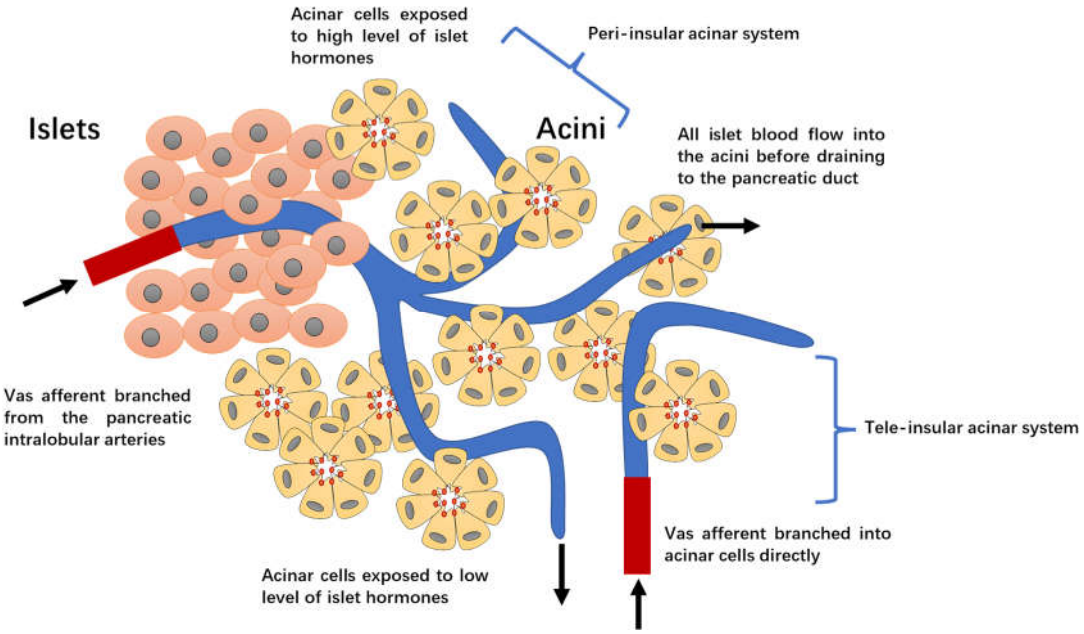


Figure 4. A schematic representation of the pancreatic insulo-acinar portal system. The islets and acini make functional contact via islet peptide hormones which facilitate exocrine and endocrine interaction and jointly impact on the secretion function of pancreatic acinar cells.[79]

The pancreatic duct runs in the parenchyma of the pancreas from the tail of the pancreas to the back of the pancreatic body passing from left to right, and its mean length is 13.8 cm. The duct diameter gradually increases from left to right, with an average tail diameter of 0.2 cm, and an average head diameter of 0.4 cm.[80] There are two narrow zones in the pancreatic duct, one at the junction of the head and body, and one along the pancreatic body. The main pancreatic duct is composed of 15-30 small branches (rami) of similar diameter throughout, which branch outward from the main pancreatic

duct.[81] These primary pancreatic duct branches (rami), according to their positions, are respectively referred to as cephalic rami, inferior cephalic rami (i.e., rami uncinatus), rami corporis superior, rami subsomalis, rami caudalis superior and rami caudalis inferior.[82]

From the neck of the pancreas, the main pancreatic duct goes downward, backward, and to the right, reaching the posterior medial wall of the descending part of the duodenum and running parallel to the common bile duct, which is located at the left, inside, and below the common bile duct. Then the pancreatic duct and common bile duct pass obliquely through the duodenal wall together, and the end duct shrinks in diameter, and finally meets the common bile duct.

The acinus secretes pancreatic fluid, and the glandular ducts are the channels through which pancreatic fluid is discharged. The pH of pancreatic fluid is between 7.8 and 8.4. and the osmotic pressure of pancreatic fluid is similar to that of blood. The pancreatic fluid drains into the duodenum through the pancreatic ducts, where it digests proteins, fats, and sugars. Pancreatic fluid contains inorganic substance such as sodium bicarbonate, and organic substances including trypsinogen, enterokinase, ribonuclease, deoxyribonuclease, hydroxy lipase, and amylase. Bicarbonates are mainly used to neutralize the gastric acid entering the duodenum, so that the intestinal mucosa is protected from the erosion of strong acids, and they also provide the most comfortable pH environment for various enzymes in the small intestine. Proteins, carbohydrates,

and fats in food need to be processed by these pancreatic enzymes before they can be absorbed by the body. It can be seen that pancreatic fluid is a very important digestive fluid.[80,83]

Pancreatic enzymes are first synthesized on ribosomes in the cytoplasm and transferred to the rough endoplasmic reticulum, and then transferred into vesicles through membranes. The synthesized enzymes are transferred from vesicles to the Golgi complex, where they are further processed and concentrated to form enzymatic proteins and stored in the proenzyme granules.[77,78,81,83]

1.3.1.2 The physiological process and regulatory factors of digestive enzyme secretion from pancreatic acinar cells.

Acinar cells are stimulated by secretory activators such as secretin, CCK, or acetylcholine, which mainly act on cell membrane receptors and then trigger intracellular cAMP or Ca^{2+} elevation, respectively, resulting in exocytosis. The mechanism of fusion may be the change of lipid or protein composition in the membrane, and then fission occurs, and the enzymes are discharged into the acinar cavity (Figure 5). During the fasting period, the enzyme secretion is less, and the enzyme particles in the acinar cells become larger and greater in numbers. During digestion after satiation, due to the presence of factors that strongly and continuously stimulate pancreatic enzyme secretion, the enzyme granules in the pancreatic acinus

can be depleted (Figure 5).

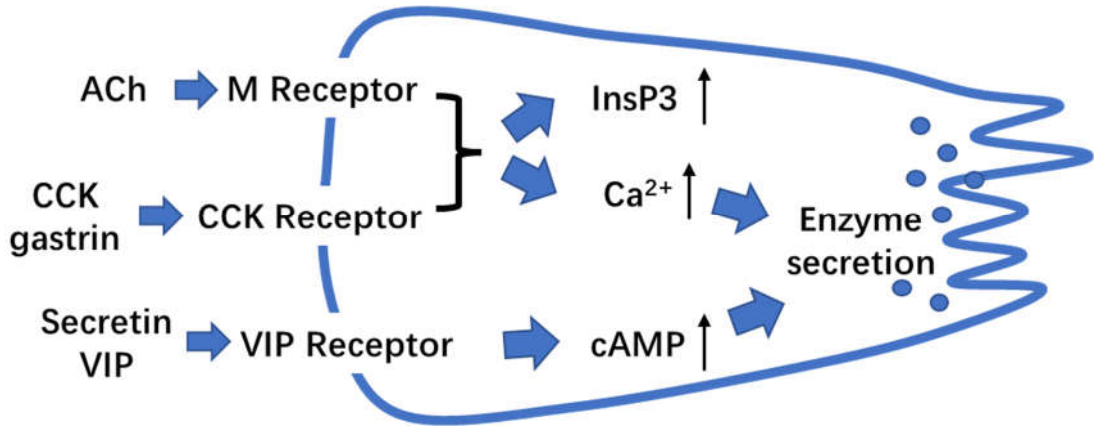


Figure 5. Schematic diagram of the membrane receptor and post-receptor pathways that stimulate pancreatic enzyme secretion. ACh, CCK, secretin, and VIP from gastrin bind to their receptors on the surface of pancreatic acinar cells and initiate phosphatidylinositol turnover, Ca^{2+} signalling, and cAMP signalling in cells which synergistically stimulates enzyme secretion. (ACh – acetylcholine, CCK – cholecystokinin, VIP - vasoactive intestinal polypeptide, cAMP - cyclic adenosine monophosphate, M receptor - muscarinic receptors, $InsP_3$ - inositol 1,4,5 trisphosphate.)

Food, and neural and hormonal systems, are major regulators of enzyme secretion by acinar cells. As shown in Figure 5, the secretory function of acinar cells is modulated via intracellular signalling pathways. The major modulators are the excitatory neurocranial molecule acetylcholine (ACh), endocranial molecule cholecystokinin (CCK), and other paracrine/endocrine molecules such as secretin and vasoactive intestinal polypeptide (VIP).[84] To stimulate the secretory function of acinar cells, ACh

binds to muscarinic receptors while CCK binds to CCK receptors, and these receptors are linked to a type of G-protein, Gαq, which results in second messenger inositol 1,4,5 trisphosphate ($InsP_3$) generation and transduction of signals via the phospholipase C (PLC)/Ca^{2+} signalling pathway. The enhanced cytosolic Ca^{2+} concentration activates pancreatic enzyme exocytosis from acinar cells. However, the pancreatic acinar cells are not electrically excitable, which indicates that the Ca^{2+} in the cytosol is not from the extracellular matrix but from intracellular Ca^{2+} stores. This was proven by experiments in 1976 when Peterson and colleagues found that the initial ACh and CCK secretion in pancreatic acinar cells did not trigger extracellular Ca^{2+} influx, and only when intracellular Ca^{2+} stores were depleted, did extracellular Ca^{2+} start to flow in.[85] It was also proven that the intracellular Ca^{2+} level was determined by the concentration of ACh or CCK.[86]

Gastrin is an important gastrointestinal hormone secreted mainly by G cells which are typical open type endocrine cells, located in the antrum, fundus, duodenum, and jejunum. The cellular function of gastrin is similar to cholecystokinin (CCK). Gastrin and CCK activate cholecystokinin type 2 receptor (CCK2R) synergistically, while Gastrin does not activate cholecystokinin type 1 receptor (CCK1R). The two types of CCK receptors mediate cellular effects through different down-stream pathways. CCK1R activates adenylyl cyclase (AC) which catalyzes ATP into cAMP and thus activates the PKA pathway while CCK2R doesn’t. Both CCK receptors stimulate

intracellular Ca^{2+} signalling through $InsP_3$, which indicates that gastrin triggers enzyme secretion in pancreatic acinar cells through the $InsP_3$-Ca^{2+} pathway, while CCK triggers enzyme secretion through both the cAMP-PKA and $InsP_3$-Ca^{2+} pathways.[87]

Secondary messengers other than Ca^{2+}, for example, cAMP, also play a role in regulating exocrine secretion in pancreatic acinar cells. VIP and secretin bind to their respective receptors which activate Gαs G-proteins and stimulate AC and thus result in cAMP generation from ATP.[88] VIP also up-regulates PKA activation. PKA induces the fusion of zymogen granules (ZG) with the apical plasma membrane which leads to the exocytosis of enzymes into the acini lumens.[89]

VIP is a type of neurotransmitter that is present in the central nervous system and enteric nervous system and is mainly released by neurons in the gut. VIP has a dual role of being both a gastrointestinal hormone and neuropeptide. The main functions of VIP are dilating blood vessels and lowering blood pressure. Regarding the digestive system, VIP helps to relax the intestinal smooth muscle and the lower esophageal sphincter. In pancreas, VIP not only maintains normal exocytosis by stimulating PKA activation which induces the fusion of zymogen granules with the apical plasma membrane, but also maintains normal pancreatic functions by its vasodilation function. As far as I can guess, since high blood pressure may lead to the dysfunction of the pancreas by preventing the secretions of β-cells from entering the circulation, the vasodilation function of VIP helps relieve this process and maintains normal endocrine functions in

pancreas and eventually results in the normal blood glucose level maintained by sufficient glucagon and insulin. [87]

The renin-angiotensin system (RAS) has also been shown to play vital roles in the enzyme secretion function of pancreatic acinar as well as islet cells. In certain tissues such as the pancreas there exists a local RAS which acts as a paracrine or autocrine factor, and its function is totally independent from the circulating RAS. The detailed mechanism underlying the regulation by local RAS signalling of enzyme secretion remains unclear. Some researchers believe that tissue RAS regulates acinar cell digestive enzyme secretion and some other physiological process through vasoconstrictive effects,[90] while others think that angiotensin II stimulates exocytosis of pancreatic acinar cells through triggering intracellular Ca^{2+} signals.[91] However, the most notable function of the local RAS in pancreas is regulation of anion secretion in duct cells and hormonal secretion in islet cells, which indicates that the local RAS is a potential drug target in diabetes and acute pancreatitis.[90,92]

1.3.1.3 The complexity of the origin and molecular basis of Ca^{2+} signals in pancreatic acinar cells.

In the previous section I reviewed the regulatory mechanisms of enzyme secretion and exocytosis in acinar cells. In the whole process, Ca^{2+} signals are fundamentally important but complex.

The complexity of the Ca^{2+} signalling activation includes its spatial and temporal characteristics. In terms of spatial characteristics, Ca^{2+} release is from the apical pole of the acinus while contradictorily, $InsP_3$, the factor which triggers Ca^{2+} signalling when activated by ACh and CCK, is produced at the lateral and basal membranes. What interested researchers was that $InsP_3Rs$, which are the $InsP_3$ regulated calcium permeable channels in the endoplasmic reticulum (ER), are located in the lateral and basal membranes where they generate Ca^{2+} signals.[93,94] At the same, there exists a delay before the Ca^{2+} wave proceeds across the cell, which contributes to the spatial dynamics of secretagogue stimulation of $InsP_3$, and this indicates that the molecular basis of Ca^{2+} release is complex and still to some extent unclear.

Unlike other type of cells like those in nerves and muscles, voltage-gated Ca^{2+} channels do not exist in exocrine cells including pancreatic acinar cells, while instead, $InsP_3$-mediated store-operated Ca^{2+} channels (SOCs) mediate Ca^{2+} influx. Only when the Ca^{2+} is depleted in intracellular Ca^{2+} stores, does the secretagogue stimulated Ca^{2+} influx from the extracellular matrix become crucial. The SOCs are very important and sensitive since excessive Ca^{2+} influx leads to Ca^{2+} overload and is toxic to cells and it is also responsible for the molecular pathogenesis of almost all forms of pancreatitis.[95] In pancreatic acinar cells, proper amounts of Ca^{2+} help maintain normal exocytosis of zymogen granules. However, lifestyle linked cytosolic Ca^{2+} overload tends to result in the untimely activation of trypsinogen in the apical pole of acinar cells, which further

causes autodigestion and is regarded as one of the main forms of pathogenesis in pancreatitis.

Until recently, the upstream mechanism of SOC activation in pancreatic acinar cells remained unclear since the identity and function of SOCs were unclear. However, research has shown that TRPC3 of the transient receptor potential canonical family partly modulates the SOC and thus influences physiological processes such as exocytosis, actin depolymerization, and intracellular trypsin activation in pancreatic acinar cells.[96]

Studies of Ca^{2+} signalling in pancreatic acinar cells are mainly focused on $InsP_3$-triggered Ca^{2+} release from ER. However, since pancreatic acinar cells also possess extensive acidic Ca^{2+} stores, researchers suspected that there may also be a special role for NAADP-triggered Ca^{2+} signalling. In contrast to the ER, acidic stores such as endolysosomal systems maintain high Ca^{2+} levels via functional vacuolar H^+ pumps. A study has shown that $InsP_3$ can release Ca^{2+} from the ER as well as from acidic stores containing vacuolar H^+ pumps.[97] A few years later, another two studies showed that $InsP_3$ and cyclic ADP-ribose (cADPR) can liberate Ca^{2+} from pancreatic secretory granules.[98] However, the amount of Ca^{2+} released from the endolysosomal system is very small and thus difficult to detect. The mechanism of Ca^{2+} release trigged by NAADP was revealed in 2008 when Murphy and colleagues proved that CCK acts on pancreatic acinar cells partly via NAADP-initiated Ca^{2+} release to evoke pancreatic

enzyme secretion.[99] A later study further revealed that endogenous NAADP generation requires a synthase differing from the ADP-ribosyl cyclase family, and ectoenzyme CD38 was proven to be necessary for the NAADP-mediated Ca^{2+} release triggered by CCK in pancreatic acinar cells.[100]

As early as 1999, Cancela and colleagues revealed that NAADP can trigger Ca^{2+} signalling in pancreatic acinar cells at a low concentration (50nM) but not at higher concentrations (1-100 uM) since high concentrations of NAADP would cause self-desensitization which led to inactivation of CCK-evoked Ca^{2+} signals.[101] This suggests that NAADP functions as an intracellular messenger in pancreatic acinar cells either via the CCK pathway or via an independent mechanism. Many researchers believe that NAADP initiates CCK signalling and that the signalling is subsequently amplified by the cADPR and IP_3.[102] However, the role of TPCs in pancreatic acinar cells was not reported until 2015, when Gerasimenko and colleagues related NAADP-triggered Ca^{2+} signalling to RyRs and TPCs in pancreatic acinar cells. In the same piece of research, they also showed that TPC2, which was responsible for mediating 64% of the NAADP-triggered Ca^{2+}, was more important than TPC1 in mediating NAADP-triggered Ca^{2+} releases from acidic stores in pancreatic acinar cells.[103]

1.3.2 Ca^{2+} signalling in adipocyte differentiation.

1.3.2.1 How does adipogenesis occur and how do stem cells differentiate into adipocytes *in vitro*?

Adipose tissue is an important energy storage organ in human body. When energy intake exceeds energy consumption, the body will store the excess energy in the form of triglyceride in adipose cells. When energy consumption in the body exceeds energy intake, triglycerides stored in fat cells will be broken down into free fatty acids and released to supplement the physiological needs of other cells or tissues. In addition, recent studies have shown that adipose tissue is an important endocrine tissue that secretes a variety of cytokines (adipokines), such as leptin, interleukin, tumor necrosis factor α (TNFα) and adiponectin.[104] On the one hand, these cytokines are involved in the regulation of normal energy metabolism. On the other hand, the cytokines such as adenosine deaminase (ADA) can also be the criteria to diagnose metabolic syndromes. Previous studies have shown that too much or too little adipose tissue can both cause metabolic syndromes.

Adipocytes originate from pluripotent stem cells (PSC) in the vascular matrix, which have the potential of self-renewal and multi-differentiation. Under appropriate conditions, PSCs can differentiate not only into adipocytes, but also into mesodermal derived cells such as muscle cells, chondrocytes, and osteoblasts.[105] The developmental

process from pluripotent stem cells to adipocytes can be divided into three stages, pluripotent stem cells, preadipocytes, and then fat cells (adipocytes). Current research in this field is mainly focused on the mechanism by which stem cells give rise to preadipocytes, as well as on the source of these pluripotent stem cells.[105]

The increase of adipose tissue volume is not only due to the increase of adipose cell size, but also due to an increase in the number of fat cells. The increase in the number of fat cells is due, on the one hand, to the development of stem cells into preadipocytes, which are then induced to differentiate into adipocytes under an appropriate hormonal environment. On the other hand, mitotic cloning amplification occurs during the differentiation of preadipocytes into adipocytes. 3T3-L1 is a preadipocyte cell line which has been widely used in the past 30 years to study the mechanism of adipocyte terminal differentiation.[104] During the culture of 3T3-L1 preadipocytes, contact inhibition occurs after cell growth and fusion, so that cells will stay in the G0/G1 phase of the cell cycle. This process was named as growth inhibition which is essential for preadipocyte differentiation.[106] Upon receiving appropriate mitosis and lipogenesis signals, growth-inhibited preadipocytes synchronously re-start the cell cycle and undergo several rounds of cell division in a process known as mitotic cloning amplification.[106] Although there are still debates about whether mitotic cloning amplification is crucial for adipocyte differentiation, a growing number of pieces of experimental evidence suggest that mitotic cloning amplification is a prerequisite for

adipocyte terminal differentiation.[107]

It was generally thought that mitosis loosened the structure of the DNA, thus allowing transcription factors to enter the transcriptional regulatory binding regions of specific genes to initiate the subsequent adipocyte differentiation process.[108,109] Numerous studies have shown that inhibiting the amplification of mitotic clones also inhibits adipocyte differentiation.[109] For example, when rapamycin, aphidicolin or roscovitine were used to block the process of the cell cycle, adipocyte differentiation was also blocked.[109] Blocking the C/EBPβ signal which promotes the amplification of mitotic clones, also inhibits adipocyte differentiation.[110,111] Along with mitotic cloning amplification, cells enter a unique cell cycle phase known as the GD phase, which is a second and permanent phase of growth inhibition. In 3T3-L1 cells, the GD phase is characterized by changes in the expression of cyclin-dependent kinase inhibitors p18, p21, and p27.[112] Even after initiation of differentiation, preadipocytes still retain the ability to dedifferentiate and re-start mitosis, but once the they exit the GD phase, they will proceed to terminal differentiation.[107]

1.3.2.2 Critical adipocyte specific genes and the functions of transcription factors.

In the process of terminal differentiation, programmed expression of a series of important transcription factors leads to the expression of adipocyte specific genes,

which then result in the generation of adipocyte phenotypes. So far, most studies about the role of transcription factors in this process have focused on the C/EBP family and the PPAR family.[113] The C/EBP family are transcription factors with the function of activating CCAAT repeats of DNA enhancers of specific genes. To date, six members have been discovered, namely C/EBPα, C/EBPβ, C/EBPγ, C/EBPδ, C/EBPe, and C/EBPx (also known as CHOP-10).[113] These proteins regulate cell growth, differentiation, and the immune response in a variety of tissues. Among them, C/EBPα, C/EBPβ, C/EBPδ, and CHOP-10 are involved in fat formation. C/EBP family members have three essential functional domains: the transcriptional activation domain, the DNA binding domain, and the dimerization domain.[111]

The C/EBP dimerization domain is rich in leucine, and these leucine residues all appear in the same direction in a helix to form a leucine zipper structure, through which C/EBP can be bonded to itself or other C/EBP members in hydrophobic bonds to form homologous- or hetero-dimers.[114] The affinity of C/EBP to DNA is affected by the formation of such homologous- or hetero-dimers and is significantly reduced by the non-dimer C/EBP.[114] The DNA binding domain and dimerization functional domain are both located in the C-terminal of proteins, therefore, they are collectively referred to as the bZIP domain, which is highly conserved in the C/EBP family.[114] The C/EBP family is the first family of transcription factors that have been shown to play an important role in adipocyte differentiation and are expressed in a certain sequence during

adipogenesis.[114] Early in the differentiation process, the expression of transcription factors C/EBPβ and C/EBPδ is rapidly increased, and subsequently, activated C/EBPβ and C/EBPδ then activate C/EBPα. The C/EBPα gene promoter has a C/EBP regulatory element, which binds to C/EBPα to activate its self-expression and maintain the process of differentiation.[115] C/EBPβ and C/EBPδ can be induced by cAMP and glucocorticoid, respectively; their roles in adipogenesis were discovered by transgenic methods.[115] Exogenous expression of C/EBPβ in hormone deficiency was shown to be sufficient to promote the differentiation of 3T3-L1 preadipocytes into adipocytes, while exogenous expression of C/EBPδ accelerated fat accumulation. Embryonic fibroblasts lacking either C/EBPβ or C/EBPδ had significantly reduced adipogenesis, but when both were deficient, adipocyte differentiation was severely blocked.[115] Similar results have been obtained *in vivo*; thus mice with either C/EBPβ or C/EBPδ knocked out had normal white adipose tissue but showed delayed adipose accumulation in brown adipose tissue.[116] In mice with C/EBPβ and C/EBPδ knocked out at the same time, 85% of individuals died of unknown causes in the perinatal period, and the survivors had significantly reduced brown adipose tissue and slightly reduced white adipose tissue.[116] C/EBPβ is also regulated by programmed phosphorylation and glycosylation prior to transcriptional activity.[115,117,118]

C/EBPα is considered to be an essential factor in adipocyte differentiation. C/EBPα is expressed at a relatively late stage of differentiation and can activate a large number of

specific genes required for adipocyte differentiation, such as the 422/aP2, SCD1, GLUT4, and Ob genes.[112] Antisense C/EBPα mRNA fragments inhibit hormone-induced cell differentiation in 3T3-L1 preadipocytes. Ectopic expression of C/EBPα initiates differentiation in the absence of hormone induction. CHOP-10 does not have a DNA-binding domain, but via heterodimerization with other C/EBP members it can inhibit the transcriptional activity of other members.[119] CHOP-10 is expressed in growth-inhibited preadipocytes. After hormone induction, the expression of CHOP-10 is down-regulated and C/EBPβ is released in the preadipocytes after they enter the S phase, thus causing the preadipocytes to differentiate into adipocytes.[119] Overexpression of CHOP-10 or increased expression of CHOP-10 with proteasome inhibitors inhibited adipocyte differentiation.[119]

The peroxidase proliferator-activated receptor (PPAR) family is a class of nuclear hormone receptors. It is composed of three different genes encoding nuclear receptors PPARα, PPARβ (δ), and PPARγ. The structure of PPAR consists of four functional regions. The first is the N-terminal ligand-independent active region, the structure of which differs greatly for each isotype. The serine residues of PPAR can inhibit the activity of the receptor after phosphorylation by mitogen activated protein kinase (MAPK). The second is a highly conserved DNA binding region (DBD) that binds to the target PPAR reaction element (PPRE). The third is the hinge region, connecting the DBD to the ligand binding region. The last is the ligand-binding region (LBD), in which

different amino acid sequences allow each subtype of PPAR to have affinity for different ligands. The activated PPAR protein binds to another nuclear receptor, resin-like X receptor (RXR), to form a heterodimer, which then acts on specific peroxide-proliferative response elements to alter gene regulation in target cells.[120] PPARγ is a key regulator of fat formation. The expression of PPARγ transcription factor increases during the induction of differentiation, and then activates the expression of a large number of downstream genes related to fatty acid binding, uptake, and storage, such as 422/aP2, lipoprotein enzyme, acetyl-CoA synthase and phosphoenolpyruvate carboxykinase (PEPCK).[120–123] There are three subtypes of PPARγ, which are PPARγ1, PPARγ2, and PPARγ3. PPARγ1 is expressed at a low level in diverse tissues, while PPARγ2 is only expressed in adipocytes, and PPARγ3 is only found in macrophages and large intestinal cells. The importance of PPARγ in fat formation has been demonstrated in many ways. PPARγ-deficient mice tend to die during the embryo stage due to placental defects, and embryonic stem cells with PPARγ heterozygote (pparγ^{+}/-) can neither differentiate into adipocytes nor participate in adipose tissue formation.[124] Heterotopic expression or activation of PPARγ with exogenous ligand can induce adipocyte differentiation. The combined expression of PPARγ and C/EBPα can transform myoblasts into adipocytes.

C3H10T1/2 is the most commonly used pluripotent stem cell line. It was isolated from 2-3 week old C3H mouse embryos and has fibroblast morphology and multi-

differentiated potential to differentiate into muscle cells, adipocytes, chondrocytes, and osteoblasts under the action of the DNA methylase inhibitor 5-azacytidine.[125–128] This cell type switch is heritable because isolated clones retain these specific phenotypes even if they are no longer treated with 5-azacytidine. The DNA methylase inhibitor 5-azacytidine has been shown to induce the stable expression of one or more genes, and the expression of these genes leads to the development of multipotent stem cells.[114] Myo D was thus discovered as a transcription factor capable of transforming multipotent stem cells into myoblasts.[129] The discovery of Myo D in turn led to the discovery of other transcription factors Myf5 and myogenin in myoblast orientation.[130]

Previous studies have proved that Sox9 is involved in chondrogenic development, while Runx2/Cbfa1 and Osterix are involved in osteogenic development. However, the genes involved in the development of multipotent stem cells into adipocytes remain unclear. Bone morphogenetic protein (BMP), a member of the transforming growth factor beta (TGF-β) superfamily, was first found to induce ectopic osteogenesis.[131] However, it has been found that BMP has various other biological functions and is involved in embryogenesis, organogenesis, and morphogenesis by regulating the development and differentiation of cells.[132] For example, BMPs promote the differentiation of multipotent stem cells into adipocytes, osteoblasts, chondrocytes, and muscle cells.[133–135] Researchers found that BMP-4 could induce multi-potential C3H10T1/2 cells to be fully developed into preadipocytes since when C3H10T1/2 cells were exposed to

exogenous BMP-4, they were automatically directed to develop into preadipocytes, and can further differentiate into mature adipocytes under the action of hormones (3-isobutyl-1-methylxanthine, dexamethasone, and insulin).[136] The same function of BMP-4 was shown *in vivo*; thus the multi-potential C3H10T1/2 cells pretreated with BMP-4 can differentiate into adipose tissue indistinguishable from normal fat after subcutaneous injection into nude mice.[137] Researchers also found that C3H10T1/2 cells treated with the DNA methylase inhibitor 5-azacytidine developed into a preadipocyte cell line A33, which highly expressed BMP-4 endogenously, and the endogenous BMP-4 was required for multipotent stem cells to acquire preadipocyte properties.[137] This phenomenon is very valuable for deciphering the process of orientation of pluripotent stem cells to adipocytes.

Cell density and cell morphology also play important roles in stem cell development. Researchers have found that human pluripotent mesenchymal stem cells are easy to differentiate into osteoblasts at low density and adipocytes at high density.[138] Using a micropatterned matrix to control cell elongation, the researchers found that human stem cells growing on small islands of fibrin contracted and could only differentiate into fat cells (adipocytes). On the other hand, the human mesenchymal stem cells that grow on the larger fibrin islands were flat and stretched out and could only differentiate into osteoblasts. Lysine oxidase (LOX) was shown to play an important role in the formation of the cell matrix. Researchers found that this protein is a target gene of BMP signalling

pathway and plays an important role in the development of stem cells into preadipocytes.[139]

1.3.2.3 The genesis of brown and beige adipocytes.

What we commonly call ‘fat’ is white adipose tissue (WAT), whose main function is to store excess calories in the form of triglycerides. In contrast, the main function of brown adipose tissue (BAT) is to burn excess calories. In terms of cellular structural composition, white adipocytes have a large oil drop (cellulite) and few mitochondria (to power less cellular activity), while brown adipocytes have smaller and more dispersed oil droplets, and they have lots of mitochondria to take in large amounts of glucose and fatty acids. In terms of physiological function, brown adipose tissue can help lower blood glucose, increase leptin sensitivity, insulin sensitivity, and reduce the level of inflammation. It also dramatically increases basal metabolic rate, and even improves bone density. Generally, brown adipocytes consume energy in the form of heat, which is why they are regarded as thermogenic adipocytes (Figure 6).[140]

Human embryos and infants have similar amount of brown adipose tissue to other mammals, but the amount decreases with age. Light and a warm environment can inhibit the activity of brown fat cells and promote their apoptosis. In the modern adult body, due to the optimization of the living environment, the amount of brown adipose tissue is very small, therefore, beige adipocytes are the main form of thermogenic fat.

Beige adipocytes are usually surrounded by white adipocytes and possess similar structural feature to brown adipocytes (Figure 6).

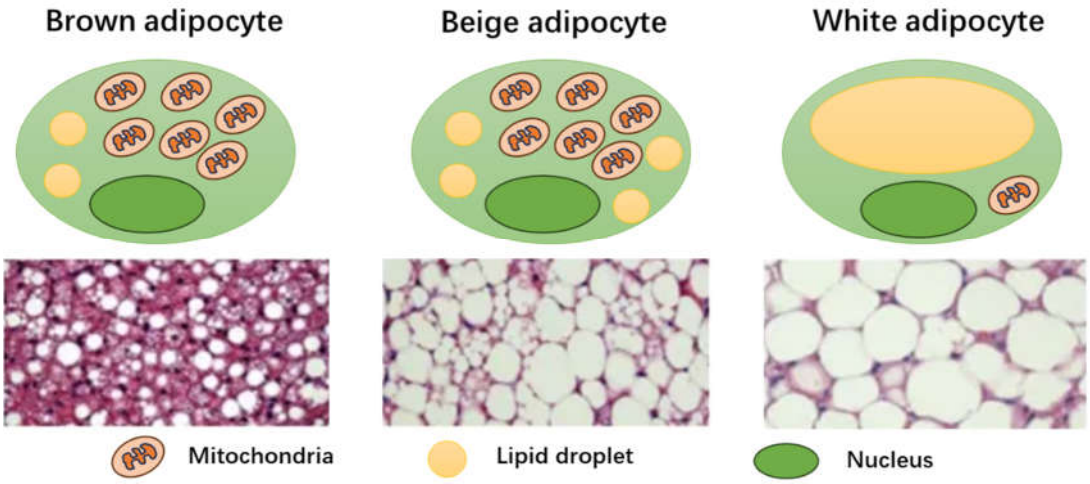


Figure 6. Schematic diagrams of three types of adipocytes. Brown and beige adipocytes have multilocular lipid droplets and densely-packed mitochondria. White adipocytes have unilocular lipid droplets and few mitochondria.[140]

Activating thermogenesis in beige and brown adipocytes, as well as regulating the number of beige adipocytes, are potential strategies to combat obesity. As reviewed by Wang and Seale, to maintain a certain number of beige adipocytes in WAT depots, ongoing stimulations including cold exposure and β3-adrenergic agonist are required. The source of beige adipocyte can be either precursor cells in WAT or mature white adipocytes. In inguinal WAT, different precursors such as mural cells expressing Ebf2 and smooth muscle cells expressing Acta2 and Myh11 differentiate into beige adipocytes through promotion by transcription factors such as Ebf2, Prdm16, Zfp516,

and Pgc1α. In inguinal WAT, beige adipocytes and white adipocytes are mutually transformational; thus beige adipocytes transform into white adipocytes when the animals have warmed up, while white adipocytes transform into beige adipocytes under conditions of cold exposure or β3-adrenergic agonist. However, in epididymal WAT, white adipocytes and brown adipocytes do not transform into each other, the only way being via beige adipocyte generation with bipotent preadipocyte differentiation being stimulated by cold exposure or a β3-adrenergic agonist.[140]

1.3.2.4 The function and regulation of Ca^{2+} signalling in adipocyte differentiation.

As described in previous paragraphs, changes in intracellular Ca^{2+} constitute a universal signalling mechanism that mediates a variety of critical physiological processes. For differentiation, studies have shown that intracellular and extracellular Ca^{2+} synergistically regulate the process of cardiomyocyte differentiation from pluripotent stem cells via regulation of the Ca^{2+}/CaM/GATA-4 pathway and CaMKII pathway.[141] However, the role of Ca^{2+} signals as mediators of differentiation of other cell types, particularly adipocyte differentiation, remains far from clear. Previous research has shown that pharmacologically induced Ca^{2+} changes by an endoplasmic reticulum Ca^{2+}-ATPase inhibitor can prevent adipogenesis by inhibiting the post confluent mitotic phase of the differentiation process in preadipocytes *in vitro*. However, at the early stage of differentiation, the same Ca^{2+}-ATPase inhibitor was shown to stop cell proliferation

and DNA replication, which help cells enter a growth inhibition stage and thus they can be ready to receive lipogenesis signals.[142] Although the results seems interesting, such approaches are unlikely to mimic the complex spatiotemporal Ca^{2+} signalling patterns that may be occurring during endogenous differentiation.

In terms of downstream effectors of Ca^{2+} signals during adipocyte differentiation, calpain, a Ca^{2+}-activated protease, was shown to be necessary for the differentiation from preadipocytes to adipocytes. Calpain was originally expressed by preadipocytes, however, there was evidence showing that the expression decreased during the process of differentiation. The inhibition of calpain also inhibits the expression of adipocyte gene C/EBPα through intercepting the cAMP pathway initiated by IBMX, which would prevent the cells from gaining adipocyte phenotypes.[143] Another study altered Ca^{2+} levels by treatment of extracellular Ca^{2+}, and its results showed that enhanced Ca^{2+} levels activated CaMKII and PI3K/Akt-FoxO1 pathways to initiate adipocyte differentiation in mesenchymal stem cells, and also that this effect was inhibited by a Ca^{2+} chelator, CaMKII inhibitor, and PI3K inhibitor, indicating that Ca^{2+} activated kinase CaMKII is a critical downstream effector of Ca^{2+} signals in adipocyte differentiation.[144] In addition, a Ca^{2+}/calmodulin-regulated serine/threonine phosphatase, calcineurin, was also shown to be involved in an early step of the adipogenic cascade which ultimately results in the expression of PPARγ and C/EBPα.[145]

These results raised the question of whether these downstream effectors were regulated by specific upstream Ca^{2+} signals during adipocyte differentiation, or to be more specific, whether the three primary Ca^{2+}-mobilizing messengers, inositol trisphosphate (IP_3), cyclic ADP ribose (cADPR), and nicotinic acid adenine dinucleotide phosphate (NAADP) are involved in adipocyte differentiation by exclusively regulating a specific downstream effector. As was described in previous paragraphs, IP_3 and cADPR release Ca^{2+} from the endoplasmic reticulum (ER) via IP_3 receptors (IP_3Rs) and ryanodine receptors (RyRs), respectively.[146] In contrast, NAADP targets a Ca^{2+} store located in endolysosome-like acidic organelles.[147] Importantly, these signalling pathways seem not to be independent, and there exists a complex interrelationship in which NAADP triggers local Ca^{2+} release from acidic organelles which stimulates global Ca^{2+} release from the ER via IP_3Rs and RyRs.[148] Recent evidence also indicated that this relationship is bidirectional; thus Ca^{2+} released from the ER can activate the NAADP pathway both by stimulating Ca^{2+}-dependent NAADP synthesis and by activating NAADP-regulated Ca^{2+} channels.[149] The identity of such NAADP-regulated Ca^{2+} channels remains controversial. In line with their assumed location in acidic organelles, studies by my lab and others have identified the TPCs as endolysosomal ion channels and integral components of the intracellular receptor for NAADP.[150–154] In addition, gene elimination of Tpcn1 and Tpcn2 was shown to impair the ability of mouse embryonic fibroblasts (MEFs) to mediate NAADP-triggered Ca^{2+} signalling *in vitro*.[154]In my study, I put emphasis on the investigation of the role of TPC2 in adipogenesis, to be specific,

the upstream Ca^{2+} triggers and the downstream effectors' involvement with TPC2.

1.4 Intracellular Ca^{2+} signalling in virus infection with a particular focus on SARS-CoV-2.

1.4.1 The function of the Ca^{2+} signalling system in viral infection, particularly SARS-CoV-2 infection.

The COVID-19 outbreak of 2019, caused by severe acute respiratory syndrome coronavirus 2 (SARS-CoV-2), led to a global pandemic in 2020-2022. A multiplicity of studies were carried out into the route of SARS-CoV-2 infection as well as the mechanism of this disease. As Ca^{2+} signals play critical roles in infection by diverse viruses, some studies focused on targeting Ca^{2+} signalling pathways as therapeutic strategies.

As an important second messenger, Ca^{2+} has essential functions in many physiological processes through controlling various cell pumps, ATPases, ion channels, and uniporters at the cellular level. In viral infection, the Ca^{2+} signalling system is severely affected in the host cells, while it also has important functions in the virus-host cell interactions.[155] Ca^{2+} signalling is one of the most common host cell signalling cascades which tend to be dysregulated during infections, since causative agents hijack Ca^{2+} signalling cascades of host cells for their own benefit.[156] Previously, researchers demonstrated that Ca^{2+} modulates the pore charge and selectivity of the envelope protein, which is a viroporin related to virulence, in SARS-CoV viruses.[157]

Inflammasomes, which are protein complexes activating caspases upon the detection of pathogen-associated molecular pattern (PAMP) signals and producing cytokines to initiate cell death, were also shown to be activated by Ca^{2+}.[158–160] For SARS-CoV-2, a recent study has pointed out that Ca^{2+} is likely to bind to six acidic residues located on the fusion protein of the SARS-CoV-2 spike protein.[161] This finding directly indicated that Ca^{2+} channel inhibitors could be a potential treatment strategy for COVID-19.[162]

1.4.2 TPC-mediated endo-lysosomal Ca^{2+} signalling in virus infection, and its potential functions in COVID-19.

The lysosomal Ca^{2+} handling machinery was shown to have been utilized by viruses to enter host cells. An important study revealed that the trafficking of Ebola virus was via endosomal vesicles, and that genetic knockout of two pore channels (TPC) on endosomes in the mouse embryonic fibroblasts can inhibit virus trafficking and thus prevent infection.[163] A later study further revealed that Ebola viruses enter cells through endolysosomes that contain both Niemann-Pick C1 (NPC1) and TPC2.[164] A subsequent study reported that a mammalian TPC blocker, virtually screened from a database of ~1500 FDA approved drugs, can inhibit entry of Ebola viruses into host cells (Table 1).[165] Furthermore, a recent study reported single-molecule FRET (smFRET)-imaging results which showed that Ca^{2+}, together with pH and NPC1, induces conformational changes to the envelope glycoproteins (GP) which permits virus-liposome lipid mixing and results in virus entry.[166] Similar to the situation with Ebola viruses, TPCs also play

vital roles in Middle East Respiratory Syndrome coronavirus (MERS-CoV) infections, with NAADP-triggered Ca^{2+} signals being shown to be involved in the translocation of MERS pseudo virions, and gene editing of the TPCs impairing the translocation of MERS-CoV via endolysosomes (Table 1).[167] Similarly, endo-lysosomal Ca^{2+} release through TPC1/2 has been shown to have functions in Merkel cell polyomavirus and simian virus 40 infection (Table 1).[168] At the early stage of the COVID-19 pandemic, a study revealed that TPC2, as a downstream mediator of $InsP_3$ signalling, is critical for the entry of SARS-CoV-2 via binding with the receptor human angiotensin converting enzyme 2 (hACE2) that initiates endocytosis.[168] In my present study, I investigated whether the infection of pseudo-virus has any interrelationship with TPC1/2, whether the expression of TPCs is altered by pseudo-virus infection, and whether pseudo-virus infection processes are affected by TPC gene modification, as well as studying which upstream or downstream effectors may be involved.

Table 1. The outcomes of viral interaction with host cell lysosomal Ca^{2+} signalling mediated by TPCs.[156]

Virus	**Viral Protein**	**Host target**	**Effect on host cell Ca^{2+} signalling**	**Relevance to viral pathogenesis**	**Reference**

Ebola virus	Not known	TPC2	Ca^{2+} release from lysosomes	EBOV entry and infection	163–165
Marburgvirus	Not known	TPC2	Ca^{2+} release from lysosomes	Marburgvirus infection	
Polyomavirus	Not known	TPC1/2	Ca^{2+} release from lysosomes	Viral entry	168,169
MERS-CoV	Furin	TPCs	Ca^{2+} release from lysosomes	Viral entry	167
SARS-CoV-2	Not known	TPC2	Ca^{2+} release from lysosomes	Viral entry	168

1.5 The aims, questions, and hypothesis before this study, and proposed solutions.

In this study, the metabolic characters of TPC gene-edited mice were investigated mainly from two aspects. The first was how TPCs participate in the exocrine function of pancreatic acinar cells. And the second was whether and how TPCs take part in the process of adipocytes differentiation in stem cells. In addition, a preliminary study was carried out into whether and how TPCs have effects on SARS-CoV-2 virus infection.

The study was based on some previous recognitions and speculations. First, previous research indicated that TPC-KO mice are leaner and these mice have an abnormal amount of lipase in their digestive track (unpublished findings, personal communication by John Parrington). Second, in the process of adipocyte differentiation, TPC2 expression was found transiently up-regulated (unpublished findings, personal communication by John Parrington). Thirdly, naringenin, a TPC inhibitor was reported to fight SARS-CoV-2 infection, indicating that TPC could be playing a role in SARS-CoV-2 infection.

The detailed aims, questions, hypothesis, and solutions have been listed in the following table (Table 2).

Table 2. Aims, questions, hypothesis, and solutions for the studies in this thesis.

Aims of each chapter	Unsoved questions before this study	Hypothesis before investigation	Solutions in this study
To investigate why TPC1 KO mice have abnormal lipase production in their digestive track. (Chapter 3)	Is the activity of lipase influenced by TPC KO in pancreatic acinar cells? What about other digestive enzymes?	The activity of digestive enzymes within pancreatic acinar cells are altered by TPC KO.	The activities of lipase, amylase and elastase were tested in isolated pancreatic acinar cells.
	What happens to the cell components of pancreatic acinar cells after TPC1 KO?	The changes of cell components with or without TPC KO can be discovered.	Proteomic analysis was performed on the whole cell protein extracts, and Raman Spectroscopy was employed to detect single-cell components.
To investigate why TPC2 mRNA expression is transiently up-regulated during adipocyte differentiation. (Chapter 4)	What has caused the up-regulation of TPC2 transcription during adipocyte differentiation?	One or more components in the differentiation medium induces TPC2 up-regulation.	Which components in the differentiation medium caused the over-expression of Tpcn2 was investigated.
	Does TPC2 have any functions in adipocyte differentiation?	TPC2 KO preadipocytes have impaired differentiation.	The differentiation of isolated preadipocytes was studied.
	What is the down-stream effector of TPC that finally regulates adipocyte differentiation?	Calpain (a cytosolic protease, a Ca^{2+}-activated effector in adipocyte differentiation) may be activated by TPC2 mediated Ca^{2+}.	The change of calpain activity was investigated during adipocyte differentiation.
To investigate whether TPCs play a role in SARS-CoV-2 viral infection. (Chapter 5)	Do TPCs have an effect on hepatocytes against SARS-COV-2 pseudo virus infection?	Similar to MERS and Ebola, TPCs may have effects on SARS-CoV-2 viral entry.	T he infection efficiency of pseudo virus on TPC-silenced hepatocytes was tested.
	What is at the down-stream of TPCs in SARS-CoV-2 pseudo virus infection?	SARS-CoV-2 pseudo virus infection may have effects on TIMP-1 expression via TPCs.	TIMP-1 expression was detected in WT *vs.* TPC1 KD hepatocytes with or without PSV infection.

Chapter 2: Materials and Methods

2.1 Materials.

2.1.1 Animals.

Animal experiments in this study were performed in accordance with UK law (Animals [Scientific Procedures] Act 1986) and were approved by the University of Oxford Pharmacology Ethical Review Committee and the national guidelines under which the institution operates. Mutant mice (homozygote $Tpcn1^{Gt(XG716)Byg}$ and homozygote $Tpcn2^{YHD437}$) and wild-type littermates were maintained in Biomedical Science Building at the University of Oxford and delivered by Biomedical Services.

All mice, including wild-type, mutant, and high-fat-diet (HFD) fed, were given ad libitum access to food and water unless otherwise stated. The amount of food was strictly controlled during high-fat-diet feeding to ensure both control and HFD mice were taking in the same amount of food, while water access was not restricted. The digestive tract emptying state was not controlled because the conditions do not permit.

2.1.2 TPC KO mice line.

Tpcn1 KO (homozygote $Tpcn1^{Gt(XG716)Byg}$) and *Tpcn2* KO (homozygote $Tpcn2^{YHD437}$) mice, previously established by the Parrington/Galione labs (Department of Pharmacology, University of Oxford) were used (Figure 7). Strain-matched (C57BL/6)

WT mice were used as controls.

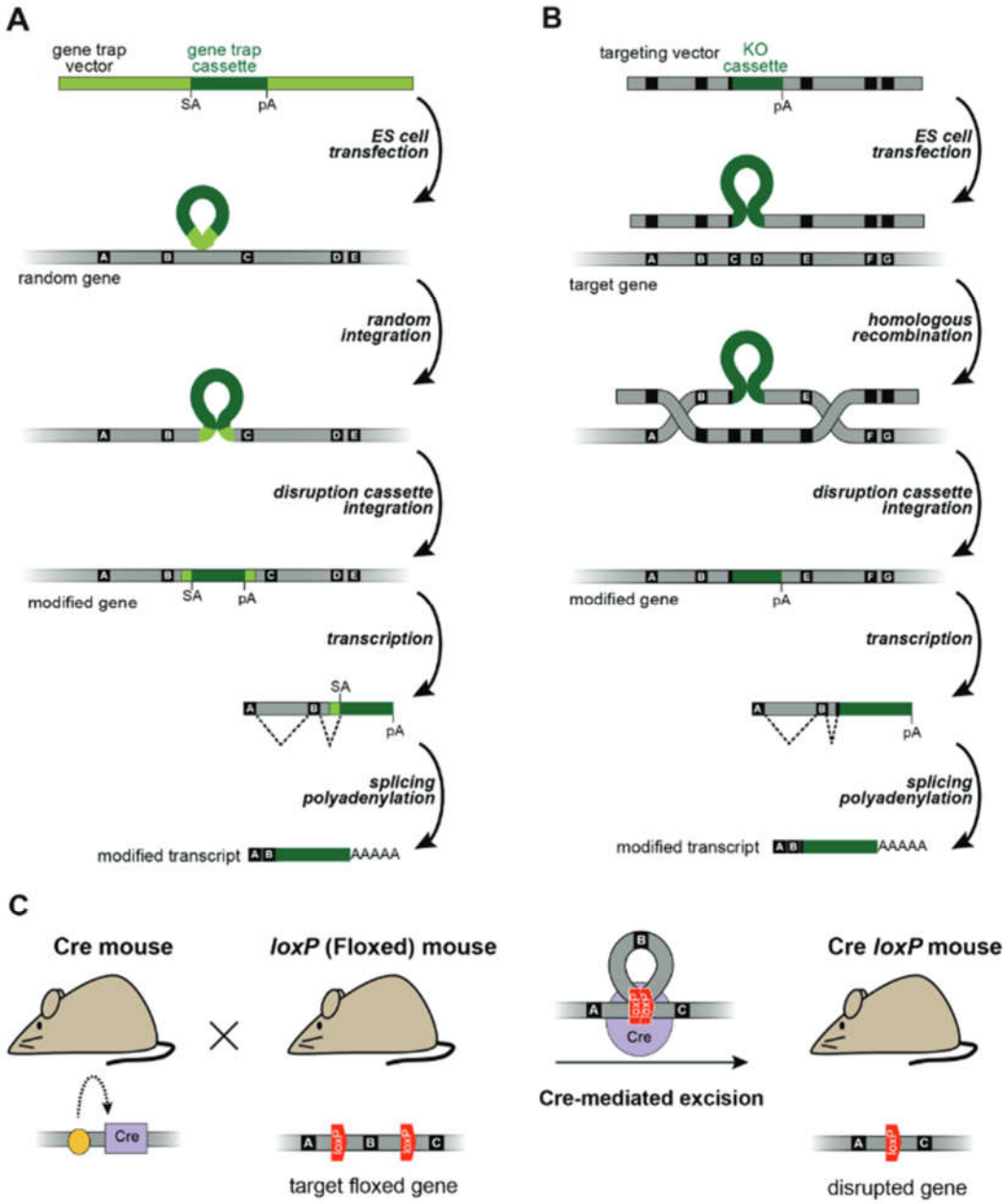


Figure 7.[170] Schematic diagram for mutant mouse line established by Cre loxP. Cre loxP-based gene targeting is a two-step process (A/B). The first step is to introduce loxP sequences into the genome of embryonic stem cells, which can be achieved through the design of target vectors

and the screening of homologous recombinants. The next step is to achieve Tpcn1/2 genetic modification, the gene between loxP sites then being knocked out. (Introns are represented in grey, exons are represented in black, and labelled with letters and disruptive sequences are in green. SA-splice acceptor sequence, pA - poly-adenylation signal.)[170]

Mice were killed by cervical dislocation or asphyxiation. All experiments and procedures were approved by the local animal welfare and ethics committee of the University of Oxford, in accordance with UK guidelines for the use of experimental animals.

Both TPC KO and WT mice are randomly picked for any experimental process in this study, including body composition detection, primary cell isolation, high-fat diet breeding, etc.

2.1.3 High-fat-diet mice model establishment.

High-fat-diet (HFD) C57Bl6 mice were fed with a special high-fat diet (HFD) by adding an additional 14-15% fat and 0.15-0.2% cholesterol (provided by Dr. Kai Nie from SJTU) since they were 2 weeks old. Both normal and HFD mice were kept under the same conditions and were provided with the same amount of food.

Restricted by conditions, high-fat-diet (HFD) mice used in Chapter 3 for pancreatic enzyme activity tests, were fed with normal forage with additional 15% fat without any

cholesterol.

2.1.4 Culture of C3H10T1/2 cells.

To better mimic the differentiation of adipocytes in the body, I chose mesenchymal stem cell (MSC) lines to develop the cell models. MSCs are pluripotent stem cells, which possess all the characteristics of stem cells, namely the capacity for self-renewal and multidirectional differentiation. C3H10T1/2 cells (clone 9, passage 18) were obtained from the American Type Culture Collection (ATCC). Cells were thawed in a 37℃-water bath and collected by 2 minutes centrifugation. Then they were washed with PBS twice and incubated at 37°C with 5% CO_2 in Dulbecco's modified Eagle's medium (DMEM) (Gibco, 61965) supplemented with 10% fetal bovine serum (FBS) and 0.5-1% penicillin/streptomycin. Medium was refreshed every second day. Cells were passaged before they exceeded 80% confluence. Cells were screened for mycoplasma contamination using a MycoAlert Mycoplasma Detection Kit (Lonza).

2.1.5 Adipocyte differentiation of C3H10T1/2 cells.

Insulin, dexamethasone, and 3-isobutyl-1-methylxanthine (IBMX) synergistically result in adipocyte differentiation in C3H10T1/2 mesenchymal stem cells. The cocktail of these three components with growth medium was used as differentiation medium in this study. This protocol was developed based on protocols previously used in our lab with slightly changed dosages of insulin and dexamethasone.[171]

To stimulate stem cells to differentiate into adipocytes, and meanwhile, to inhibit them differentiating into other types of cells such as osteoblasts, the transcription level of certain adipogenic genes needs to be enhanced. The most important adipogenic genes include C/EBPα, C/EBPβ, and PPARγ.[172]

The transcription of C/EBPβ is mediated by cAMP-CREB and cAMP-KLF signalling. IBMX elevates the level of cAMP by inhibiting its phosphodiesterase and thus mediates the C/EBPβ up-regulation. The up-regulation of CEBPβ then stimulates C/EBPα and PPARγ transcription which directly facilitates adipocyte differentiation. Insulin exerts its adipogenic function through three pathways. First, insulin inhibits FOXO1 which is an endogenous inhibitor of PPARγ transcription. Second, insulin directly triggers PPARγ transcription by up-regulating sterol regulatory element-binding proteins (SREBP). Thirdly, as a type of growth hormone, insulin has an activation effect on CREB, which stimulates C/EBPβ transcription and then up-regulates C/EBPα and PPARγ. Dexamethasone is a glucocorticoid that binds to its receptors and activates the transcription of both C/EBPβ and PPARγ.[173]

Cells were randomly selected for differentiation. Differentiation was induced in C3H10T1/2 cells at 1-2 days post-confluence, designated as ‘day 0’. What calls for special attention is that cells cannot be overspread in the culture vessel; there must be some interspace for cells to grow since cells tend to swell during adipocyte differentiation. On day 0, the growth medium was discarded, and cells were washed

twice with PBS and supplied with differentiation medium which contained growth medium with the addition of 1 μM insulin, 0.5 mM 3-isobutyl-1-methylxanthine (IBMX), and 1 μm dexamethasone. After 2-3 days, the differentiation medium was replaced with growth medium with the addition of 1 μM insulin (0.5 units), and after another 2 days, this was replaced with growth medium. Differentiation proceeded for a total of 8 days, with the base DM refreshed every 2 days. For cells under the untreated control condition, cells were maintained in GM, and passaged on day 2, day 4, and day 6.

2.1.6 Isolation, culture, and differentiation of primary preadipocyte cells.

Abdominal adipose tissue from the abdominal fat pad of C57Bl6 mice was obtained at the age of 10-18 weeks. The mice for abdominal adipose tissue separation were randomly picked and their abdominal adipose tissue was mixed for primary preadipocyte isolation.

A preadipocyte isolation kit (ab196988, Abcam) was used for preadipocyte isolation and purification according to the manufacturer's instructions. Tissues were minced thoroughly with scissors and digested for about 30 minutes with 0.15% collagenase I (aliquoted and stored at -20 °C 2 months before use). During digestion, tubes were gently vortexed for 10-15 seconds every 5 minutes to assure complete digestion. After

digestion, collagenase stopping buffer was added directly to the tissues and the sample centrifuged at 1000 rpm for 2 minutes and washed with PBS for 2-3 times. Before the last wash, cells were incubated with 10% red blood cell lysis buffer at room temperature. Since preadipocytes are very delicate, all solutions and buffers were equilibrated to 37°C before use. The culture vessel was incubated in DMEM/F12 medium at 37°C for 1-2 hours before plating to increase preadipocyte binding. Cells were split before reaching 70% confluence. The preadipocytes were cultured in DMEM/F12, supplemented with 10% fetal bovine serum (FBS) and 0.5-1% penicillin/streptomycin, and left for 48 hours until adherence. Differentiation was induced following the same standard differentiation protocol as used for C3H10T1/2 cells but replacing DMEM with DMEM/F12. Since preadipocytes can only be passaged for 3-5 times according to the cells' condition, preadipocytes under the untreated control condition were used at 1-2 days after isolation.

2.1.7 Primary mesenchymal stem cell isolation.

The mice were randomly picked and their bone marrow was mixed for primary mesenchymal stem cell isolation. The femoral bone of C57Bl6 mice was collected from the acetabulum and soft tissue was removed. To obtain the bone marrow, a size 18 needle was passed through the bottom of a 0.5 ml microcentrifuge tube. Then the bone was put into the tube with the knee downwards and the 0.5 ml microcentrifuge tube was put into a 1.5 ml microcentrifuge tube and centrifuged for 15 seconds in a

microcentrifuge tube at 8000 g. Marrow cells were extracted using a 10 ml syringe and transferred to a 50 ml conical tube and the volume increased to 10 ml using PBS. Cells were then centrifuged at 1200 rpm for 8 minutes. Cells were then transferred to DMEM/F12 (Thermo-fisher) with 5% FBS and 1% PS and cultured at 37%, 5% CO_2.

2.1.8 Hepatocyte isolation.

PBS with 0.1% collagenase1 was heated to 37℃ and perfused into the hepatic portal vein very slowly until the whole liver turned pale. Then the liver was transferred to PBS with 0.15% collagenase1 and 0.1% trypsin inhibitor and incubated at 37℃ for 15 minutes. The supernatant liquid was centrifuged at 800 rpm for 2 minutes. 2 ml ACK lysis buffer was added and mixed well with the cells. Then the sample was centrifuged again at 800 rpm. Hepatocytes were resuspended with DMEM/F12 (Thermo Fisher) with 5% FBS and 1% PS.

2.2 Cell transfection and infection.

2.2.1 Tpcn1 gene silencing (siRNA).

siRNA sequences were designed by Biodev DSIR. Both pancreatic acinar cells (PACs) and hepatocytes were freshly isolated from C57BL6 mice. siRNA (ordered from GenScript) was transfected into cells by application of lipofectamine RNAiMAX (Thermo Fisher). The cells were incubated with siRNA for 20 mins then PACs were

used after 5 hours culture while hepatocytes were used after 24 hours culture. siRNA sequences designed by Biodev DSIR were based on FASTA results provided by NCBI. According to the principles for siRNA sequence design, two pairs of AS and SS sequences had been screened from hundreds of possible ones (Table 2). 'AS' refers to antisense strand which is complementary to the target sequence, and 'SS' refers to sense strand, which is the same as the target sequence. These strands were annealed into a siRNA double-stranded complex with dTdT (DNAs) replacing the two bases at the 3 'end to enhance the stability of the complex (Figure 8).[174]

Table 3. Sequence of the small interference RNA used for TPC1 silencing. SS- Sense strand, which means the sequence is the same as the target sequence. AS- Antisense strand, which means the sequence is complementary to the target sequence.

Position	SS Sequence	AS Sequence
1811	CGACAACAACUCAGCUGUAUG	UACAGCUGAGUUGUUGUCGGG
2795	GGUGGUUGGUUGUGGGUUAUA	UAACCCACAACCAACCACCCU

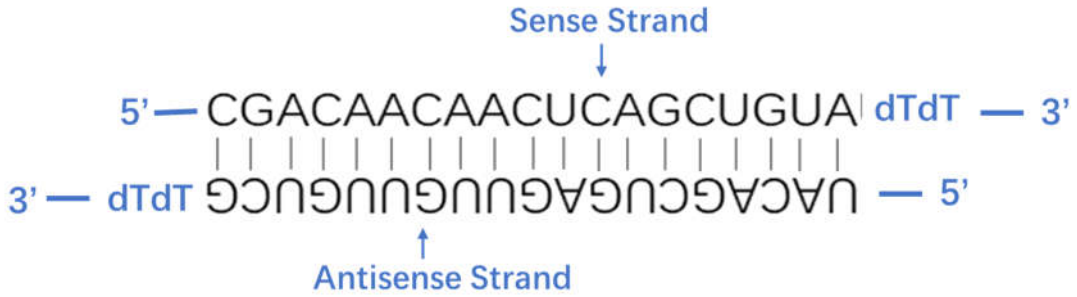


Figure 8. A schematic diagram of the composition of the siRNA double-stranded complex.

(dTdT- DNAs replacing the 2 bases at the 3 'end which enhances the stability of the complex.)

2.2.2 Lentiviral expression of TPC2.

This part of the experiments was completed by Dr. Ruth Tunn during her study in the lab. Lenti-X HEK293T cells (Clontech) were grown at 37℃, 5% CO_2 in DMEM supplemented with 10% tetracycline-free fetal calf serum (BioSera), 1mM sodium pyruvate, 100U/ml penicillin-G-sodium, 100μg/ml streptomycin sulphate and 2mM L-glutamine. When 50-80% confluent, cells were co-transfected with viral vector and Lenti-X HT packaging mix (Clontech, 15 μl per 3 μg vector) using a jetPEI system (Polyplus transfection) according to the manufacturer's instructions. Medium was harvested 48 hours after transfection, filtered through a sterile 0.45 μm polyethersulfonate filter (Whatman puradisc 25 AS), and checked for the presence of infectious virons by applying a sample to Lenti-X GoStix (Clontech). When cells reached 50% confluence, mCherry, mCherry-tagged TPC lentiviral medium, or control medium was added (1 ml/T75 flask) along with polybrene to 4 μg/ml final concentration.

2.2.3 Pseudo-virus (PSV) infection.

Cells were randomly picked for either PSV infection or normal procedure. Both acinar cells and hepatocytes were seeded and incubated in a 6-well plate at 37℃ in an incubator supplied with 5% CO_2 2 days before PSV infection. One hour before PSV

infection, cells were transferred to the medium containing Polybrene, then they were mixed evenly with SARS-CoV-2 pseudo-virus at a concentration of 100-200 ul/well for hepatocytes and 100, 150, 200, 250, 300 ul/well for pancreatic acinar cells. Cells were incubated at 37℃ for 1 hour. Since the PSV was marked with GFP, the efficiency of infection was measured with a microplate reader (PerkinElmer EnSpire) at 488 nm after 3-5 hours of PSV infection.

2.3 Cell staining.

2.3.1 Oil red O staining.

Oil red O is used in order to show the fat in tissues. Oil red O is a fat-soluble dye, highly soluble in fat and less soluble in water, and can specifically colour the neutral fat such as triglyceride in tissues. In the experiment, 0.2% Oil Red O (w/v) was dissolved in isopropanol and was filtered thoroughly after dissolution. Cells after or during adipocyte differentiation were washed 2-3 times with PBS and fixed in 4% paraformaldehyde for 30 minutes at room temperature. Fixed cells were incubated for 5 minutes in 60% isopropanol, then incubated in the filtered Oil Red O solution for 10 minutes, and then washed with PBS for 5 minutes before being imaged using a Leica DM 500B microscope.

2.3.2 AdipoRed staining and quantification.

AdipoRed is a reagent that enables the quantification of intracellular lipid droplets in a high throughput manner. Before the process of dyeing, the outside wall (except the bottom) of each well of a 24-well plate was painted black with a marker in order to avoid fluorescence cross contamination. Cells after or during adipocyte differentiation were seeded in this 24-well plate and incubated for 2 days. Cells after or during adipocyte differentiation were randomly picked for AdipoRed staining.

On the day of dyeing, cells were washed 2-3 times with PBS , and 30 ul AdipoRed (Lonza) reagent in 0.5 ml PBS was added to each well. To assure a homogeneous dispersion of the AdipoRed reagent, the solution was pipetted up and down 3 times in each well. Cells were incubated with AdipoRed reagent for 15 minutes at room temperature. They were then washed three times with PBS before being observed under a fluorescence microscope. Fluorescence was measured under excitation of 488nm using a Typhoon 9400 Variable Mode Imager equipped with a BP 580/30 emission filter. The photomultiplier tube (PMT) was adjusted to maximize the signal while avoiding saturation, and resolution was 100 μm. The relative fluorescence unit (RFU) was quantified using Fiji/Image J software. Data were normalized to an average background of empty wells or, in the case of lentivirally-infected cells, to an average reading for cells infected with the relevant lentivirus but not treated with AdipoRed, to control for overlap between mCherry and AdipoRed fluorescence emission.

2.4 Proteomic analysis.

2.4.1 Pancreatic acinar cell protein extraction.

Suspended cultured primary acinar cells were scrapped from culture vessels using a cell scraper and transferred to the centrifuge tube. Cells were centrifuged at 1000 rpm for 3 minutes, then culture medium was discarded. Cold PBS was used for cell resuspension and cells were centrifuged at 1000 rpm for another 3 minutes. Cells were washed 3 times to make sure they were clear of culture medium and then transferred into 1.5ml EP tubes. Lysis buffer with 10% Triton X-100, 10% sodium deoxycholate, 1% phosphatase inhibitor, 0.1% protease inhibitor, and 0.5% 100mM PMSF, was added to cells. The EP tube was placed on ice for 30 minutes and the contents gently mixed by vortex for 30 seconds every 10 minutes. The mixture was then centrifuged at 4℃, 14000rpm for 15 minutes. Supernatant was collected and sediment was discarded. The protein was quantified using the BCA method (as described below). The protein was aliquoted and stored at -70℃ for later use.

2.4.2 BCA method for determination of protein concentration.

The BCA protein quantitative method works by the reduction of Cu^{2+} into Cu^{+} by proteins in an alkaline environment in what is known as the biuret reaction. Individual amino acids and dipeptides are unaffected in the biuret reaction, but tripeptides as well as larger peptides or proteins react to produce pale blue to basket purple complexes with

absorption peaks at 540 nm. A copper bivalent ion combines with four to six nearby peptides to form a coloured chelate. The intensity of colour produced is proportional to the number of peptide bonds involved in the reaction (Figure 9). In my experiments, standard Pierce BCA Protein Quantification reagents (Thermo Scientific, 23227) were employed to detect protein concentrations. Reagent A, a carbonate buffer containing the BCA reagent was mixed with 2% reagent B which is a copper sulphate solution, and the mixture was added to protein samples and turned purple at 37℃ after 30 minutes in the presence of the protein. The results were read by a spectrophotometer at 562nm. A standard curve was drawn using samples with known concentrations and the concentrations of samples under test were calculated.

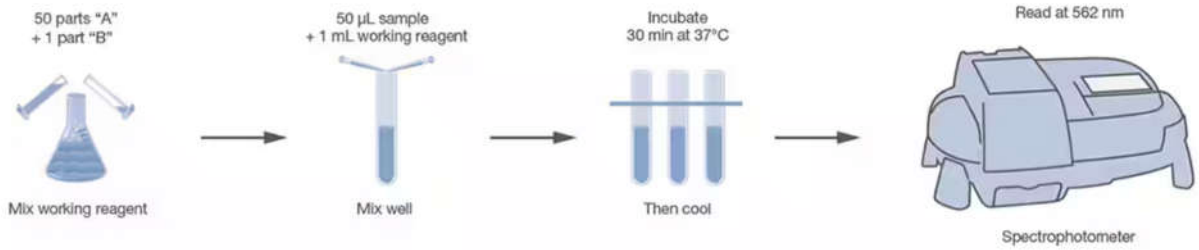


Figure 9. Experimental scheme of BCA protein quantitative assay.

2.4.3 Fluorescence and immunofluorescence imaging.

Three coverslips were placed in culture vessels and C3H10T1/2 cells were split and seeded 2 days before use. Coverslips were moved out of the culture vessel and washed twice in warm PBS. Then cells were fixed for 20 minutes in 4% paraformaldehyde at room temperature and washed with PBS three times. Then the coverslips were mounted

with ProLong Gold antifade mounting medium (Invitrogen) for fluorescence observation. For cells processed for immunofluorescence, cells were not mounted after fixation; instead they were permeabilized in PBS/0.5% Triton X-100, then blocked in Fast Blocking Western blocking buffer (Yeasen) followed by incubation in 5F8 monoclonal against mCherry (left by Dr Ruth Tunn, supplied by A. Rottach, University of Munich) diluted 1:500, for incubation for 1 hour at room temperature, and incubated in goat anti-rat Alexa Fluor 488 (Invitrogen), 5μg/ml. Coverslips were mounted with ProLong Gold antifade mounting medium (Invitrogen) and slides were viewed using a Zeiss Meta 510 confocal LSM.

2.4.4 TIMP-1 expression level detection (Western Blot).

Whole cell proteins from pancreatic acinar cells were extracted as previously described. Protein was stored at -70℃ and thawed at room temperature before use. The BCA method was used for protein quantification. Then 40μg of total protein per sample was separated by electrophoresis on sodium dodecyl sulfate (SDS)-polyacrylamide gels (90%) and transferred to PVDF membrane. TIMP-1 primary antibodies (ab179580, Abcam) were added to TBS buffer (Thermo-Fisher) at 0.05% dilution. The PVDF membrane was incubated with primary antibodies on a bottle shaker at 4℃ overnight. On the next day, the membranes were washed with TBS for 3 x 10 minutes to ensure they were clear of primary antibodies. Then membranes were blocked with 5% skimmed milk powder in TBS or Fast Blocking Western blocking buffer (Yeasen) and

incubated at room temperature for 1 hour before being washed in TBS for 10 minutes twice. A secondary antibody, goat anti-rabbit IgG H&L (Alexa Fluor® 488) (ab150077, Abcam) was added at a 0.01% dilution in PBS and was incubated for 1 hour at room temperature. The membrane was then washed 3 x 10 minutes to get rid of secondary antibodies. The result was detected by Invitrogen iBright CL750 system and the blots were analyzed using a Fiji/image J software.

2.4.5 p-CREB and cytochrome c expression level detection (Western Blot).

A similar protocol as for TIMP-1 expression level detection was used for p-CREB and cytochrome c expression level detection. But different to TIMP-1, the protein extract was not only from pancreatic acinar cells but also from hepatocytes. 50µg of total protein per sample was separated by electrophoresis on sodium dodecyl sulfate (SDS)-polyacrylamide gels (90%) and transferred to PVDF membrane. A primary antibody to p-CREB (sc-81486, ImmunoCruz) was added to TBS at 0.1% dilution and incubated at 37℃ for 30 minutes. The same process was employed for another group of protein samples with a different primary antibody, to anti-cytochrome c (ab110325, Abcam). The membrane was washed 3 x 10 minutes with TBS, then blocked with 5% skimmed milk powder in TBS or Fast Blocking Western blocking buffer (Yeasen). Then the membrane was washed in TBS for 10 minutes twice. A secondary antibody, goat anti-mouse IgG (H^+L) Cross-Adsorbed Secondary Antibody, Alexa Fluor™ 488 (AB-

2534069, Invitrogen, supplied by Dr. Kai Nie from SJTU) was added at a 0.02% dilution and the membrane incubated for 1 hour at room temperature. The membrane was detected using the Invitrogen iBright CL750 system.

2.4.6 iTRAQ and DIA proteomics and their data analysis.

iTRAQ technology, which was first introduced by Applied Biosystems Incorporation, refers to isobaric tags for relative and absolute quantitation (iTRAQ), and is a new and powerful method for absolute and relative quantitative study of four samples simultaneously. Proteins from pancreatic acinar cells were extracted as previously described. Cell lysis buffer with Triton X-100 was employed due to the mild strength of RIPA buffer which made it difficult to dissolve membrane protein (organelle protein, cell membrane protein contains GPCR), nuclear protein (H3), DNA binding protein, histone protein, or protein with a low expression level, and some phosphorylated protein signalling pathway proteins (such as PI3K/Akt /mTOR). The proteins were cleaved to peptides and differentially labeled with iTRAQ reagents. The labelled samples were then mixed together so that they could be compared. After mixing, the proteins were identified by a method of MudPIT multidimensional protein identification and were analyzed by 2D liquid chromatography tandem mass spectrometry. On the basis of mass spectrometry, each peptide fragment was identified by MASCOT and Protein Pilot which are software packages of Applied Biosystems. iTRAQ technology required that the total mass of detection of protein in sample was at

least 50 ug while the minimum concentration was not less than 5 ug/uL, otherwise the isotope cannot be labelled. The label free intensity of more than 1000 proteins in pancreatic acinar cells was detected by HPLC-MS technology, and the proteins whose intensity was sharply changed were detected and shortlisted for further analysis.

2.4.7 Proteomics results analysis.

First, the raw data of intensities were transformed into logarithmic form, followed by quantile standardization using the limma R packet (v3.46.0). The original and standardized signals were combined in a single table to obtain a complete picture of protein expression and function (shown in Supplementary Materials). For comparison of the samples of two groups, the statistically significant differences analysis was conducted using the two-tailed Student's t test, and the proteins were screened with P-value of 0.05 and fold change of 2.0 as thresholds (the table of differentially expressed proteins are shown in Supplementary Materials). The volcano map, scatter map, and protein cluster map were drawn according to the statistical analysis results. For comparison of two samples within each group, fold change was used for differential expression analysis, and a fold change of 2.0 was used as the threshold to screen differentially expressed proteins, and scatter plots and cluster plots of proteins were drawn. The Cluster Profiler R package (v3.18.1) was used to analyze the Gene Ontology and KEGG pathway enrichment of differentially expressed proteins.

2.5 Other quantitative analysis.

2.5.1 Quantitative PCR analysis.

Cells of the same clone but growing in separate culture plates were randomly collected for harvesting. All cells were processed following the same protocols for qPCR.

Total RNA from C3H10T1/2 cells was extracted and purified using a QIAGEN RNeasy mini kit according to the manufacturer's instructions. The RNA concentration was checked using a NanoDrop spectrophotometer and integrity was checked by electrophoresis on a 1.5% agarose gel. cDNA was synthesized from RNA samples using a high-capacity cDNA reverse transcription kit (Applied Biosystems) according to the manufacturer's instructions. The extracted RNA or cDNA synthesized was aliquoted and stored at -70°C until analyzed. A Roche Light Cycler 480 System was used for qPCR. Primers were obtained from former researchers in the lab and were designed using the Roche Universal Probe Library Assay Design Centre. A reaction solution of cDNA (1-5 ng/μl), gene-specific forward and reverse primers (0.1μM each), and Universal Probe Library Probe (0.1μM) in LightCycler 480 Probes Master were mixed. All samples were run in triplicate within each experiment and results were averaged. Cycling conditions were set up as 50°C for 3 minutes and then 95°C for 10 minutes for 30 cycles, then 95°C for 15 seconds, 60°C for 1 minute, then an end cycle at 40°C for 30 seconds. LightCycler 480 SW 1.5 software was used to acquire data and produce

graphs quantifying the fluorescence of each sample plotted against cycle number and the Cp was calculated for each sample. The values for genes of interest were normalized to the averaged housekeeping gene (β-actin, β-tubulin and gadph) value and were recorded as values relative to a control (0-hour timepoint for differentiation time-course experiments, GM or vehicle control for pharmacological interventions).

2.5.2 Tpcn2 level measurements (qPCR).

Since part of the qPCR experiments was completed in Prof. Hong Yu's lab in Shanghai JiaoTong University, the protocols were slightly different because of different reagents and equipment. Complementary DNAs (cDNA) were synthesized by reverse transcription (RT) utilizing NuHi®eRT NH9011 (NuHigh). Amplification was conducted utilizing Power Up SYBR Green Master Mix (Thermo-Fisher). Primers for both Tpcn2 and the housekeeping gene Gadph were designed using online tools of the Roche Universal Probe Library Assay Design Centre (Table 2), and oligos were ordered from GenScript. A Thmorgan Q6-96 qPCR machine was used for qPCR, a quantitation ΔΔCt experiment was set-up, and SYBR Green reagent was selected. Then samples were run under standard ramp speed. The number of cycles was set at 40 and a melt curve stage was added. When the plot of amplification was completed, the Ct value of the amplification curve was calculated automatically by the system with a default threshold line.

Table 4. Forward and reverse primers for the Tpcn2 gene and their GC percentage. Primers were designed using the Roche Universal Probe Library Assay Design Centre.

GC%	Forward primer (5'->3')	Reverse primer (5'->3')
59.97	ACGACTTTGCTGCTGCTTTG	TAACCCACAACCAACCACCC
60.11	GGUGGUUGGUUGUGGGUUAUA	UAACCCACAACCAACCACCCU

2.5.3 TD-NMR scanning for mice body composition.

These experiments were completed by Dr. Ruth Tunn during her time in the lab. Mice was killed by neck-breaking or asphyxia in CO_2 at the ages of 3, 6 and 9 months. The carcasses were thawed at 4°C one day before scanning, followed by 4 hours at room temperature. These frozen-thawed mice were scanned in the same manner as live animals. Mice were weighed then scanned using a Bruker Minispec LF50 Whole Body Composition Analyzer. Fat mass and lean mass data were acquired using Bruker Minispec Plus software.

2.5.4 Calpain activity analysis.

The calpain activity of differentiating primary preadipocytes was measured using an Abcam Calpain Activity Assay Kit (ab65308) according to the manufacturer's instructions. To detect activated calpain in the cytosol, a fluorometric assay was developed based on the detection of cleavage of calpain substrate Ac-LLY-AFC. Undigested Ac-LLY-AFC emits blue light (λ_{max} = 400 nm), but after being digested by

activated calpain, AFC emits a yellow-green fluorescence (λ_{max}= 505 nm). Therefore, the ratio of yellow-green fluorescence and the blue light can be used to quantify the percentage of Ac-LLY-AFC which are digested by activated calpain, which reflects the amount of activated calpain. Pancreatic acinar cells were freshly isolated and collected (around 1-2 x 10^6 cells were required). Cells were washed with cold PBS twice and transferred into 1.5 mL EP tubes. Cells were then resuspended in 100 μL of extraction buffer (supplied in assay kit) and incubated on ice for 20 minutes, with gentle vortexing three times during incubation. Protein extracts were collected by centrifugation for 1 minute in a microcentrifuge (10K x g). Supernatant was transferred to a clean tube and kept on ice. The cell lysate was diluted to 100 ug in 85 uL extraction buffer in each well of 96-well plates. The positive control was carried out with 1 uL active calpain (supplied in the assay kit) dissolved in 85 uL extraction buffer while the negative control was carried out with 1 uL calpain inhibitor in cell lysate in 85 uL extraction buffer. Reaction buffer and calpain substrate were added to samples following the manufacturer's instructions. The samples were incubated at 37ºC for 60 minutes. The fluorescence was measured using a Tecan M200 Pro microplate reader. The relative fluorescent unit (RFU) of Ex/Em = 400/505 nm was calculated for sample groups versus control groups. Each experiment was triplicated, and the results were averaged.

2.5.5 CREB phosphorylation analysis.

Cells were subject to the same lysis procedure as for Western Blot analysis. CREB

levels (total/phosphorylated) were measured using a CREB InstantOne ELISA kit (Invitrogen) according to the manufacturer's instructions.

2.5.6 The quantified analysis of the activation of pancreatic lipase, elastase, and amylase.

Pancreatic acinar cells were freshly isolated as previously described. Isolated cells were suspended in PBS and were smashed by an ultrasonic shatterer Sonics VCX 1500. Then the supernatant was collected for enzyme activity tests. A colorimetric lipase activity assay kit (ab102524) was used for a lipase activity test according to the manufacturer's instructions. The elastase activity was tested by using a fluorometric elastase activity assay kit (ab204730). The detection of amylase was based on the interaction of the substrate with α-amylase and release of the chromophore upon hydrolysis by a α-glucosidase.[175,176] Maltooligosaccharides (G3–G10) linked to a chromophore and azurin cross-linked amylose (provided by Dr. Rui Gao from OCDEM, Radcliff Department of Medicine, University of Oxford) were used as substates. The standard curve was drawn according to the test results of α-amylase (Sigma, A-4551) with a known gradient concentration. Results were read by a multi-functional laser imaging system Typhoon 9400 at absorbance of OD=405 nm.

2.5.7 Analysis of TPCN2 genetic variants in humans.

This part of the experiment was carried out by Dr. Marijana Todorcevic from the Oxford

Centre for Diabetes, Endocrinology and Metabolism, University of Oxford. Abdominal and gluteal subcutaneous adipose tissue biopsies were obtained from 11 healthy females recruited from the Oxford BioBank (OBB), aged 30-50 years with BMI ranging from 22-27 kg/m^2.[177] The study was approved by the Oxfordshire Clinical Research Ethics Committee (08/H0606/107$^+$5) and all subjects gave written informed consent. Stromal vascular fraction (SVF) cells and mature adipocytes were separated from whole adipose tissue biopsies following collagenase (Roche) digestion (1 mg/ml in Hanks' buffered salt solution) and in the case of SVF cells there was additional treatment with red cell lysis buffer. Total RNA was extracted as described by Collins et al.[178] RNA integrity was assessed using a 2100 Bioanalyzer (Agilent Technologies) and samples with a RNA integrity (RIN) number of 8 and above were selected for RNASeq analysis. These samples were sent to the Oxford Wellcome Trust Centre for Human Genetics where a quality control report was generated and a library of read data compiled. Differentially expressed genes were identified by comparing the RNAseq profiles between SVF, mature adipocytes, and the whole adipose tissue samples.

2.5.8 Single-Cell Raman Spectra (SCRS) measurements and data analysis.

8-10 weeks old TPC1, TPC2 and TPC double knock-out mice were randomly picked for pancreatic acinar cell isolation. The isolation processes followed the same protocol described in previous paragraphs.

Freshly isolated pancreatic acinar cells were fixed for 20 minutes in 4% paraformaldehyde at room temperature and washed three times with PBS. Then fixed cells were spread on an aluminum-coated slide and observed under a 100×/0.9 microscope objective. The Raman spectra measurements were carried out by Dr. Jiabao Xu from the Department of Engineering Science, University of Oxford. Single-cell spectra were acquired using an HR Evolution confocal Raman microscope (Horiba) equipped with a 532 nm neodymium–yttrium aluminum garnet laser and 600 grooves/mm diffraction grating. Acquisition time was 20 seconds per spectrum with 4.6 mW laser power and a 1 μm^2 laser spot.[179] Principal component analysis (PCA) was carried out using MultiVariate Statistical software. LabSpec 6 software was applied for spectral result processing and baseline correction. The biomolecule enrichments were quantified by integrating individual Raman bands. The results were generated by Real Statistics Data Analysis Tools in the form of box plots, in which the lines in the boxes represent the medians of the biomolecule quantification distribution.

2.6 Statistical analysis.

All data are presented as $^{+}$/- standard error of the mean (SEM). For most data comparisons, an unpaired 2-tail student's t-test was used ($^{*}p<0.05$; $^{**}p<0.01$; $^{***}p<0.001$). For multiple comparison of three or more data sets, one-way analysis of variance (ANOVA) was used with post-hoc Tukey test ($^{*}p<0.05$; $^{**}p<0.01$; $^{***}p<0.001$). For statistical analysis of variation in gene expression and calpain activity during the adipocyte differentiation time-course, one-way ANOVA was used with a post-hoc Dunnett test comparing all timepoints to expression at time zero ($^{*}p<0.05$; $^{**}p<0.01$; $^{***}p<0.001$). Statistical analyses were conducted using GraphPad Prism 9.

Chapter 3: The role of TPC1/2 in the secretion of digestive enzymes by the pancreas

3.1 Background and the aim of study.

Previously, Pamela Lear, John Parrington, Ruben Nogueiras, Carlos Dieguez, and colleagues discovered that mature (aged 6-9 months) Tpcn1 knockout mice of both genders were resistant to age-related and HFD-induced obesity, and they found that this resistance was independent of caloric intake or expenditure and without apparent gastrointestinal side-effects (unpublished findings, personal communication by John Parrington). The researchers also found that in Tpcn1 knockout mice, the insulin, lipid, and glucose profiles were all improved over wild-type (WT) littermates. To be specific, in TPC1 KO mice, the level of HFD-induced insulin resistance (led by chronic overnutrition) was lower, and HFD-related lipid storage was milder, and the HFD-induced glucose enhancement was slight. This phenomenon suggests that endogenous TPC1 plays a key physiological role in the process of nutrient absorption in the gastrointestinal tract which includes pancreatic lipase activity and intestinal triglyceride (TG) absorption. Their conclusion was consistent with the previous discovery in our lab that Tpcn1 knockout mice were lighter because they possessed lower percentages of body fat and higher percentages of lean tissue.

I tried to find out the reason why Tpcn1 KO mice are leaner and healthier. In general terms, the process of fat metabolism in the animal body can be divided into three steps which are fat digestion, lipid absorption, and lipid metabolism. Lipase is the main enzyme participating in the process of fat digestion. There are three main types of lipase, distinguished by their sources, which are tongue lipase, gastric lipase and pancreatic lipase. During fat digestion, lipase secreted from the back of the tongue hydrolyzes fat in the mouth and this process continues in the stomach. Tongue lipase shows greatest activity against triacylglycerol composed of medium and short chain fat molecules, and milk fat is the ideal agent for this enzyme. Chyme stays in the stomach for 2-4 hours, and about 30% of triacylglycerol can be digested through the combined action of tongue lipase and gastric lipase. After entering the small intestine, lipids are emulsified by bile salt, which is a strong emulsifier, and dispersed into tiny clumps before they are digested by a mixture of enzymes.

Stimulated by lipids, the pancreas secretes inactive pro-lipase, pro-phospholipase A2, and pro-cholesterol lipase. Under normal conditions, these enzymes are activated in the small intestine and act on their respective substrates. Tongue lipase and gastric lipase can hydrolyze short-chain triglycerides, bile salts can emulsify long-chain triglycerides, and long-chain triglycerides are then hydrolyzed, which are then further digested by pancreatic lipase and absorbed by intestinal mucosal cells.

The reason why I embarked on the research in this area is that I wanted to further

explore the mechanism by which TPCs modulate the function of enzyme secretion and zymogen granule (ZG) exocytosis in pancreatic acinar cells. Dr. Pamela Lear previously showed that if Tpcn1 was knocked out, there appeared not to be enough lipase entering the small intestine to efficiently digest lipid (data not shown).

Before the exploration I had two aims for my research. First, I wanted to discover whether the reduction of lipase was because of impaired exocytosis (ZGs are trapped in pancreatic acinar cells) or whether it was because the lipase activity was weakened. Secondly, I wanted to find out whether the activation reduction/secretion reduction was specific to lipase.

3.2 Lipase activity is lower in Tpcn1 knockout pancreatic acinar cells.

I first tested whether not only the amount of lipase secreted is lower in Tpcn1 KO mice, but also the lipase activity. The results of my research show that in normal diet (ND) mice, pancreatic lipase activity declined in Tpcn1 knockout mice primary pancreatic acinar cells (PACs) after 12 weeks (Figure 10). However, on a high fat diet (HFD), pancreatic lipase activity declined in Tpcn1 knockout mice primary PACs at 6 weeks. Although the present evidence cannot identify the reason why there is a difference between normal diet or high fat diet mice, these results indicate that knocking out Tpcn1 inhibits lipase activation at a certain stage of the life span and suggests that Tpcn1 may

normally play a role in lipase secretion/activation.

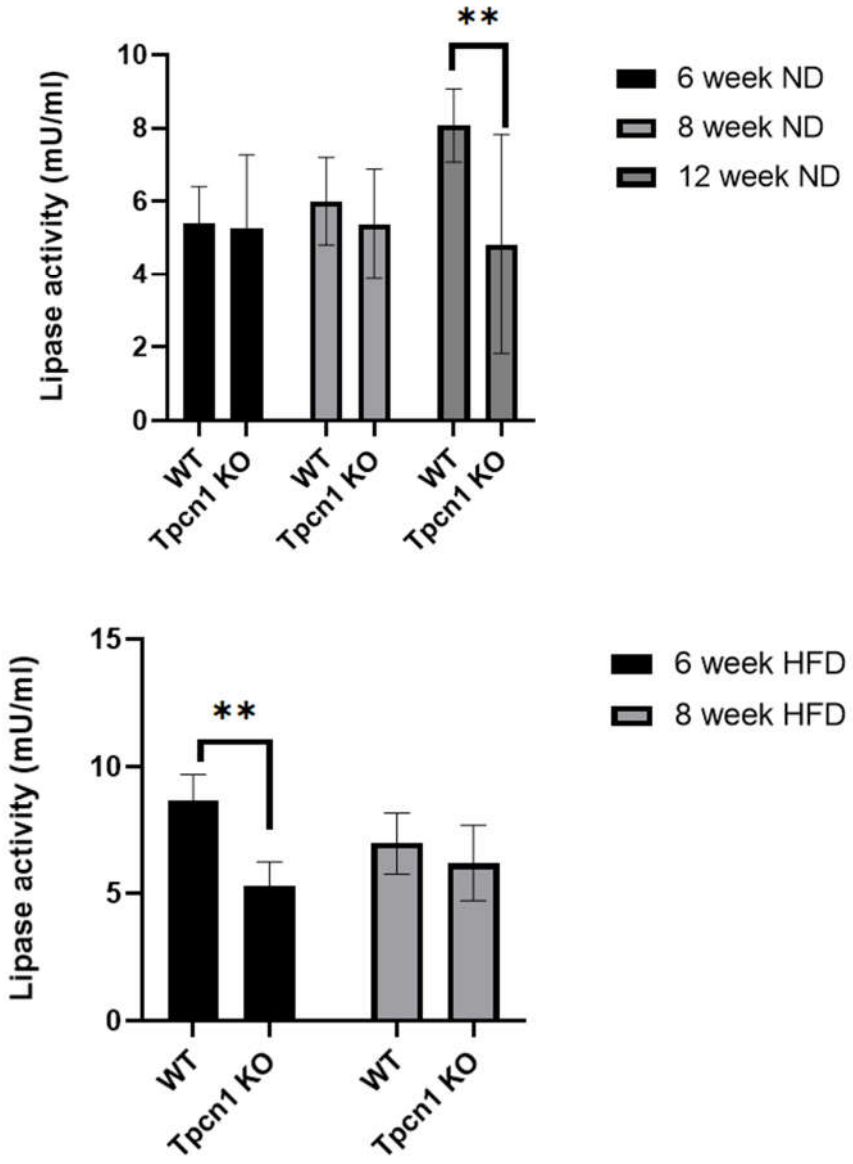


Figure 10. Activity of lipase in primary pancreatic acinar cells isolated from WT or Tpcn1 KO mice on a normal diet (ND) or a high fat diet (HFD) at an age of 6-12 weeks, measured by fluorometric assay using an Abcam kit ab118969. Significance was measured by student's t-test, n=3-5, ** $P < 0.01$.

The above results showed that lipase activity was reduced in Tpcn1 KO primary PACs. But two points are not clear.

First, it seems that in mice on a normal diet, the impairment of lipase activity occurs only in mature mice (aged 12 weeks/3 months), while in mice on a high-fat diet, the impairment of lipase activity occurs only in 6-week-old mice. This raises the question of whether this reduction of lipase activity was age-related and why this might be.

Second, in normal physical conditions, most digestive enzymes are not activated in pancreatic acinar cells, instead they are transferred through the pancreatic ducts to the small intestine and activated there. Only when pathological Ca^{2+} signalling occurs in pancreatic acinar cells, are the digestive enzymes activated in an untimely manner. The results showed that the activity of lipase was less after Tpcn1 KO, indicating that less lipase was untimely activated. Consequently, this may result in more activation occurring in the small intestine, which causes more abundant lipid digestion. My suspicion is that the secretion amount may vary greatly in Tpcn1 KO vs. WT pancreatic acinar cells. This is a reminder that isolated pancreatic acinar cells may not be a good model for either enzyme activation detection or secretion level quantification. Further studies could be carried out with pancreatic tissue freshly removed from the abdominal cavity.

3.3 Amylase and elastase activities are lower in Tpcn1 KO PACs.

My results described above showed that lipase activity is significantly less in Tpcn1 KO primary PACs. However, those results did not tell us whether this effect is specific to lipase or not. To look at this issue I measured the activity of other pancreatic enzymes, which are amylase and elastase (Figure 11). The results show that Tpcn1 KO is associated with reduced activity of amylase and elastase at 8 weeks but not at 6 weeks, and this suggest that Tpcn1 not only participates in lipase activation but also in other types of pancreatic enzyme activation, although the result of elastase activity is not representative here because of the low concentration in the samples.

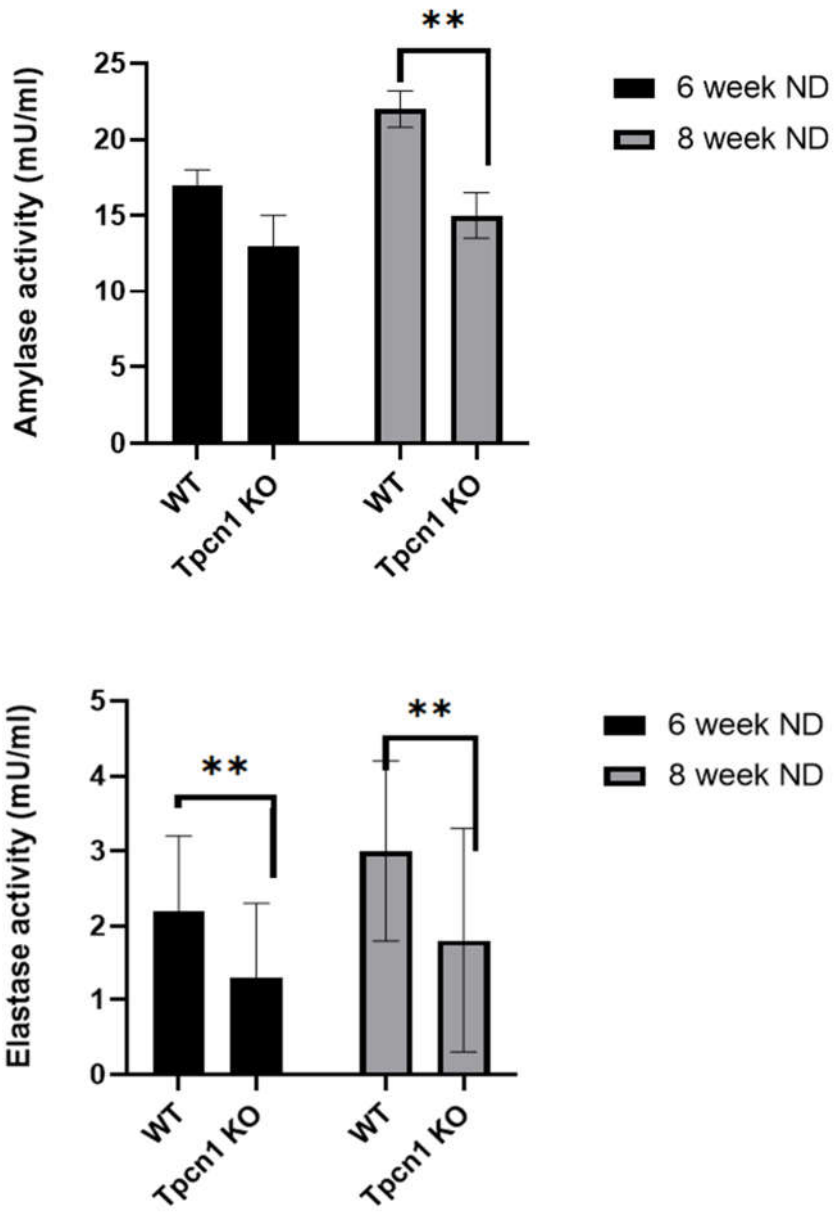


Figure 11. Activity of digestive enzymes secreted by pancreatic acinar cell other than lipase, taking amylase and elastase as examples. Activities of amylase and elastase are measured by a fluorometric assay as in previous studies.[180] Significance was measured by paired student's t-test, n=3, ** $P < 0.01$. Because of the discrepancies of experimental conditions, elastase activity was measured using substrates from different batches, which may be the main reason that

causes the large SEM. The significance of differences was measured between paired samples (which are processed using the same substrates) which still shows the trend that Tpcn1 KO PACs have reduced elastase activity than WT.

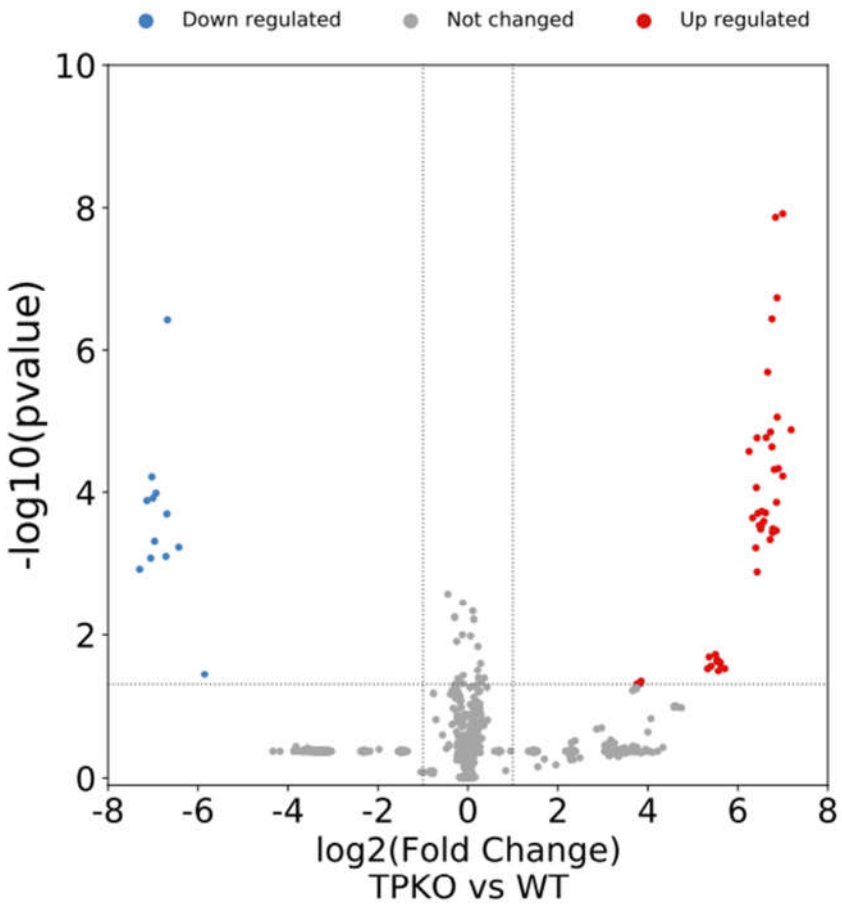
What is interesting is that similar to the results with lipase activity, the effects of Tpcn1 KO on amylase and elastase activity also seem age-related in that greater effects of Tpcn1 KO are evident in older animals. But it is regrettable that the age spans of the experimental animals are too small. Future studies could use some older animals such as 6-month and 9-month-old mice for pancreatic digestive enzyme activity tests.

The impaired activity of all these digestive enzymes in pancreatic acinar cells in Tpcn1 KO mice suggests that TPC1 may play an important role in regulating the untimely activation of digestive enzymes in acinar cells. Previous evidence from both clinical and experimental observations have shown that intrapancreatic activation of digestive enzymes is the inducement of pancreatitis onset. In this study I have shown that genetically inhibition of TPC1 can suppress the activation of these digestive enzymes within pancreatic acinar cells, suggesting that TPC1 could be developed as a potential drug target for pancreatitis. However, protease, which is the chief enzyme participating in the pancreatic autodigestion, was not shown to be inactivated by TPC1 KO. To verify my hypothesis, future studies should be carried out to investigate whether protease activity could be suppressed by gene-editing or pharmacological inhibition of TPC1.

3.4 Fatty acid β-oxidation is suppressed in Tpcn1 knockout pancreatic acinar cells.

In order to further study why Tpcn1 KO has such effects on the pancreas, I extracted the protein from pancreatic acinar cells isolated from WT and Tpcn1 KO mice, and then I sent the whole cell protein samples for LC-MS proteomic sequencing. The advantage of mass spectrometry for protein sequence analysis is that it is very sensitive. Peptides are split and proteins are identified with closed ends or modified ends. High-resolution mass spectrometry technology platforms claim that the protein sequence analysis can achieve 100% coverage of the target protein sequence measured. The proteomic analysis is usually used to detect whole cell protein expression and to compare the differences between two sample groups, while further bioinformatic analysis can tell us how a gene knockout such as that of Tpcn1 affects signalling pathways in pancreatic acinar cells.

To observe the differences in proteins in general according to the standardized expression mean value, the scatter plot of two groups/samples was drawn and according to the fold change and P value, and in addition a volcano plot of the two groups of samples was drawn (Figure 12). As shown in the plots, we can see that many proteins were significantly up or down regulated in Tpcn1 KO mice compared to WT controls (Figure 12).


Down regulated
Not changed
Up regulated
-log10(pvalue)
log2(Fold Change)
TPKO vs WT
10
8
6
4
2
0
-8
-6
-4
-2
0
2
4
6
8

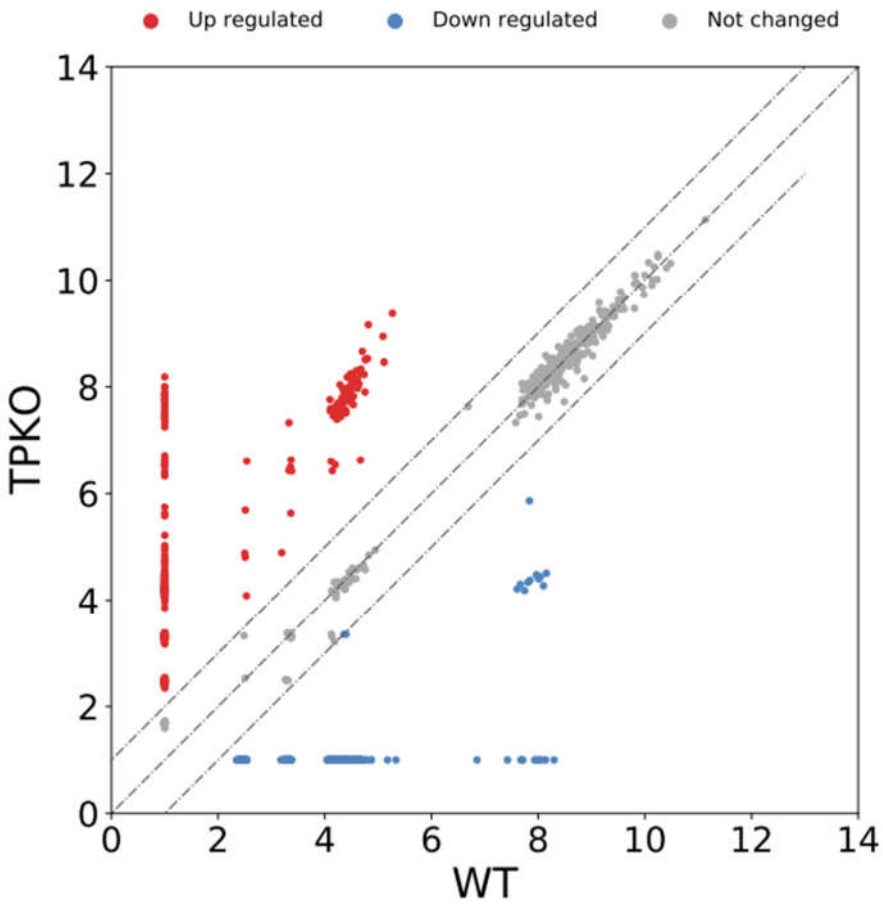


Figure 12. A). The volcano plot representing the differential protein expression. In the figure, the x-coordinate is log2 fold change value, and the y-coordinate is -log10padj or -log10pvalue. The red dots represent upward changes, the blue dots downward ones, and the gray dots no change. The dashed blue line represents the threshold line of differential gene screening criteria. Each data point represents a protein expression level. The y-axis represents the statistical significance (p value) of the protein expression with the amplitude of change. The more differentially expressed proteins are distributed at either end. B). The scatter plot representing the differential protein expression in Tpcn1 KO (TPKO) vs. WT.

Cluster analysis of differentially expressed proteins was performed using a pheatmap R package (v1.0.12) with standardized expression values. In the figure, red indicates relatively high expression, while blue indicates relatively low expression. The same group of samples were clustered in a branch (Figure 13, 14).

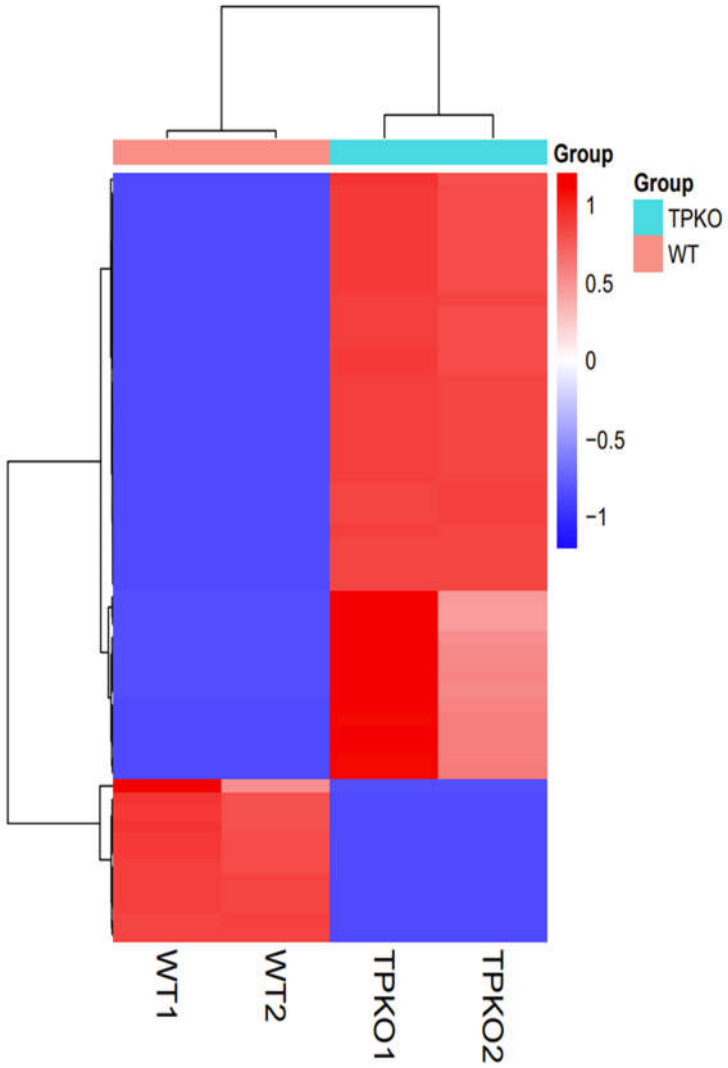


Figure 13. Heat map showing the differences in protein expression in four samples. The abscissa is the sample name, and the ordinate is the value after the normalization of differential

proteins. The redder the colour, the higher the expression level, and the bluer the colour, the lower the expression level. TPKO represents the TPC1 KO group while WT represents wild-type.

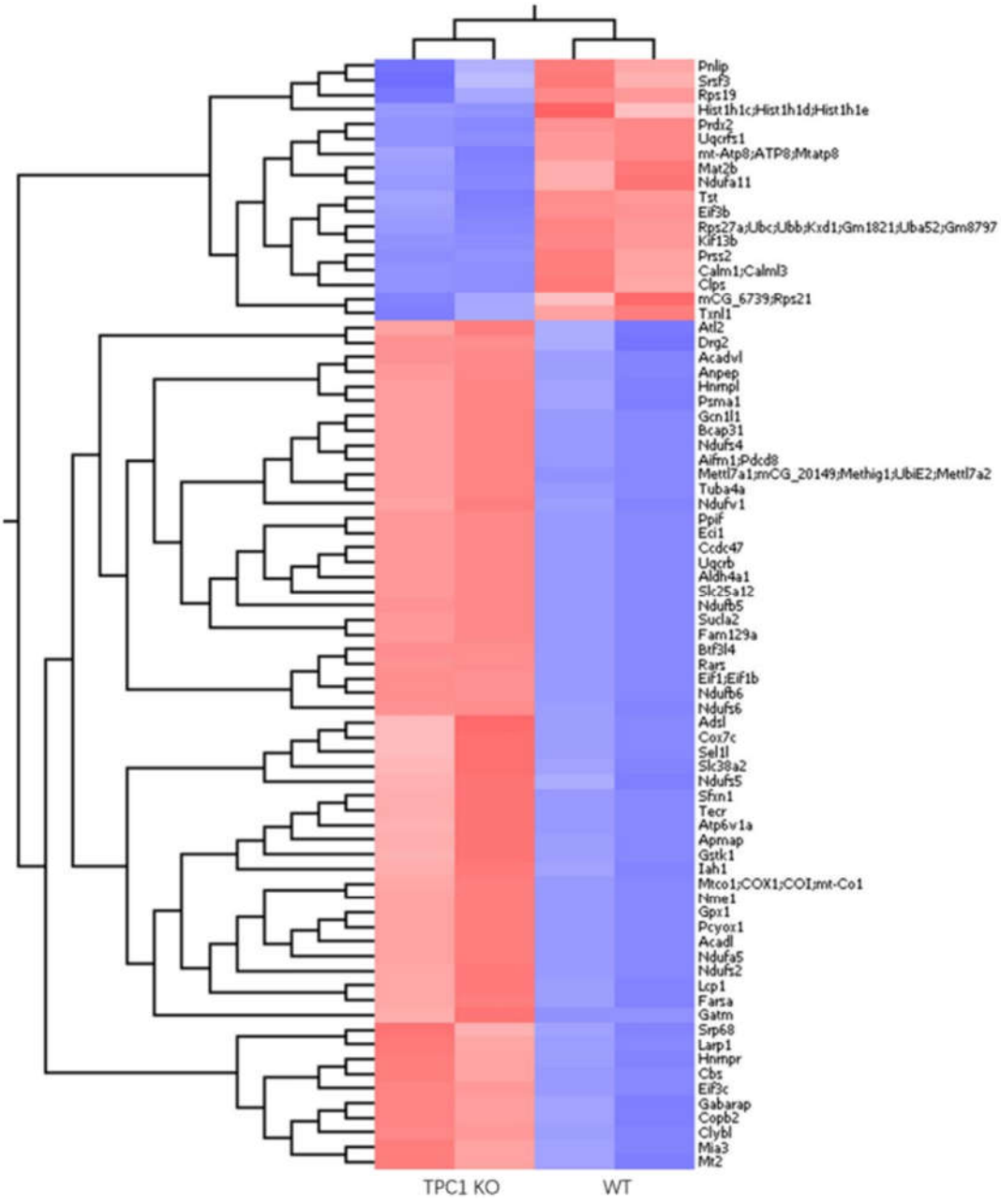


Figure 14. Heat map of shortlisted label free intensity of proteins in WT vs. TPC1 KO mice. The blue represents lower intensity, and the pink represents higher intensity (generated by Qlucore software).

KEGG Pathway maps were applied to explain the biological functions of biological

molecules at the pathway level (Figures 15, 16).[181] Pathway analysis of differentially expressed proteins makes it possible to infer which pathways these proteins participate in and their biological functions. With a P-value < 0.05 as the threshold value of the significantly enriched pathway, bar charts and bubble charts of the significantly enriched top ten KEGG pathways were drawn (Figures 15, 16).

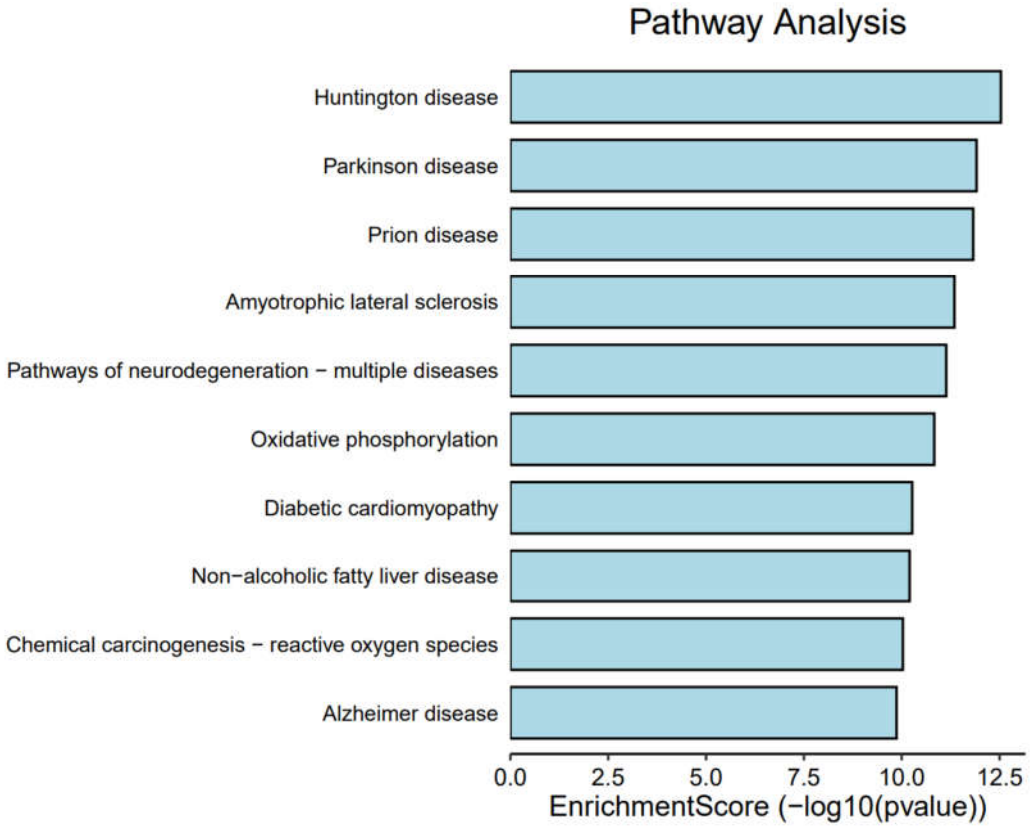


Figure 15. Enrichment bar chart of top ten KEGG pathways of proteins extracted from Tpcn1 KO vs. WT pancreatic acinar cells, with each bar representing one KEGG pathway clause, P＜ 0.05.

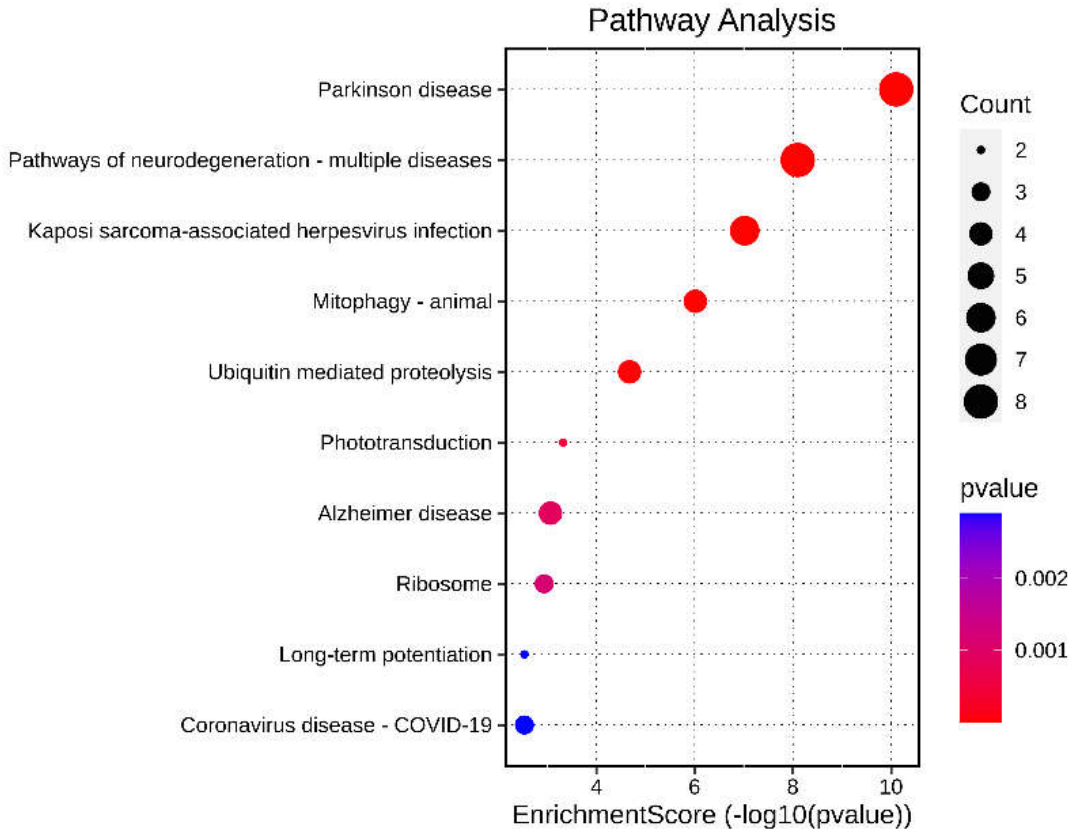


Figure 16. Enrichment bubble chart of top ten KEGG pathways of proteins extracted from Tpcn1 KO vs. WT pancreatic acinar cells, with each bubble representing one KEGG pathway clause, $P < 0.05$.

GO (Gene Ontology) is a comprehensive database to describe gene functions, which can be divided into three parts: biological process (BP), cellular component (CC), and molecular function (MF).[182] In the Figure, the x-coordinate represents the enrichment factor, which refers to the ratio of the number of differential genes annotated on GO Term to the total number of differential genes, and the y-coordinate is GO Term (Top 20). Each dot represents a comparison of Tpcn1 KO vs. WT, and the larger the dot is,

the more differential genes are enriched for this function. The green to red columns represents uncorrected P-values. A P value of < 0.05 was taken as the threshold for significant enrichment in GO terms, and the bubble chart was plotted (Figure 17).

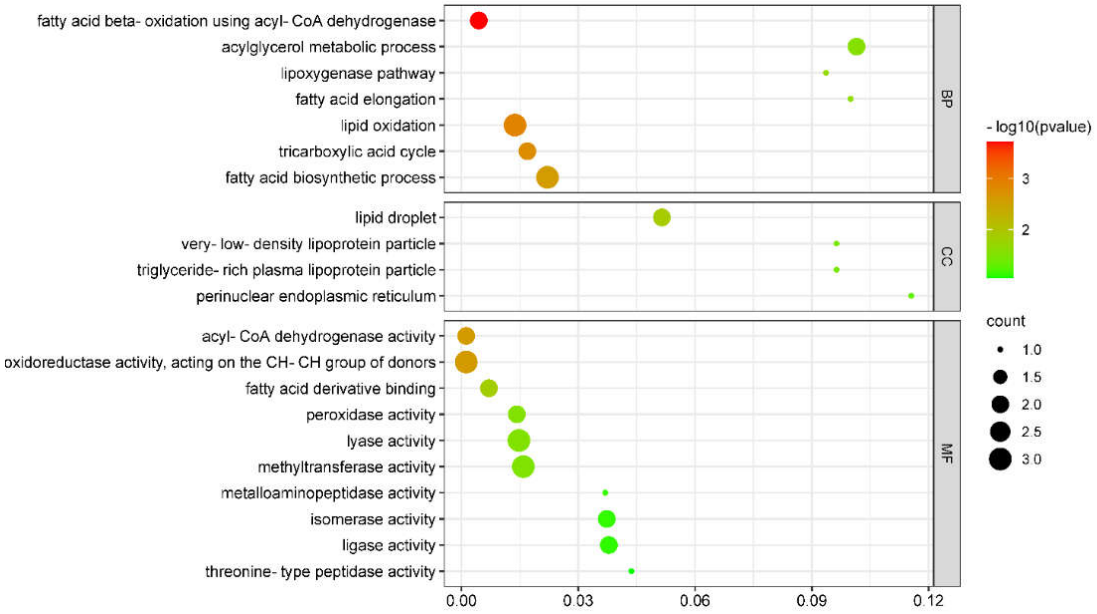


Figure 17. Enrichment bubble map of GO in proteins extracted from Tpcn1 KO vs. WT pancreatic acinar cells, with each bubble representing one GO term, P＜0.05. The horizontal coordinate is the Rich factor, and the higher the value, the greater the enrichment degree. Rich factor = number of differentially expressed genes located under this pathway term/number of all annotated genes located under this pathway term. The y-ordinate represents pathway terms with a top 20 high enrichment degree.

In the above results, it seems that Tpcn1 KO is closely related to neurodegenerative disease, particularly Huntington's disease and Parkinson's disease. This is consistent with some recent findings in this area. Thus there are studies showing that the

autophagic-lysosomal pathway takes charge of the clearance of damaged, dysfunctional or senescent proteins inside cells, and when lysosomal dysfunction occurs, autophagy is impaired which results in the accumulation of protein aggregates such as α-synuclein (in PD) which is regarded as an important source of pathogenesis in PD.[183,184]

For pathways and genes that are related to metabolism, fatty acid β-oxidation is shown to be down-regulated by Tpcn1 KO, which leads to suppressed acylglycerol metabolism. The oxidation modes of fatty acids include β-oxidation and special oxidation. Fatty acid β-oxidation means that glycerin and fatty acids produced by oil hydrolysis, are oxidized and decomposed into carbon dioxide and water, under the condition of sufficient oxygen supply, and this releases a large amount of energy for the body to use, and mostly happens in liver and muscle. The oxidation and energy generation are carried out in mitochondria, and a previous study suggested that knockout of TPC1 may impair the role of mitochondria in intracellular Ca^{2+} signalling. In addition, a down regulation was observed of the activity of acyl-CoA dehydrogenase which take part in β-oxidation, which can synergistically explain why TPC1 KO impairs the process of fatty acid β-oxidation.[185]

Importantly, the results above also suggest that, apart from the acyl-CoA dehydrogenase down-regulating fatty acid β-oxidation, the activity of multiple enzymes are also reduced in Tpcn1 KO pancreatic acinar cells; these include some enzymes involved in fatty acid oxidation and other enzymes such as peroxidase, lyase, methyltransferase,

isomerase, and metalloaminopeptidase. Some of these enzymes do not play a role in digestion. Some previous studies showed that the activity of isomerase may be closely related to mitochondrial Ca^{2+} overload, because the dysfunction of isomerase impairs the generation of a mitochondrial permeability transition pore.[186] However, there is not much information about the upstream regulation of these enzymes in pancreatic acinar cells.

3.6 Cytochrome C expression was suppressed in Tpcn1/2 DKO but not in TPC1 KO and WT pancreatic acinar cells.

Raman micro-spectroscopy is an anode vibrational spectroscopy based on inelastic scattering of light, which can be used to detect the intrinsic molecular profiles of cells. Researchers have developed Raman micro-spectroscopy into a label-free technique for studying the phenotypes of single cells. The biggest advantage of Raman is non-destructive detection; thus, individual cells are still intact and viable for subsequent use after Raman. Raman spectroscopy analysis uses principal component analysis. Some previous reports have demonstrated the utility of Raman analysis for phenotypic discrimination in animal cells.

Several changes in Raman bands for major cellular components and metabolites were observed in WT compared to TPC1 KO pancreatic acinar cells (Figures 19, 20).

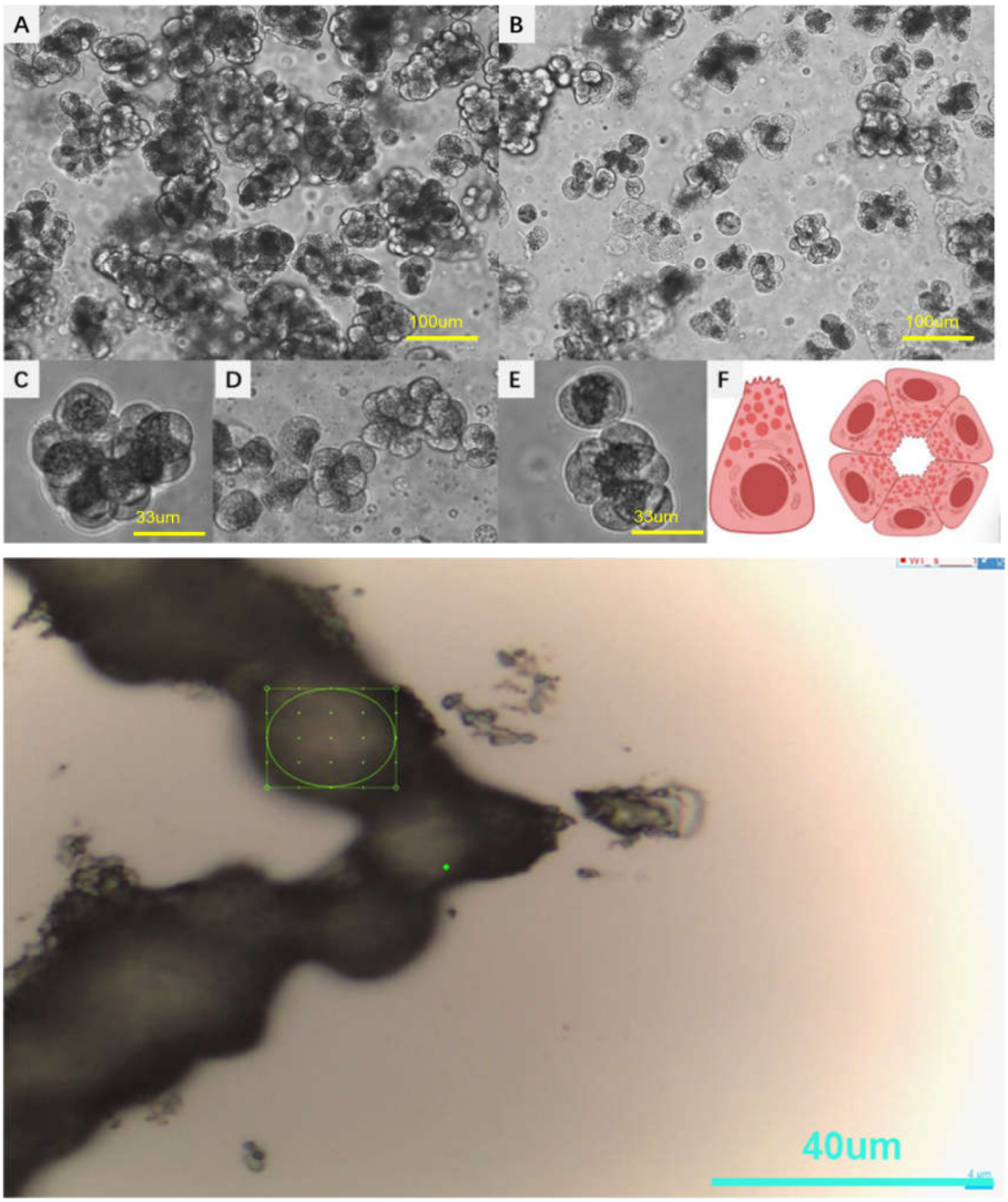


Figure 18. A) Pancreatic acinar cells after isolation. B) Pancreatic acinar cells one hour after isolation. C) E) Healthy acinar cell clusters (acini). D) Single cells with clusters. F) Schematic diagrams of single acinar cells and acini. G) The fixed acinar cells used for Raman spectroscopy with the location of single-cell component analysis (green square).

Similar to the proteomic sequencing results, prominent differences were found between the single-cell Raman spectra (SCRS) of Tpcn1 KO and WT pancreatic acinar cells, including Raman bands at 746 cm^{-1}, and 1,125 cm^{-1} (cytochrome c), 1,295 and 1,440 cm^{-1} (unsaturated lipid).

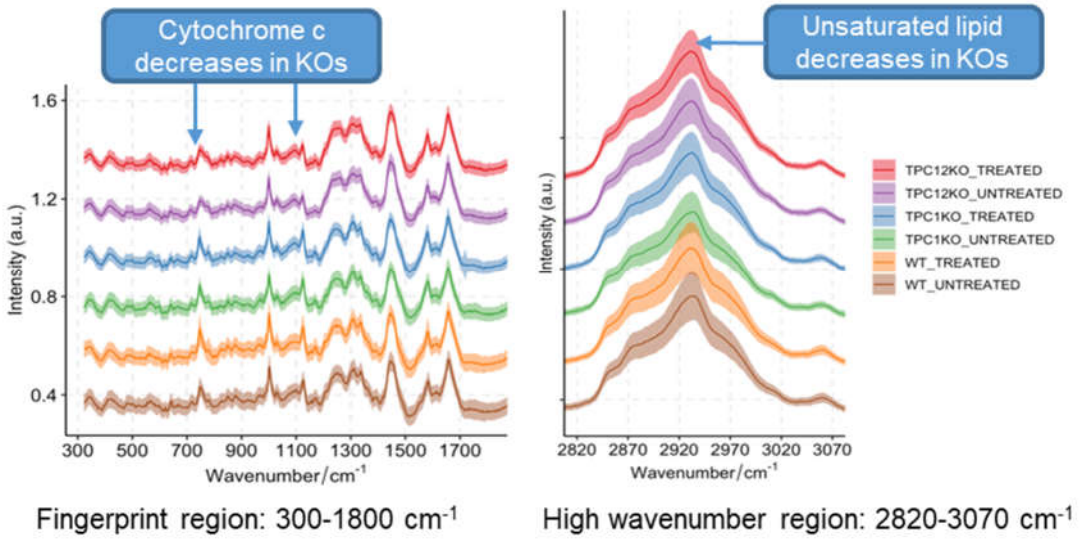


Figure 19. Averaged single-cell Raman spectra (SCRS) of the TPC KO and WT pancreatic acinar cells, differing primarily at 749, 1128, and 1312 cm^{-1}, which can be assigned to cytochrome c, and also differing at 2920 cm^{-1} which can be assigned to unsaturated lipid.

In order to confirm the variations of biomolecules in the presence or absence of TPC1 expression, I further performed semi quantification of cytochrome c by integrating relevant Raman band areas. The bands at 750 cm^{-1} and 1,127 cm^{-1} showed a decreased cytochrome c expression in Tpcn1/2 DKO pancreatic acinar cells (Figure 16).

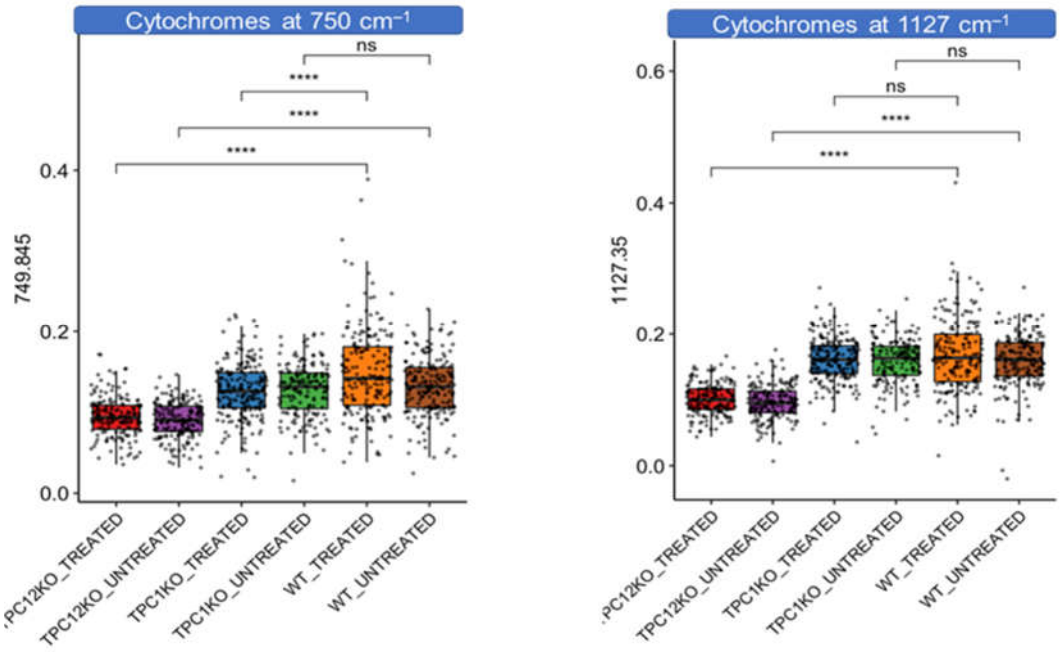


Figure 20. Identification of potential biomarkers using SCRS. Average Raman spectra acquired from the Tpcn1/2 DKO (red/purple), Tpcn1 KO (blue/green) and WT pancreatic acinar cells annotated with Raman bands identified in cytochrome C (750 and 1,127 cm−1) (n=1,192). The results represent means ±SEM. Significance was measured by ANOVA, post hoc Tukey's test, **** P≤0.0001.

In order to validate the results of Raman spectroscopy single-cell analysis, immunoblotting was used to detect the expression level of cytochrome c in whole protein extracted from primary pancreatic acinar cells. The results show that cytochrome c expression was indeed suppressed in TPC1/2 DKO pancreatic acinar cells (Figure 21).

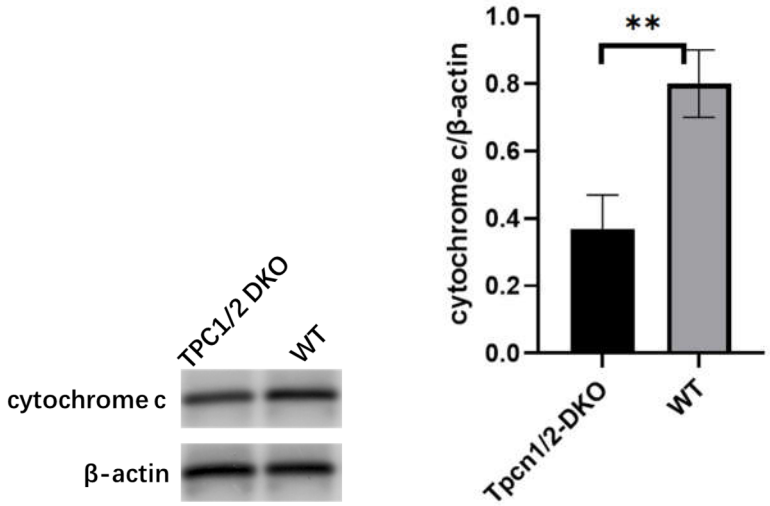


Figure 21. A) The relative protein expression levels of cytochrome c (15 kDa) were measured by western blot in primary pancreatic acinar cell whole protein extraction (n = 3). The expression level of β-actin (42 kDa) was measured as an internal reference. B) Grey value ratio of cytochrome c/β-actin analysed by Fiji Image J software. Significance was measured by student's t-test, n=1, ** $P < 0.01$.

The results above show that cytochrome C expression has been suppressed in TPC1/2 DKO but not in TPC1 KO and WT PACs. This is the first study showing that endogenous cytochrome C expression is related to intercellular Ca^{2+} signalling, particularly to TPCs.

Cytochrome C is a water-soluble protein with a molecular weight of 12-13 kDa. It is located outside the inner membrane of mitochondria, between the respiratory chain complex III to complex IV, and plays an important role in the regulation of mitochondrial energy metabolism. Cytochrome C was described as an 'extreme

multifunctional' protein. Exogenous cytochrome C is used for auxiliary treatment of various tissue hypoxia, for instance caused by carbon monoxide poisoning, sedative-hypnotic poisoning, cyanide poisoning, neonatal asphyxia, hypoxia in severe shock period, cerebrovascular accident, concussion sequelae, anaesthesia and breathing difficulties caused by lung diseases, and myocardial hypoxia caused by various heart diseases.[187] In recent years, the role of cytochrome C in cell apoptosis has attracted wide attention, notably following a study showing that nuclear apoptosis (DNA fragmentation) depends on the existence of a certain organelle fragment, which was subsequently confirmed to be composed of mitochondrial cytochrome C.

In the previous section I discussed how mitochondrial function was impaired by Tpcn1 KO through dysfunction of the isomerases causing overload of Ca^{2+} in mitochondria, which further results in the inhibition of β-oxidation of fatty acids in mitochondria. Since endogenous cytochrome C is generally regarded as a mitochondrial electron transporter, I believe that the low expression of cytochrome C may be related to mitochondrial dysfunction caused by Tpcn1 KO.[188] And to pursue this further, it would be very interesting to investigate whether the generation and cytosolic release of cytochrome C from mitochondria has any relationship to NAADP triggered Ca^{2+} release from acidic stores. It will also be interesting to see whether TPCs have any function in cell apoptosis through regulating the synthesis and release of cytochrome C. This is a very preliminary hypothesis, as the study of cytochrome C is still at an early

stage, but I believe that the functional effects of TPC mediated Ca^{2+} signalling in mitochondria is a promising direction for further exploration in this field.

3.7 LSM12 expression was suppressed in Tpcn1/2 DKO PAC and localized on the periphery of pancreatic acini.

In addition, another part of my exploration in pancreatic acinar cells was Lsm12 expression level detection. Since a recent study confirmed that Lsm12 is a mediator of the association of NAADP and TPCs,[189] here I tried to see whether Lsm12 expression in pancreatic acinar cells is altered by TPC KO (Figure 22). The results show that Lsm12 expression is significantly depressed in TPC1/2 DKO pancreatic acinar cells, but it is not significantly different in the single TPC1 or TPC2 KO cells (Figure 22).

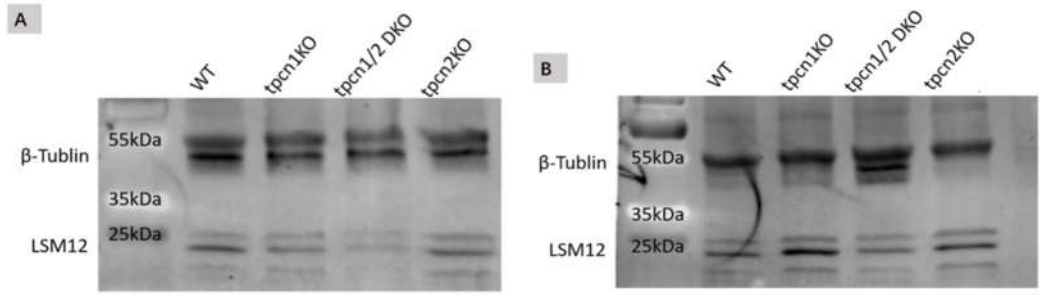


Figure 22. Western blot protein analysis of Lsm12 (23 kDa) in primary pancreatic acinar cell whole protein extracted from WT, Tpcn1 KO, Tpcn1/2 DKO, or Tpcn2 KO mice. The blotting process was duplicated. The expression level of β-tublin (55 kDa) was measured as an internal reference.

I also used immunostaining to study the location of Lsm12 in freshly isolated pancreatic acinar cells and hepatocytes (Figure 23). The results shows that Lsm12 appears to be more intensively localized at the basolateral pole of acinar cells, and on the periphery rather than in the middle of acini, but it is evenly distributed in hepatocytes (Figures 23, 24).

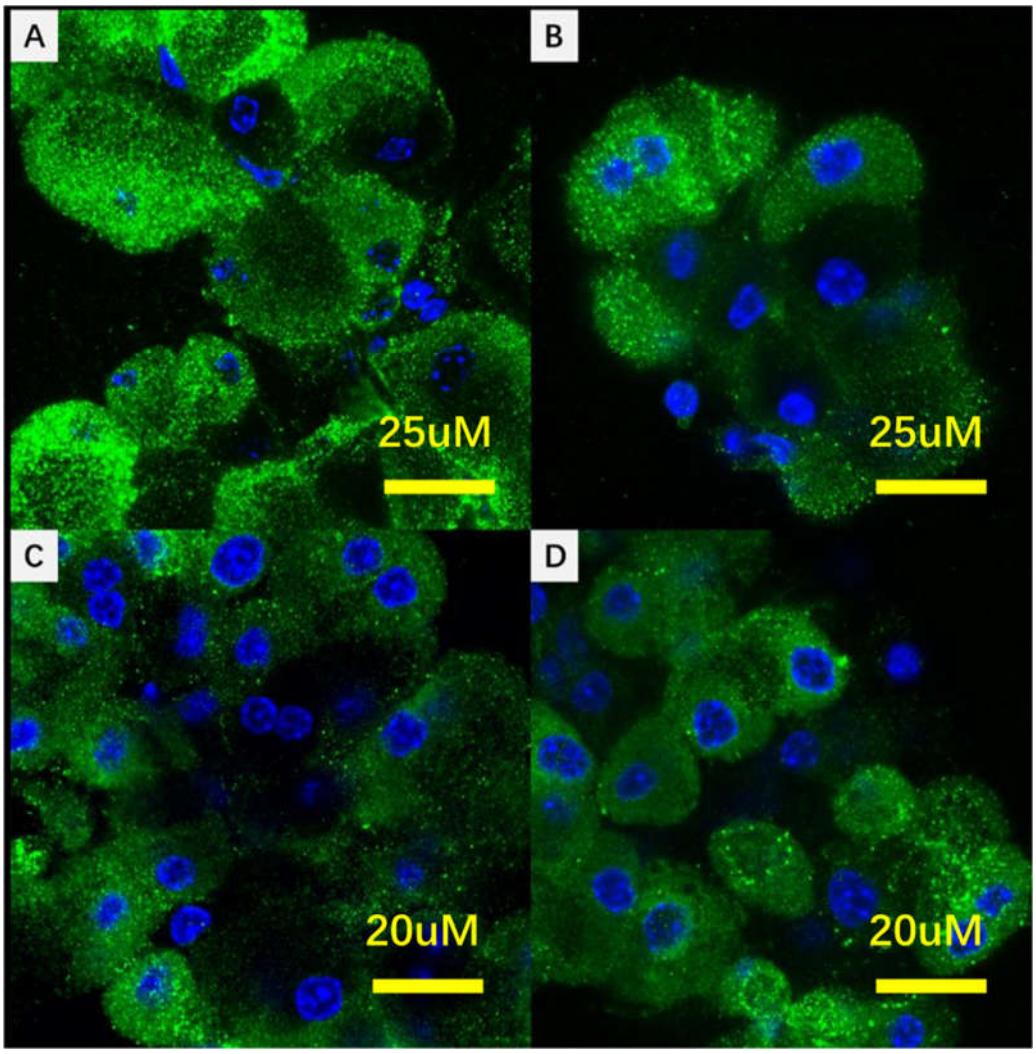


Figure 23. A) Lsm12 in primary WT mouse pancreatic acinar cells. B) Lsm12 in primary Tpcn1 KO mouse pancreatic acinar cells. C) Lsm12 in primary Tpcn1/2 DKO mouse pancreatic acinar cells. D) Lsm12 in primary Tpcn2 KO mouse pancreatic acinar cells.

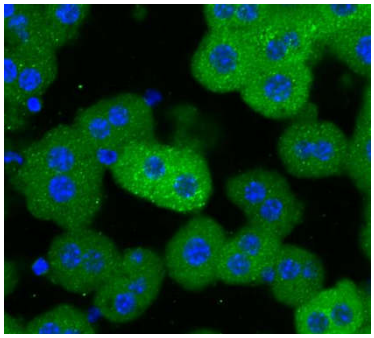


Figure 24. Lsm12 in primary WT mouse hepatocytes.

Lsm12, an RNA-binding protein involved in RNA metabolism, aroused researchers' interests in recent years since it was shown to connect NAADP and TPCs during the activation of TPCs.[189,190] The results above show that Tpcn1/2 DKO pancreatic acinar cells have significantly suppressed expression of Lsm12. However, there is not much research into the sources and functions of Lsm12, and future studies need to be performed to find out why its expression level is changed.

In addition, Lsm12 tends to localize on the periphery of the acini. Unfortunately, the hepatocytes of Tpcn1/2 KO animals were not isolated and immunoassayed, so that we are unable to know whether TPC1/2 DKO has any effects on Lsm12 location in hepatocytes.

3.8 Conclusion.

My exploration of pancreatic acinar cells from TPC KO vs. WT mice went in three directions. First, to further improve our previous study, the activity of lipase and other

pancreatic digestive enzymes were analysed separately. In this research direction I found that the pancreatic enzyme activity of Tpcn1 KO mice was lower than that of WT mice, indicating that TPC1, or Ca^{2+} release from endolysosomal systems through TPC1, regulates the activation of lipase in pancreatic acinar cells. And, this effect seems to be age-related since older mice have a higher extent of TPC1-related lipase activation. The question remaining to be answered is why the animals seemed healthy even when they lacked several digestive enzymes. And another point which is interesting is whether the TPC1-related impaired activation of the enzymes rescues animals from pancreatitis. Future studies in this area may use pancreas tissues or collected pancreatic juice instead of isolated acinar cells for enzyme activity detection.

Second, to explore which signalling pathways might be involved in the effects of TPC1 in pancreatic acinar cells, proteomic analysis was conducted with Tpcn1 KO vs. WT pancreatic acinar cells. In this part of the study, the expression of several enzymes, including acyl-CoA dehydrogenase which take part in β-oxidation, was shown to be impaired by Tpcn1 KO. Several physiological processes were predicted to be influenced by Tpcn1 KO, and the analysis has shown that these physiological processes are mainly related to neurodegenerative disease, in particular involving mitochondrial dysfunction. The question is how TPC1 is involved in the whole process, and whether it is through mitochondrial Ca^{2+} overload or not. Further evidence needs to be presented and future studies may take these findings as a starting point.

Third, the results of Raman spectra and immunoblot analysis have shown that Tpcn1/2 DKO significantly impairs cytochrome C expression. This is the first study to reveal that TPCs, and probably more generally Ca^{2+} release from endolysosomal systems, have something to do with cytochrome C expression. There is lots to be discussed and explored relating to this finding. Further work may be carried out with other cell types such as cell lines with Tpcn1/2 DKO to see if this is a mechanism that regulates cell apoptosis.

Finally, the Lsm12 immunoblots and immunostaining showed a very interesting phenomenon, namely that Lsm12 expression level was significantly reduced in Tpcn1/2 DKO pancreatic acinar cells. The reason remains unclear and few studies have focused on this direction. But it will be worth investigating the upstream mechanism of Lsm12 expression to study how TPC1/2 DKO has an impact on it.

To sum up, isolated pancreatic acinar cells are a good model for the exploration of the functions of TPCs. Although the studies are preliminary, it can be a good start for future exploration in this field.

Chapter 4: The role of TPC2 in adipocyte differentiation

4.1 *Tpcn2* KO mice of both sexes have abnormal adipogenesis compared to wild type controls.

Previous researchers in our lab had determined that there were differences in fat and lean content of Tpcn2 KO mice using time domain nuclear magnetic resonance (TD-NMR) (the experiments were performed by Dr. Ruth Tunn, unpublished findings, personal communication by John Parrington) (Figure 25).

Male Tpcn2 KO mice were found to be significantly lighter than wild-type (WT) controls at all ages studied, mainly due to lower fat mass. Lean mass was not significantly different in Tpcn2 KO males, except in the 9-month-old cohort, in which significantly reduced lean mass was observed for Tpcn2 KO males (Figure 25).

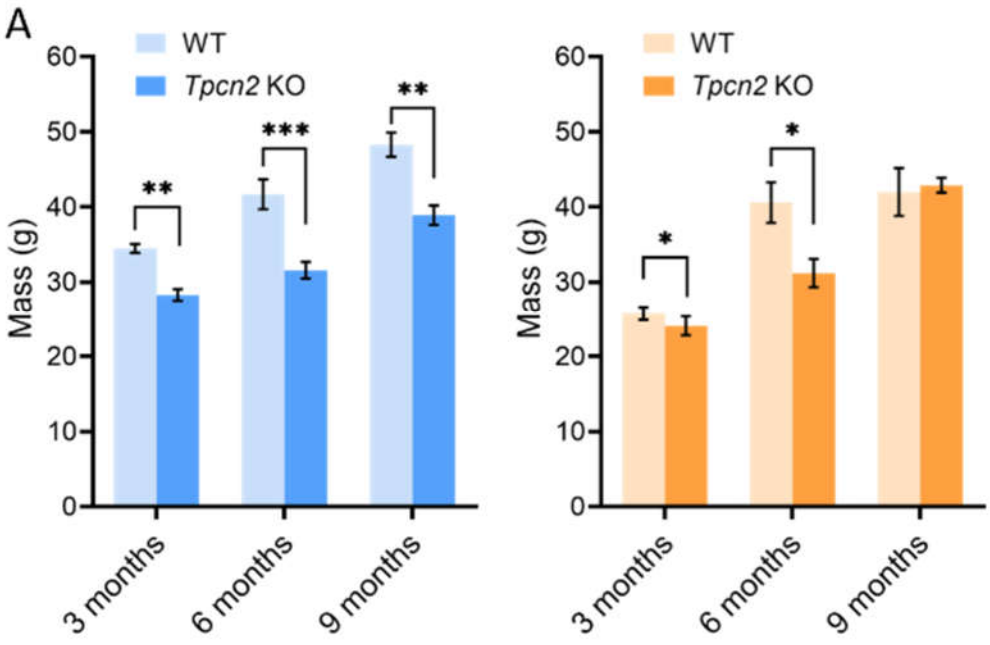


Figure 25. Total body mass of male (blue) and female (orange) Tpcn2 knock-out vs. WT mice. (Significance was measured by student's t-test, n=7-8. *p<0.05; **p<0.01; ***p<0.001)

This translated into an overall reduced body fat percentage with concomitant increase in percentage of lean composition. Tpcn2 KO females were also significantly lighter than WT controls, up to 6 months, and similar to the male group this was due to reduced fat mass.

The reduced fat mass and normal lean mass seen in 3- and 6-month-old females resulted in a decreased body fat percentage and increased percentage in lean composition. In contrast, the 9-month Tpcn2 KO female group showed no significant differences in any of the parameters measured, when compared to the WT controls (Figure 26).

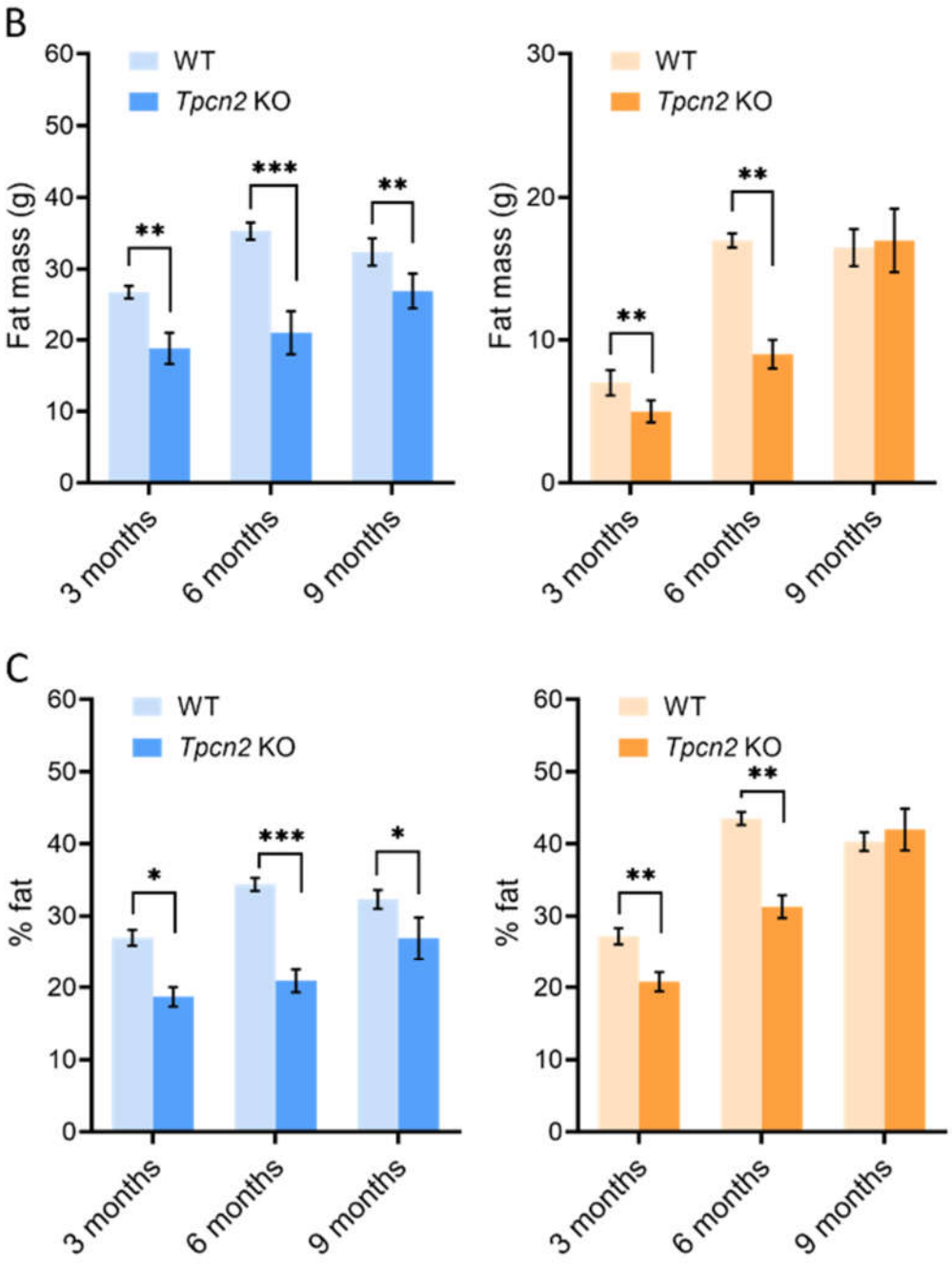


Figure 26. B) Total fat mass of male (blue) and female (orange) Tpcn2 KO vs. WT mice. C) Percentage of body fat of male (blue) and female (orange) Tpcn2 KO vs. WT mice. (Significance was measured by student's t-test, n=7-8. *p<0.05; **p<0.01; ***p<0.001)

To further investigate the physiological condition of Tpcn2 KO mice, an intraperitoneal glucose tolerance test (IPGTT) was carried out (Figure 27). In response to a glucose challenge, Tpcn2 KO mice showed a slight, non-significant tendency towards blood glucose peaking higher than in WTs, with no significant difference in total glycaemia (Figure 27).

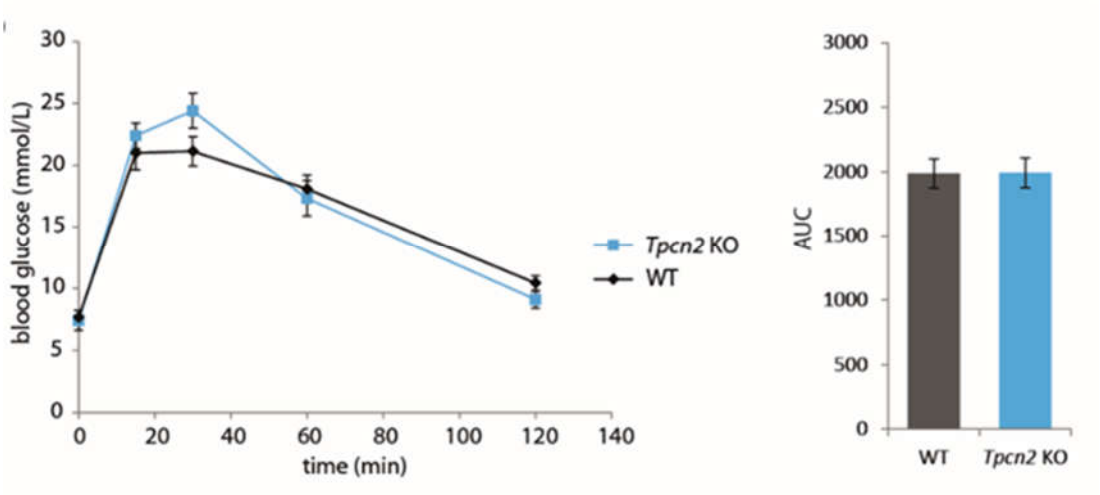
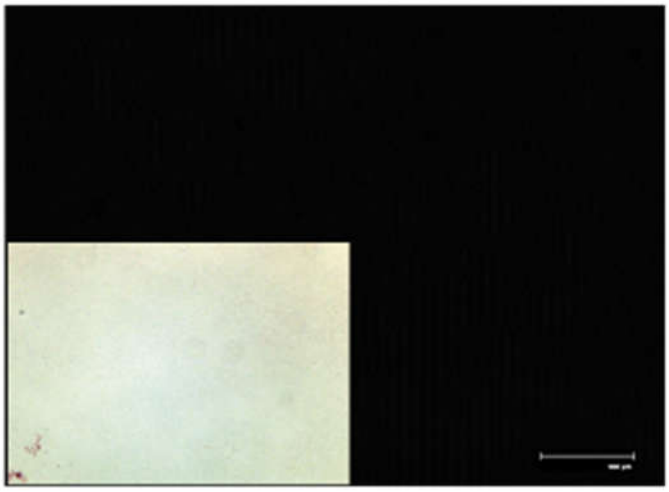


Figure 27. Intraperitoneal glucose tolerance test (IPGTT). Response to 2g/kg IP glucose following overnight fast in male Tpcn2 KO and strain-matched WT mice aged 9-11 weeks. (Significance was measured by student's t-test, Tpcn2 KO n=11, WT n=8, AUC = area under the curve)

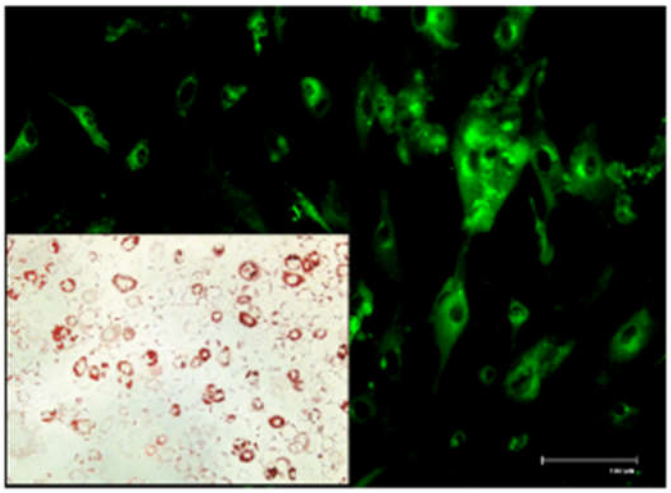
4.2 TPC2 mRNA expression is transiently up regulated during *in vitro* adipocyte differentiation.

Differences in adiposity in Tpcn2 KO mice *in vivo* might have a number of different underlying causes. In this study we decided to use *in vitro* analysis to focus on whether TPC2 might be involved in one specific process linked to the related phenomena of adiposity and adipogenesis, namely adipocyte differentiation. To see whether TPC2 might play a role in adipocyte differentiation *in vitro*, we used the C3H10T1/2 cell line, a mesenchymal stem cell line that can differentiate along adipogenic, myogenic, osteogenic, or chondrogenic pathways.[191] In the presence of a cocktail of insulin, dexamethasone, and IBMX in serum-containing medium, C3H10T1/2 cells differentiate into adipocytes.

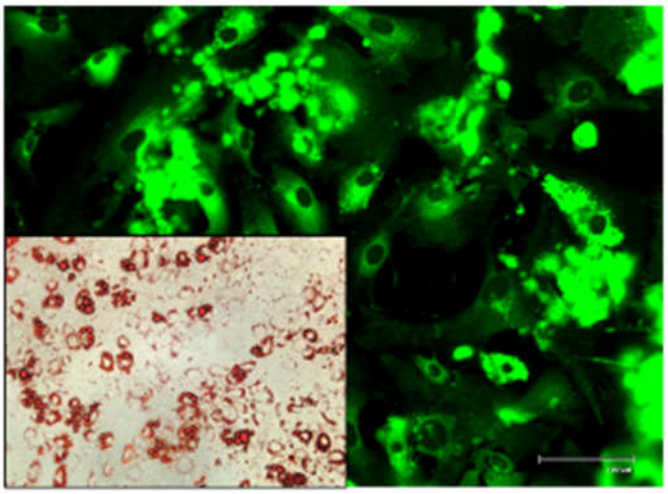
Progression of adipogenesis was monitored by Oil Red O staining or AdipoRed fluorescence, which both measure accumulation of lipid droplets, and RT-qPCR analysis of mRNA expression of adipogenic markers, to ensure that the morphological changes observed in cells subjected to the standard differentiation protocol were indicative of true adipogenesis (Figures 28, 29). Early transient upregulation of c/Ebpδ mRNA expression, followed by sustained Pparγ2 and Srebp1 mRNA expression and later aP2 mRNA expression, which is the expected sequential pattern of expression of these genes during adipocyte differentiation, confirmed adipogenesis at the molecular as well as the morphological level (Figure 29).[192]



Day 0



Day 4



Day 8

Figure 28. AdipoRed and Oil Red O staining of differentiating C3H10T1/2 cells, immediately before start of differentiation induction with adipogenic medium, and 4 and 8 days after the start of treatment. Accumulation of the stain indicates lipid droplet formation. (Scale bar=100 μm)

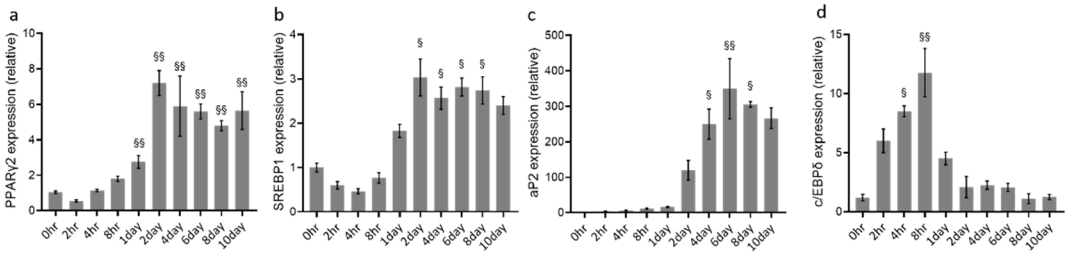


Figure 29. mRNA levels of adipogenic marker genes in differentiating C3H10T1/2 cells. a) Pparγ2; b) Srebp1; c) aP2; d) c/Ebpδ. Values are normalised to the geometric mean of 18S and ubiquitin c mRNA expression and presented as fold-change relative to the 0h value. n=2 (c/Ebpδ); n=3 (Pparγ2, aP2, Srebp1). (Significance was measured by ANOVA, post-hoc Dunnett test vs 0h, n=7-8. §p<0.05; §§p<0.01.)

We next studied whether TPC2 expression levels change during the differentiation process, as this might indicate an involvement in this process. RT-qPCR was used to evaluate expression levels of Tpcn2 mRNA at different time intervals in C3H10T1/2 cells subjected to the standard differentiation protocol. Tpcn2 mRNA levels increased significantly early during adipocyte differentiation, and in a transient manner, with mRNA levels peaking at around 4 hours post-induction and returning to starting levels by around 48 hours after the start of induction (Figure 30).

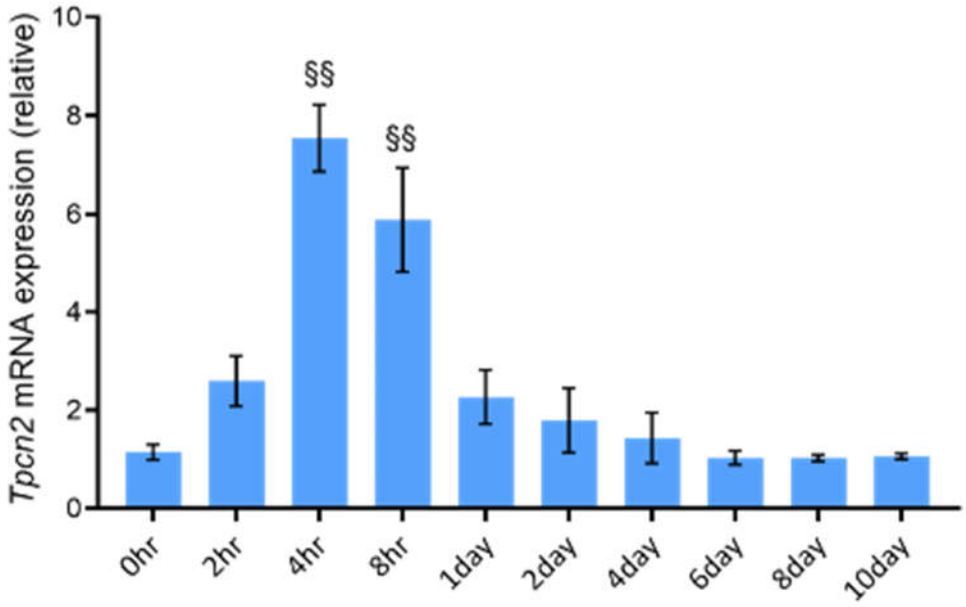


Figure 30. Tpcn2 mRNA levels in differentiating C3H10T1/2 cells. Values are normalised to the geometric mean of 18S and ubiquitin c mRNA expression and presented as fold-change relative to 0hr value. (Significance was measured by ANOVA, post-hoc Dunnett test vs 0h, n=3, §§$p<0.01$)

4.3 TPC2 mRNA expression during adipocyte differentiation is up regulated by a cAMP signal.

In order to investigate which components of the adipocyte differentiation cocktail were responsible for the observed changes in Tpcn2 mRNA expression, mesenchymal stem cell line C3H10T1/2 cells were treated with the individual components separately, and harvested at 4 hours post-induction, a stage at which a significant change in expression was previously seen (Figure 31).

Tpcn2 mRNA levels were significantly increased by IBMX, to a level comparable to that achieved by complete differentiation medium, whilst the other components of the cocktail had no significant effect on Tpcn2 mRNA expression (Figure 31).

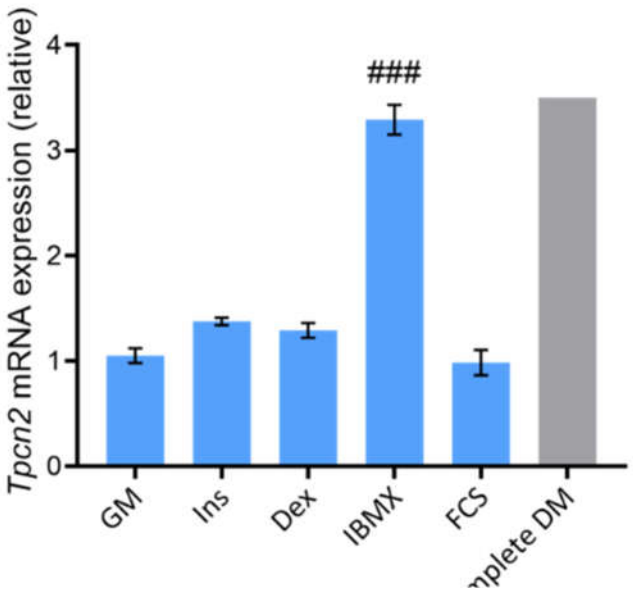


Figure 31. Determination of the components of the adipocyte differentiation medium that stimulates Tpcn2 mRNA expression. Grey bar: sample at 4 hours (n=1). Significance was measured by ANOVA, post-hoc Tukey test, n=3. ###$p<0.001$. Values are normalized to the geometric mean of 18S and ubiquitin c mRNA expression and presented as fold change relative to GM condition.

Moreover, treatment with medium lacking IBMX but containing all other components of the differentiation cocktail, failed to induce Tpcn2 mRNA expression. This finding suggested a potential involvement of cAMP signalling in the induction of Tpcn2 mRNA

expression, since IBMX inhibits cAMP phosphodiesterase (PDE), and thus acts to increase cAMP levels (Figure 32). [193]

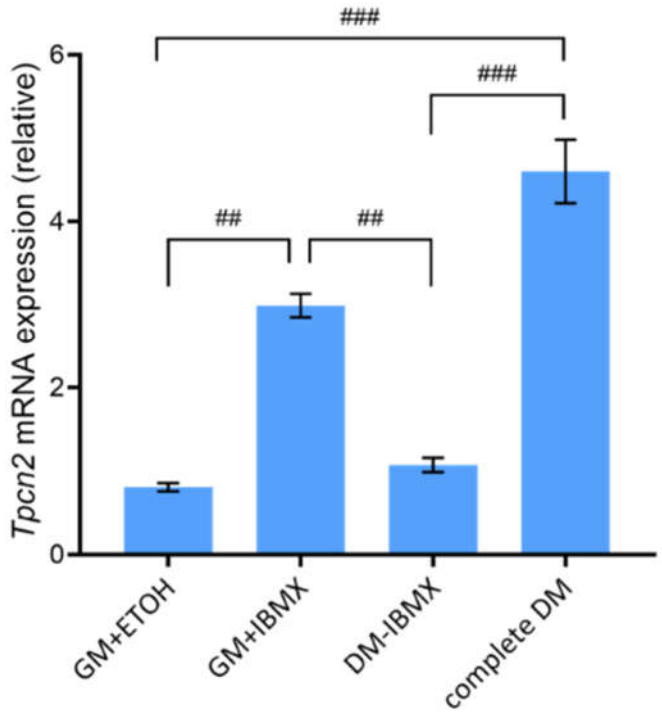


Figure 32. Effect of IBMX on Tpcn2 mRNA expression in 2-day post-confluent C3H10T1/2 cells. Significance was measured by ANOVA, post-hoc Tukey test, n=3-4, ##p<0.01, ###p<0.001. Values are normalized to the geometric mean of 18S and ubiquitin c mRNA expression and presented as fold-change relative to GM condition.

IBMX is a non-specific inhibitor of cAMP and cGMP phosphodiesterase. It inhibits degradation of cAMP, allowing for a cAMP level enhancement, thus PKA is activated by increased cAMP, which results in increased differentiation of stem cells.[194]

IBMX is used as a cAMP-elevating agent in adipogenesis system.[194] At the early stage of adipocyte differentiation, multiple transcription factors (green in the Figure) are activated directly by the hormone cocktail consisting of glucocorticoids, insulin, a cAMP-elevating agent, and fetal bovine serum (Figure 33).

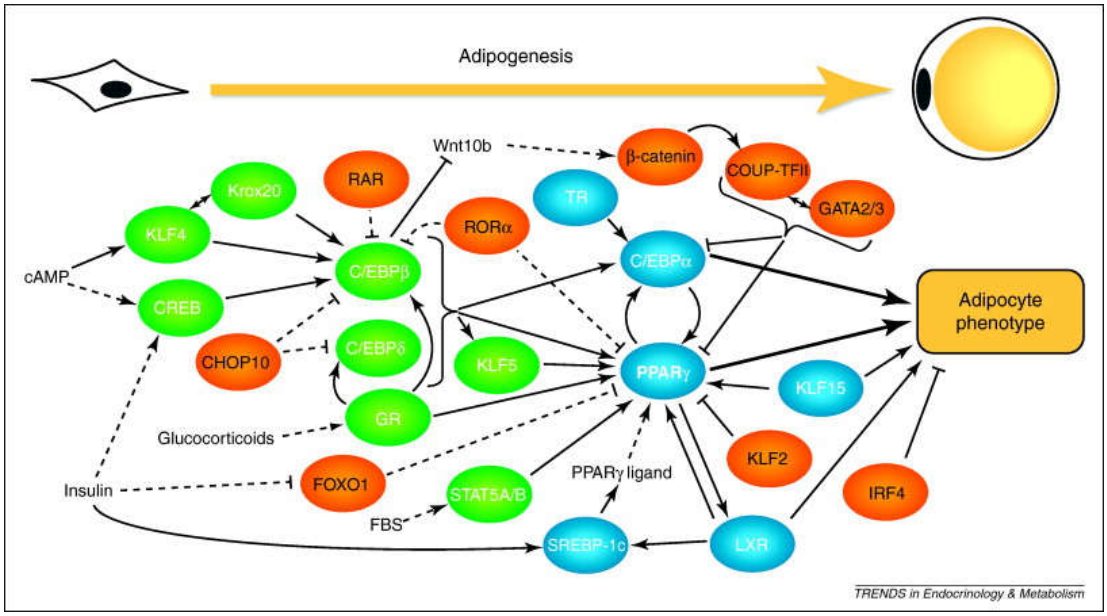


Figure 33.[194] Transcriptional cascade controlling adipocyte differentiation. (Abbreviations: C/EBP homologous protein, CHOP10; retinoic acid receptor, RAR; RAR-related orphan receptor α, RORα; forkhead box O1, FOXO1; thyroid hormone receptor, TR; liver X receptor, LXR; chicken ovalbumin upstream promoter transcription factor II, COUP-TFII.)

To further confirm the involvement of the cAMP signalling pathway in the induction of Tpcn2 gene expression, alternative methods of raising levels of cAMP were used to investigate whether this is the signalling intermediate by which IMBX affects Tpcn2. Rolipram, similar to IBMX, is also a cAMP PDE inhibitor; however, while IBMX is

relatively nonspecific and may affect cAMP levels, rolipram is a specific inhibitor of PDE IV, thus it specifically raises cAMP levels.[193] In contrast, forskolin increases cAMP levels by activating the synthesizing enzyme adenylyl cyclase.[195] I found that both rolipram and forskolin increased Tpcn2 mRNA levels after 4 hours treatment (Figure 34). The increase for both drugs was similar to, though slightly lower than, that seen with IBMX.

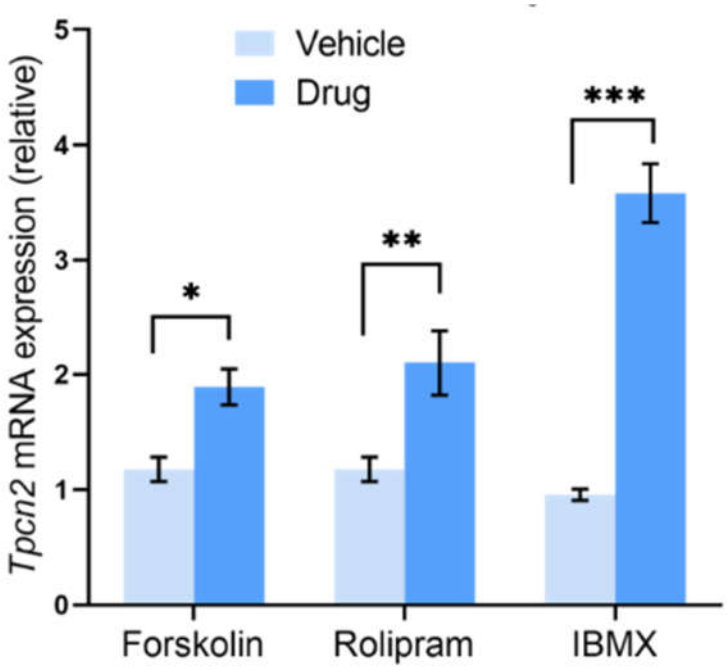


Figure 34. Expression of Tpcn2 mRNA in C3H10T1/2 cells in response to drugs that alter cAMP levels. Cells were treated for 4 hours at 2 days post-confluence with GM containing 50 μM forskolin (in DMSO), 100 μM rolipram (in DMSO), 500 μM IBMX (in 100% ethanol) or vehicle. Significance was measured by student's t-test, n=3, **p<0.01, ***p<0.001. Values are

normalized to the geometric mean of 18S and ubiquitin c mRNA expression and presented as fold-change relative to GM condition.

Further evidence for a role of cAMP in mediating IBMX-induced Tpcn2 mRNA upregulation was provided by our finding that pretreatment with the adenylyl cyclase inhibitor SQ22536 significantly reduced this IBMX-induced rise in expression (Figure 35).[196]

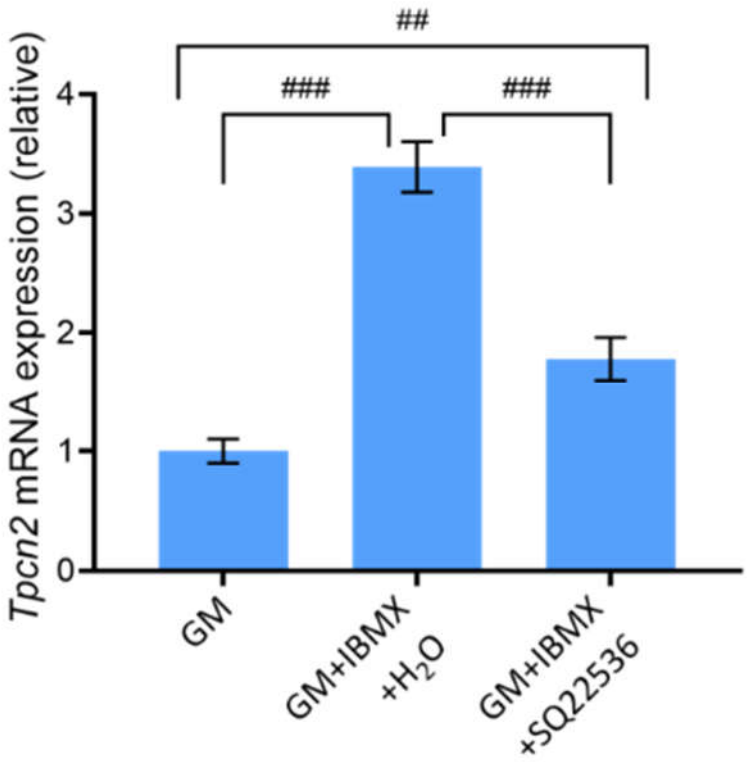


Figure 35. Effect of the adenylyl cyclase inhibitor SQ22536 on IBMX-induced induction of Tpcn2 mRNA expression. 2-day post-confluent cells were preincubated for 30 minutes with GM containing 300 µM SQ22536 or vehicle (water) before 500 µM IBMX was added. Significance was measured by ANOVA, post-hoc Tukey test, n=3, ##p<0.01, ###p<0.001.

Values are normalized to the geometric mean of 18S and ubiquitin c mRNA expression and presented as fold-change relative to GM condition.

At this stage we could see that Tpcn2 expression in the process of adipocyte differentiation is regulated by the cAMP signalling pathway, so I tried to find out which downstream proteins were mediating the regulation. There are some previous studies showing that most effects of cAMP are mediated by two ubiquitously expressed intracellular receptors which are protein kinase A (PKA), or alternatively exchange protein activated by cAMP (Epac).[197] These two receptors are like molecular switches for sensing intracellular cAMP levels and controlling diverse functions.

To investigate the possible involvement of PKA and Epac, inhibitors of these proteins were studied to see whether they had impacts on Tpcn2 gene expression (Figure 36). PKI is used as an inhibitor of PKA and was shown to significantly inhibit Tpcn2 mRNA expression 2 hours after induction of adipocyte differentiation. Treatment with ESI-09, a specific EPAC inhibitor, was shown to significantly inhibit Tpcn2 mRNA expression at 2 hours and this effect continued to the 4-hour time point (Figure 36).

These findings suggest that both PKA and Epac are involved in the cAMP-mediated regulation of Tpcn2 gene expression.

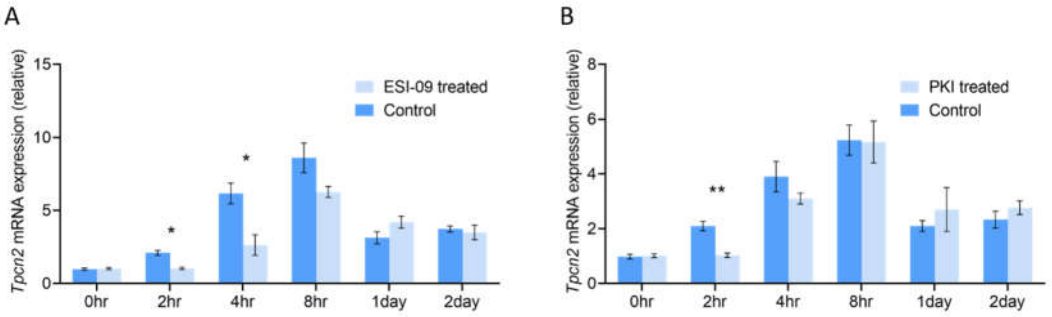


Figure 36. Comparison of Tpcn2 mRNA in non-treated (control) and (A) PKI (PKA inhibitor) / (B) ESI-09 (Epac inhibitor) treated C3H10T1/2 cells. At 2 days post confluence, 10 μM PKI / 25 μM ESI-09/ 1 μM 666-15 were added to the medium during the entire time course of differentiation. Significance was measured by student's t-test, n=5, *p<0.05, **p<0.01. Values were normalized to the geometric mean of β-actin mRNA expression and are presented as expression relative to 0 hr.

4.4 TPC2 plays a functional role during adipocyte differentiation *in vitro*.

The striking transient upregulation of Tpcn2 mRNA expression during differentiation of C3H10T1/2 cells into adipocytes *in vitro*, suggests that TPC2 may be playing a functional role in this process.

Previous researchers in the lab investigated this possibility initially by ectopically expressing recombinant TPC2 protein in C3H10T1/2 cells.

The effects of heterologous TPC2 expression on adipogenic differentiation was assessed by measuring AdipoRed fluorescence. Lentiviral-mediated expression of TPC2 did not affect adipogenic differentiation of C3H10T1/2 cells in response to the standard differentiation protocol. However, when IBMX was omitted from the differentiation medium, this led to almost complete suppression of adipogenesis, but if TPC2 was expressed virally, cells exhibited significantly higher levels of differentiation than mCherry-infected controls. In addition, preadipocyte cells were isolated from WT or Tpcn2 KO mice and induced to differentiate into adipocytes. While cells isolated from WT mice showed a high degree of differentiation, those from Tpcn2 KO mice were inhibited in their differentiation capacity to a significant degree (Figure 37).

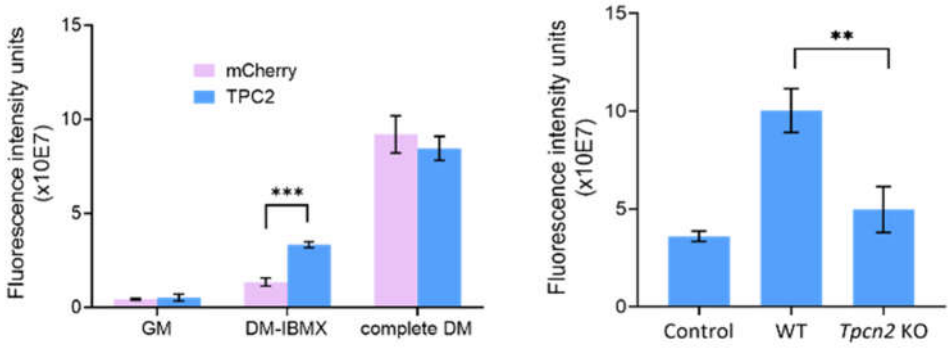


Figure 37. A) AdipoRed quantification of adipogenesis in C3H10T1/2 cells lentivirally infected with mCherry or mCherry-tagged TPC2. Cells were treated according to standard differentiation medium protocol (complete DM); with standard protocol omitting IBMX (DM-IBMX); or maintained in growth medium (GM) and were assayed after 8 days. n=8-12. ***p<0.001 (student's t-test). B) AdipoRed quantification of adipogenesis in primary

preadipocyte cells from WT and Tpcn2 KO mice treated with standard differentiation protocol and control group maintained in growth medium, assayed after 8 days. n=6. **p<0.01 (student's t-test).

4.5 TPC2 regulation of adipocyte differentiation is mediated by calpain.

TPC2 appears to be playing a functional role in adipocyte differentiation *in vitro*, but the question is by which mechanism it does so. Since TPC2 is a Ca^{2+} channel regulated by NAADP, I hypothesised that there may exist a Ca^{2+}-regulated effector protein downstream of TPC2 which is involved in the process of adipocyte differentiation.

Calpain is a cytosolic protease which is activated by calpain activator when intracellular Ca^{2+} concentration is enhanced. A previous study showed that calpain is crucial for differentiation of 3T3-L1 preadipocytes into adipocytes.[198] Interestingly, this same study showed that calpain expression is induced by changes in cAMP levels, just as we have shown in this current study for TPC2. To investigate whether calpain activity is regulated by Ca^{2+} signals mediated by TPC2, I studied changes in calpain activity during differentiation of primary preadipocytes from WT or Tpcn2 KO mice, into adipocytes.

For the WT preadipocytes, what appears to be a gradual rise in calpain activity after induction of differentiation up to 8 hours, is followed by an approximately three-fold

spike in activity at the 24-hour time-point, after which activity decreases and levels off by 4 days (Figure 38). In contrast, for the Tpcn2 KO preadipocytes, I saw a gradual increase in calpain activity that continues up to 8 days, but there is no sign of a transient burst of activity at around 24 hours as is seen for the WT controls (Figure 38). This indicates that calpain activity during adipocyte differentiation is substantially reduced by *Tpcn2* KO, in a qualitatively distinct manner, and suggests that calpain is an effector of TPC2 in this process.

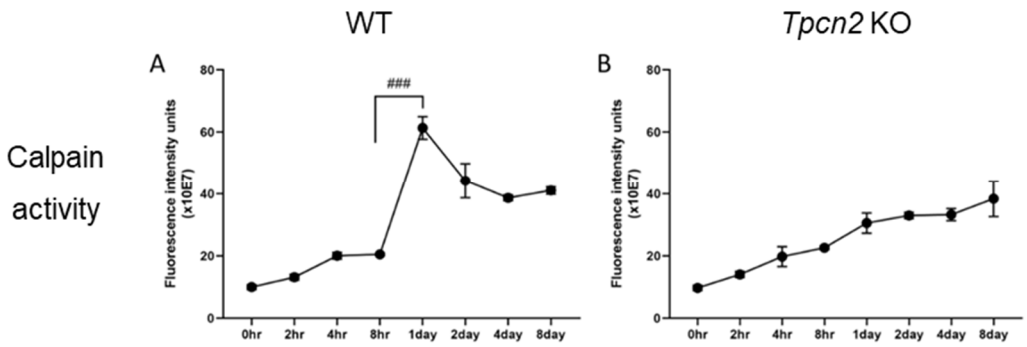


Figure 38. A/B) Variation in calpain activity in the process of primary preadipocyte differentiation. A) WT preadipocytes. n=8, ###p<0.001 (ANOVA, post-hoc Tukey test, compared between consecutive time points). B) Tpcn2 KO preadipocytes. n=3-8.

4.6 CREB phosphorylation during adipocyte differentiation is regulated by TPC2.

In my results above, Tpcn2 mRNA expression during adipocyte differentiation was shown to be regulated by the cAMP pathway, and cAMP response element binding

protein (CREB) seemed to be involved in the process. Since cAMP is activated by PKA and EPAC, it implied that TPC2 is downstream of cAMP-PKA/EPAC-CREB during adipocyte differentiation.

Since reciprocal interactions often exist between components in signalling pathways, I investigated whether Tpcn2 knockout had any effect on the active, phosphorylated state of CREB during adipocyte differentiation. An ELISA assay was employed to compare levels of phosphorylated and unphosphorylated CREB during differentiation of primary preadipocytes from WT or Tpcn2 KO mice, into adipocytes. The results showed that compared to a steadily increasing phosphorylation level of CREB in WT preadipocytes, CREB phosphorylation was inhibited in Tpcn2 KO preadipocytes after 2 days following induction of differentiation (Figure 39, 40). This suggests that TPC2 may normally be playing a role in regulating CREB phosphorylation during the late period of adipocyte differentiation, by a mechanism that remains to be determined in a future investigation.

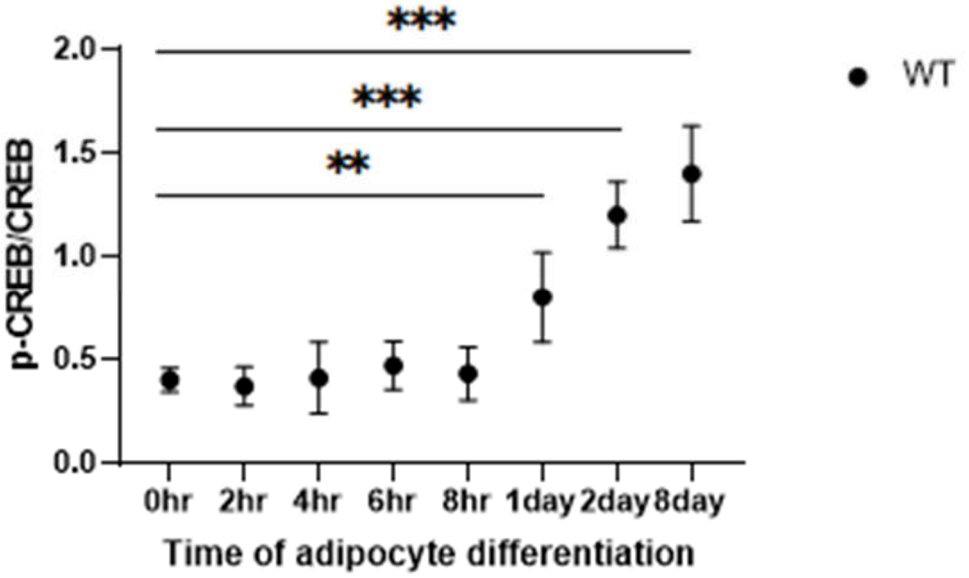


Figure 39. The ratio of optical density (at 450nm) showing the levels of phosphorylated CREB and unphosphorylated CREB during adipocyte differentiation in WT preadipocytes. Significance was measured by one-way ANOVA which was used with a post-hoc Dunnett test comparing all timepoints to expression at 0 hours. n=3, **p<0.01 ***p<0.001.

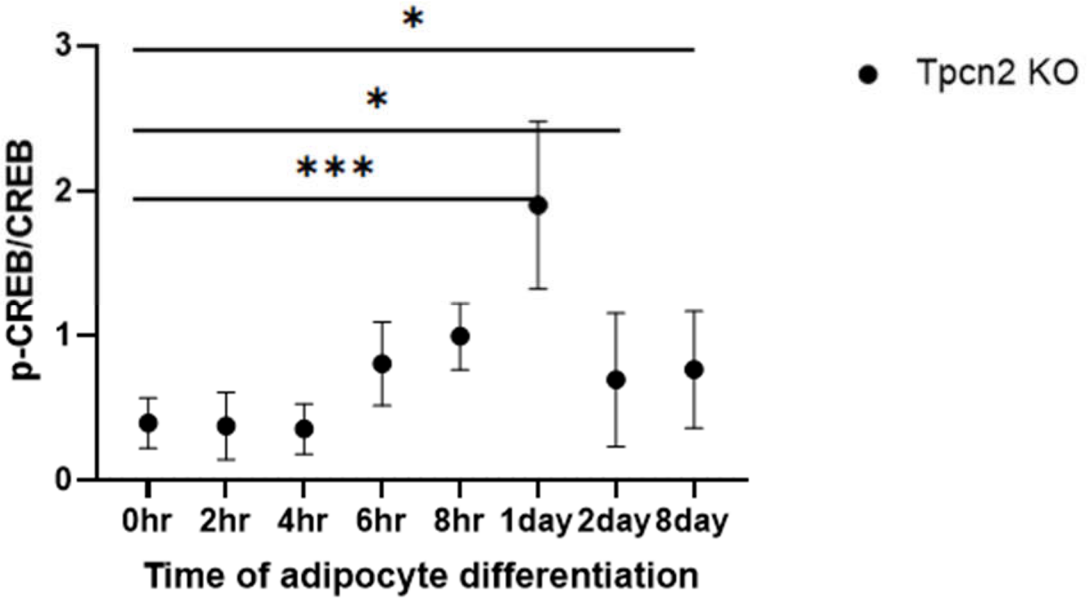


Figure 40. The ratio of optical density (at 450nm) showing the levels of phosphorylated CREB and unphosphorylated CREB during adipocyte differentiation in Tpcn2 KO preadipocytes. Significance was measured by one-way ANOVA which was used with a post-hoc Dunnett test comparing all timepoints to expression at 0 hours. n=3, *$p<0.05$ ***$p<0.001$.

Normally, in order to activate the cAMP signalling pathway, CREB must be phosphorylated by some mechanism and in previous studies multiple protein kinases have been shown to mediate CREB phosphorylation.[199] Interestingly, there are multiple phosphate-acceptor sites on CREB, indicating that there may be multiple phosphorylation events involved in CREB activation.[199] The calcium-calmodulin-dependent protein kinase (CaMKK) is a classic kinase activator of CREB. The CaMKK-mediated kinase cascade take parts in a number of Ca^{2+}-dependent pathways.[200] The involvement of CaMKK in PKA-cAMP signalling, aroused my

interest and led me to suspect that CaMKK may be an mediator through which TPC2 triggers PKA-cAMP signalling.[200]

I therefore used a CaMKK inhibitor to see if CaMKK inhibition would result in a similar inhibitory effect to Tpcn2 knockout. KN-93 Phosphate is a potent and specific inhibitor of Ca^{2+}-calmodulin-dependent protein kinase II (CaMKII) (Figure 41-43). Previous research has shown that KN93 has no obvious inhibitory activity against PKA or Ca^{2+}-PDE and is able to attenuate CaMKK-induced cell functions.[201]

The change of CREB phosphorylation level of KN93 treated cells during adipocyte differentiation is shown below. On day 2, the significant decrease of phosphorylation level in TPC2 KO cells does not happen in the cells treated with KN93, while on day 8, the phosphorylation level was lower than day 1 (Figure 41).

There are two possible explanations for the results. The possibility exists that the dosage of KN93, which is 0.3uM, does not fully inhibit CaMKK. Without considering the experimental problem, the changes of phosphorylation level on day 8 indicate that CaMKK inhibitor partly inhibits the cAMP-TPC-mediated CREB phosphorylation after day 2. And apart from the CaMKK mediated kinase cascade, TPC2 mediates CREB activation through another effector. Future work can be done to investigate whether TPC2 mediates CREB phosphorylation through another kinase; apart from PKA-related mediators, protein kinase C (PKC) may be a good direction for future

research.

The phosphorylation decreases indicate that CaMKK does mediate the phosphorylation triggered by TPC2. To exclude the possibility of dosing-induced cell death, an MTT assay was employed to WT, KN-93 treated and TPC2 KO preadipocytes, and no significant difference in the cell survival rate was detected (Figure 42).

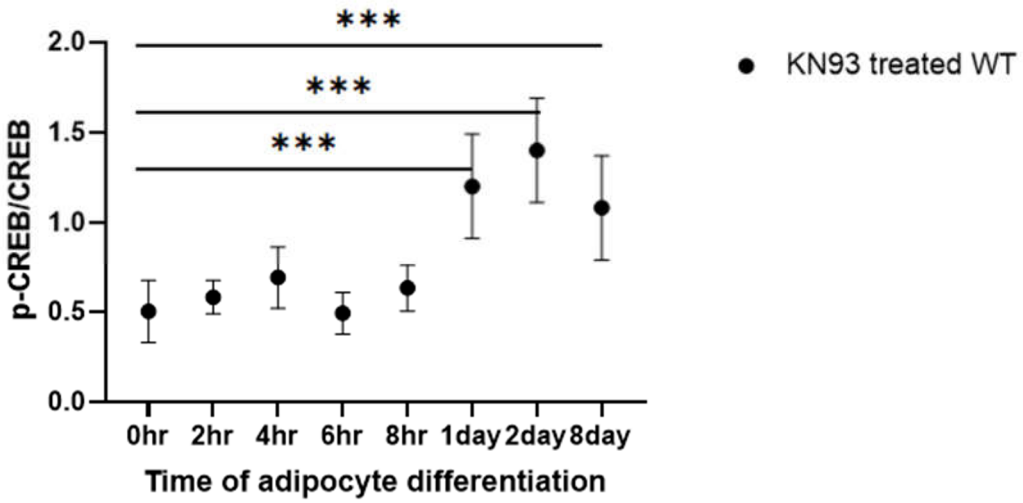


Figure 41. The ratio of optical density (at 450 nm) showing the levels of phosphorylated CREB and unphosphorylated CREB during adipocyte differentiation in wild type preadipocytes treated with CaMK II inhibitor KN93 phosphate. Cells were incubated in 0.3uM KN93 (IC50=1.6 uM) at 37℃ for 10 minutes before each medium changing. Significance was measured by one-way ANOVA used with a post-hoc Dunnett test comparing all timepoints to expression at 0hr. n=3-4, ***p<0.001.

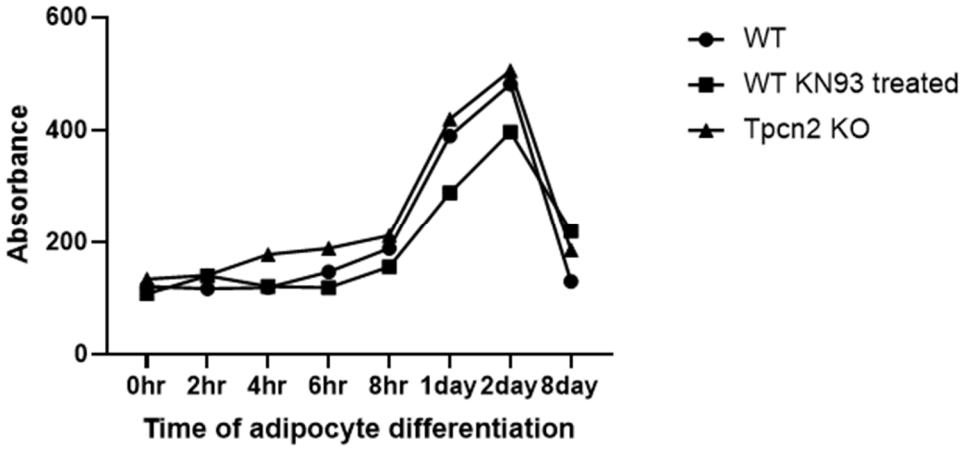


Figure 42. Preadipocyte growth curve detected by MTT assay, cells were passaged on day 4 and day 7 (n=1).

To confirm the results of the phosphorylation change, immuno-blotting was employed to show the visual quantity of the phosphorylated-CREB. Consistent with the ELISA results, the expression level of phosphorylated CREB was significantly decreased by TPC2 KO on day 8 (Figure 43).

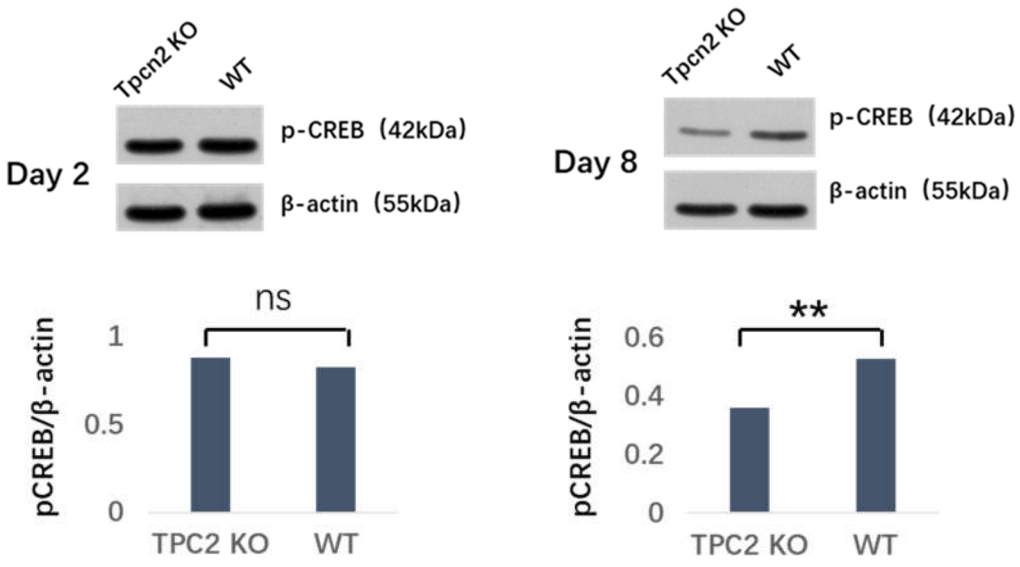
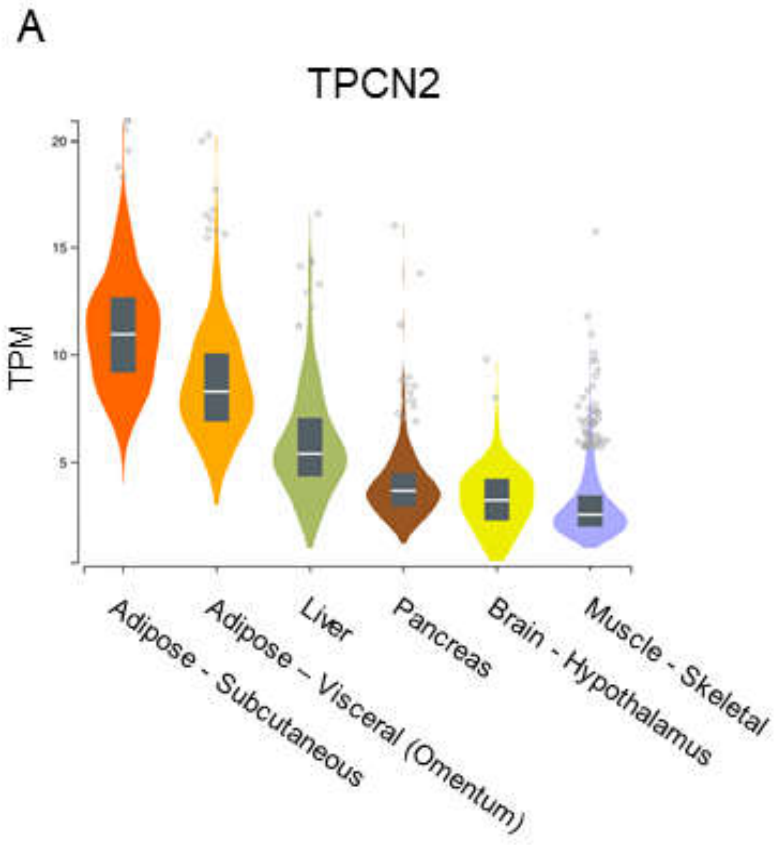


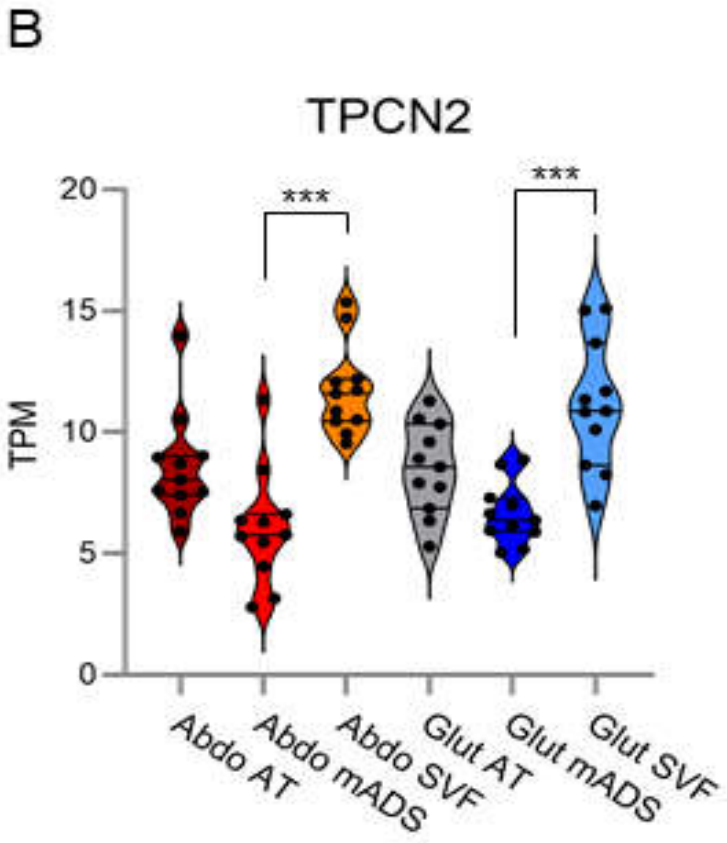
Figure 43. The expression of p-CREB during adipocyte differentiation detected on day 2 and day 8 by western blot in Tpcn2 KO vs. WT preadipocytes. Grey values were measured using Fiji/Image J software. Significance was measured by student's t-test, n=1, *P≤0.01, ***P≤0.0001.

4.7 Genetic variation at the TPCN2 locus is associated with altered fat distribution.

To determine the relevance of our findings for humans we examined the tissue expression pattern of TPCN2 in GTEx.[202] Amongst metabolic organs and tissues, abundance of TPCN2 mRNA was highest in adipose tissue. Furthermore, based on RNA sequencing data from fractionated adipose tissue from 11 females, TPCN2 expression was highest in stromovascular cells compared with mature adipocytes (Fig. 7B). We next interrogated data from the GIANT consortium and UK Biobank combined

genome-wide association study (GWAS) meta-analysis.[203] These revealed that an independent signal at the TPCN2 locus was associated with the waist-hip ratio adjusted for body mass index (WHRadjBMI) specifically in females (beta = 0.0208, p=6.06E-11). The lead single nucleotide variation (SNV) at this signal (rs2305498) lies within an intron of TPCN2 and is a strong expression quantitative trait locus (eQTL) for TPCN2 in subcutaneous abdominal adipose tissue from females based on data from the MUTHER consortium.[204] Notably, the WHRadjBMI increasing allele (G) at this SNV is associated with lower adipose TPCN2 expression (beta = -0.20554, p=4.2E-22) consistent with the pro-adipogenic effect of TPCN2 *in vitro* (Figure 44). Collectively these data suggest that TPCN2 plays an important and sexually dimorphic role in adipose tissue biology and fat distribution in humans.


A
TPCN2
TPM
20
15
10
5
Adipose - Subcutaneous
Adipose – Visceral (Omentum)
Liver
Pancreas
Brain - Hypothalamus
Muscle - Skeletal


B
TPCN2
TPM
20
15
10
5
0
***
***
Abdo AT
Abdo mADS
Abdo SVF
Glut AT
Glut mADS
Glut SVF

C

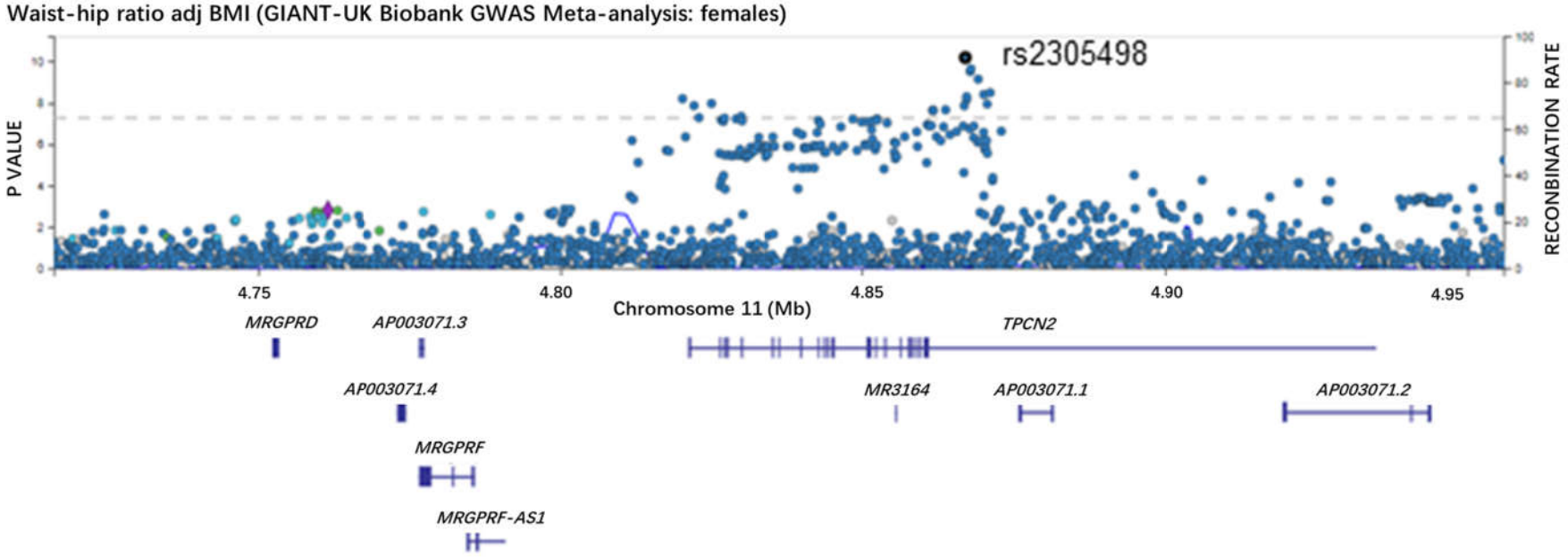

Waist-hip ratio adj BMI (GIANT-UK Biobank GWAS Meta-analysis: females)
rs2305498
P VALUE
RECONBINATION RATE
4.75
4.80
4.85
4.90
4.95
Chromosome 11 (Mb)
MRGPRD
AP003071.3
TPCN2
AP003071.4
MR3164
AP003071.1
AP003071.2
MRGPRF
MRGPRF-AS1

Figure 44. A) TPCN2 is most highly expressed in adipose compared with other metabolic tissues. RNA-Seq data from GTex. B) TPCN2 expression in whole and fractionated adipose tissue. RNA-Seq data from 11 females. AT, adipose tissue, mADS, mature adipocytes, SVF, stomovascular fraction, TPM, transcripts per million. ***$p \leq 0.0001$, two-tailed paired Student's t-test. C) Locus zoom showing a common intronic SNV at TPCN2, rs2305498, is associated with increased waist-hip ratio adjusted for BMI.

4.8 Discussion and conclusion.

Our interest was initially stimulated by the observation that Tpcn2 KO mice of both sexes have both a reduced absolute fat mass and a reduced percentage of fat at three and six months compared to wild-type controls, suggesting that Tpcn2 KO has an effect on adiposity in mice, and that this effect may be modified with age and also affected by the sex of the animals. These findings raise the question of how loss of Tpcn2 expression might give rise to such an effect. One of the problems of pursuing this issue further mechanistically is that with such a whole animal KO, loss of Tpcn2 expression may be having a variety of effects due to changes in the properties of a number of different cell types/tissues, some of which may oppose each other. In addition, a common phenomenon in mice KOs is the occurrence of compensation for loss of expression of the knocked-out gene by changes in the levels and patterns of expression of other genes. Given that compensatory effects may operate from fertilized egg stage onwards, this presents ample opportunity for changes to occur that may modify the

effects of the knocked-out gene and complicate interpretation of what a KO phenotype may reveal about the normal physiological role of that gene in a particular process *in vivo*. We thus chose in the remainder of this study to focus on one potential function for TPC2 in the regulation of the related phenomena of adiposity and adipogenesis, by investigating whether TPC2 plays a role in adipocyte differentiation *in vitro*.

The study is the first demonstration of a cell signalling pathway that can affect the expression of a member of the TPC gene family (Tpcn2). We found that changes in cAMP levels lead to changes in Tpcn2 mRNA expression and previous studies have shown that cAMP can activate protein kinase A (PKA), or alternatively exchange protein activated by cAMP (Epac). Our findings using specific inhibitors of these proteins suggest that both PKA and Epac may be involved in the cAMP-mediated regulation of Tpcn2 gene expression. Further studies will be required to better understand how PKA and Epac regulate Tpcn2 gene expression.

That TPC2 may play a functional role during adipocyte differentiation, is suggested by two main findings in the current study. First, we show that over-expression of TPC2 in C3H10T1/2 cells can partially overcome the block to adipocyte differentiation due to the absence of IBMX from the differentiation cocktail. It remains to be shown why this 'rescue' is only partially effective; one possible explanation could be that IBMX induces other changes that are necessary for differentiation to occur so that TPC2 expression on its own is only partially able to substitute for absence of cAMP signalling.

Second, we show that inhibition of endogenous TPC2 in primary preadipocytes from Tpcn2 KO mice substantially inhibits the ability of these cells to differentiate into adipocytes.

Since previous studies by ourselves and others have identified TPCs as integral components of the NAADP-regulated Ca^{2+} signalling pathway, this raises the question of whether TPC2 mediates adipocyte differentiation via some form of Ca^{2+} signalling response. We chose to study whether the downstream mediator of TPC2 action during adipocyte differentiation might be calpain, since this Ca^{2+}-sensitive protease has previously been shown to be required for differentiation of 3T3-L1 preadipocytes into adipocytes. In this current study we found that in WT preadipocytes, there is a gradual rise in calpain activity after induction of differentiation up to 8 hours, followed by an approximately three-fold spike in activity at the 24-hour time-point, after which activity decreases and levels off by 4 days. In contrast, for the Tpcn2 KO preadipocytes, we saw a gradual increase in calpain activity that levels off by 4 days, but no sign of a transient burst of activity at around 24 hours. The fact that Tpcn2 KO only appears to affect part of the change in calpain activity during adipocyte differentiation, namely that which occurs transiently at around 24 hours after the start of the differentiation process, is interesting given that Tpcn2 mRNA expression also occurs transiently, but in this case peaks at 4-8 hours after the induction of differentiation. One possible explanation for these findings would be that there are multiple calpain isoforms that are

active during the differentiation of preadipocytes to adipocytes, but only one is regulated by Ca^{2+} signals that are generated via TPC2. A previous study suggested that μ-calpain rather than m-calpain was responsible for the control of adipogenesis of ST-13 preadipocytes established from adult primitive mesenchymal cells, through the regulation of the levels of PPARs and C/EBP. It would be interesting therefore in future studies to study whether a specific calpain isoform is being activated by a Ca^{2+} signal originating from TPC2 and whether this is μ-calpain, since this has been specifically implicated in adipocyte differentiation.

In addition, we also showed that the CREB phosphorylation level was enhanced by Tpcn2 KO in the first 24 hours of adipocyte differentiation, although it peaked on day 2 and quickly fell to its base level while in WT preadipocytes, CREB phosphorylation gradually increased during adipocyte differentiation. This suggests that, while our findings indicate that Tpcn2 gene expression is regulated by a mechanism involving cAMP/PKA/EPAC/CREB, there is also a reciprocal regulation of CREB activity by TPC2. This raises the question of the mechanism by which TPC2 might be regulating CREB. One possibility, given that CREB can be phosphorylated by the Ca^{2+}/calmodulin-dependent kinases CaMKII and CaMKIV, is that Ca^{2+} signals induced through TPC2 influence CREB phosphorylation via one or both of these kinases. Further studies will be required to investigate this possibility.

In keeping with the results of the *in vitro* studies, we also demonstrate that the minor allele of a common intronic SNV at *TPCN2*, rs2305498, is associated with increased WHRadjBMI; a surrogate marker of body fat distribution and an independent predictor of cardiometabolic disease risk. Interestingly, the same allele is also associated with reduced TPCN2 expression in subcutaneous adipose tissue and increased estimated heel bone mineral density. Based on these findings we speculate that TPCN2 may limit adipose tissue expansion, thereby promoting upper-body fat accumulation, by altering mesenchymal stem cell fate and promoting adipogenesis at the expense of osteoblastogenesis. This hypothesis is consistent with the expression pattern of TPCN2 in fractionated human adipose tissue and the early and transient induction of Tpcn2 gene expression during adipogenesis of C3H10T1/2 mesenchymal stem cells. Future, studies should focus on confirming that TPCN2 is the effector gene and adipose tissue the target tissue of the WHRadjBMI associations at the TPCN2 locus, as well, as identifying the effector cell types mediating these associations. The role of TPCN2 in osteoblastogenesis should also be investigated.

My aim in embarking on this study was to find further explanations for the up and down stream modulators for the effects of TPC2 in adipocyte differentiation. In the study I identified TPC2 as a novel regulator of adipocyte differentiation and provided evidence showing that the Ca^{2+} dependent protease calpain could be a downstream effector of TPC2. However, there are still some issues to address. One is that the level of

differentiation is mainly assessed by the amount of stored lipid; thus, to improve the study I could evaluate expression of key adipogenic genes during differentiation, particularly Pparγ2, c/Ebpδ and Srebp1 since c/Ebpδ was responsible for the early stage (within 24 hours) of adipocyte differentiation. A second issue is that the evidence showing the relationship between TPC2 expression and calpain activation seems tenuous. Since calpain was first reported to be involved in the regulation of adipocyte differentiation by Ca^{2+} signalling from acidic stores, a more detailed mechanism for how calpain works will need to be revealed in future studies.

Chapter 5: The function of TPCs in SARS-CoV-2 pseudo-virus infection of hepatocytes

5.1 Expression level of Tpcn1 and Tpcn2 in SARS-CoV-2 pseudo-virus infected senile female hepatocytes.

A pseudo-virus is a recombinant virus whose genes are usually altered or modified to eliminate the expression of some of its own proteins. It can infect susceptible host cells but can only replicate once within the cell. Since virus surface proteins play a key role in entering host cells, the conformational structure of pseudo-virus surface proteins is highly similar to that of natural virus proteins. However, pseudo-viruses are less virulent than wild-type (WT) viruses, allowing them to be safely handled in the lab.

SARS-CoV-2 is an RNA virus. Studies have shown that both SARS-CoV-2 and SARS-CoV use angiotensin-converting enzyme 2 (ACE2) as the host cell surface receptor to enter target cells. The first two-thirds of the SARS-CoV-2 genome is named the ORF1ab region, while the remainder encodes several helper proteins and four structural proteins, including spinous process (S) glycoprotein, envelope (E), matrix (M), and nucleocapsid (N) proteins, which are important for maintaining the structural integrity of the envelope of SARS-CoV-2 virions. By replacing the envelope glycoprotein in the lentivirus vector with the novel coronavirus S protein, pseudo-viruses can be formed to simulate the infection of the novel coronavirus. Pseudo-viruses infect target cells with

surface S proteins and express reporter luciferase genes. Neutralizing antibodies can block the binding of S protein to ACE2, thus preventing the infection of the pseudo-virus to the host cell. By detecting the expression level of reporter gene luciferase, the degree of virus blocking can be inferred, so as to screen or verify the potency of the neutralizer. Therefore, pseudo-virus is the first choice to replace real virus in cell level detection as a positive control and standard in a virus nucleic acid detection kit, neutralizing antibody research, vaccine development, and virus receptor research.[205]

Tpcn1 and Tpcn2 knockdown (KD) pancreatic acinar cell (PAC) and hepatocyte models were established by siRNA transfection. Here the results of RT-qPCR show the degree of knock-down. I used gadph as the internal reference and determined the amount of extracted RNA with balanced expression level of gadph. We can see a 40.5% knockdown of Tpcn1 in PACs, and 26.2% knockdown of Tpcn1 in hepatocytes (Figure 45). In addition, we can see a 56.5% knockdown of Tpcn2 in PACs, and 40% knockdown of Tpcn2 in hepatocytes (Figure 45).

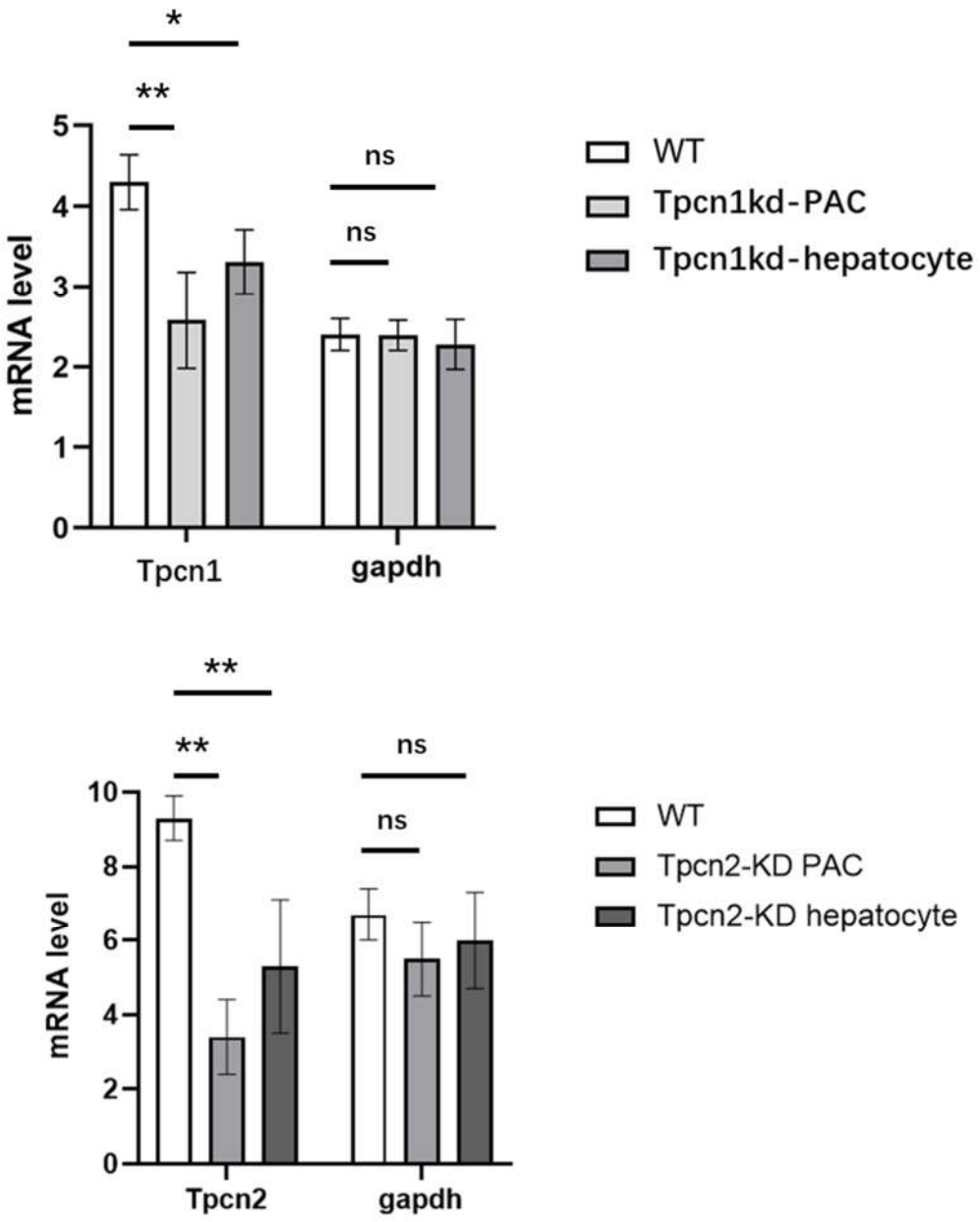


Figure 45. Tpcn1/2 knockdown by small interfering RNA (siRNA) transfection in freshly isolated hepatocytes with a degree of 26% for Tpcn1 and 41% for Tpcn2. A) The knockdown validation of Tpcn1 gene edited pancreatic acinar cells and hepatocytes. B) The knockdown validation of Tpcn2 gene edited pancreatic acinar cells and hepatocytes. Significance was measured by unpaired student's t-test, values were compared to WT, *P≤0.01, ** P≤0.001.

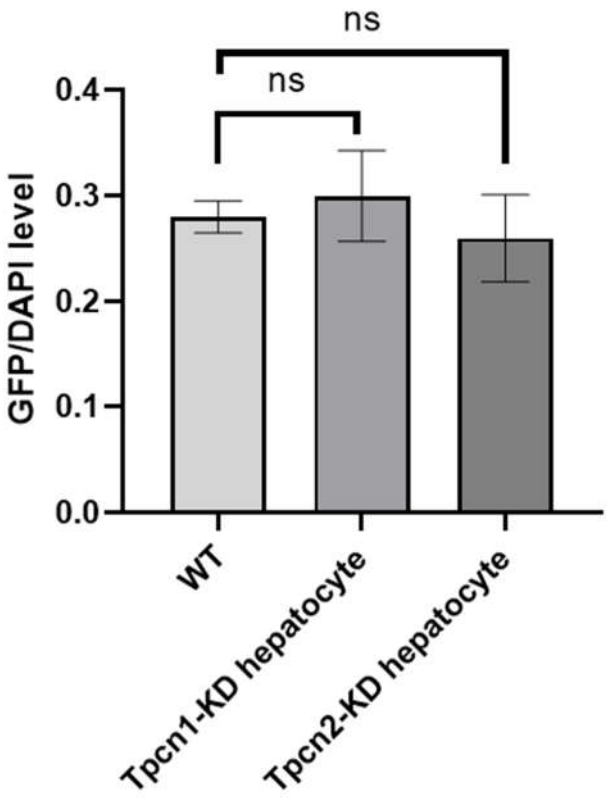


Figure 46. The efficiency of pseudo-virus infection in wild-type hepatocytes (n=3) vs. Tpcn1 knockdown (n=5) and Tpcn2 knockdown (n=5) in hepatocytes. Significance was measured by unpaired student's t-test; values were compared to WT.

Unfortunately, freshly isolated acinar cells can only survive for less than 3 hours and are then not eligible for further processes after siRNA transfection, and some experiments also proved that further pseudo-virus infection for pancreatic acinar cells did not succeed. But most freshly isolated hepatocytes can survive for more than 48 hours after siRNA transfection. From the result we can see that both Tpcn1-KD and Tpcn2-KD hepatocytes are equally sensitive as WT hepatocytes to pseudo-virus

infection (Figure 46). GFP tagged pseudo-virus was kindly provided by Dr. Shi-Hao Zhou and Prof. Jun Guo from Central China Normal University.

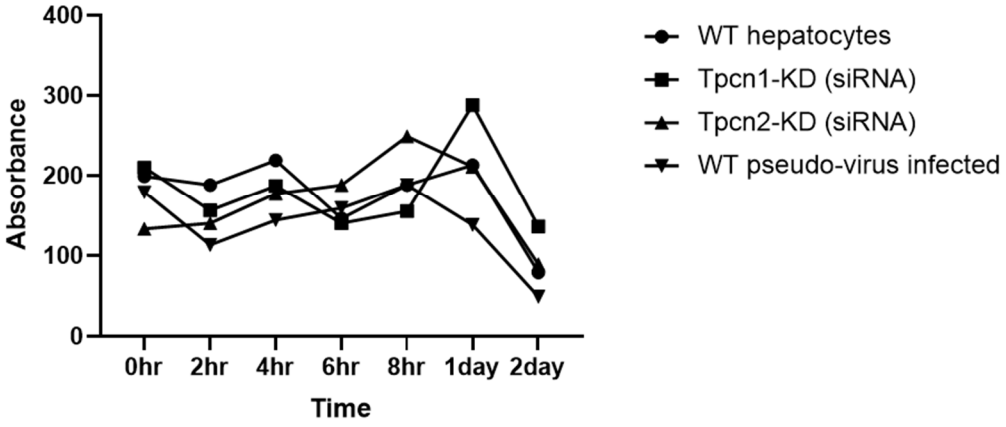
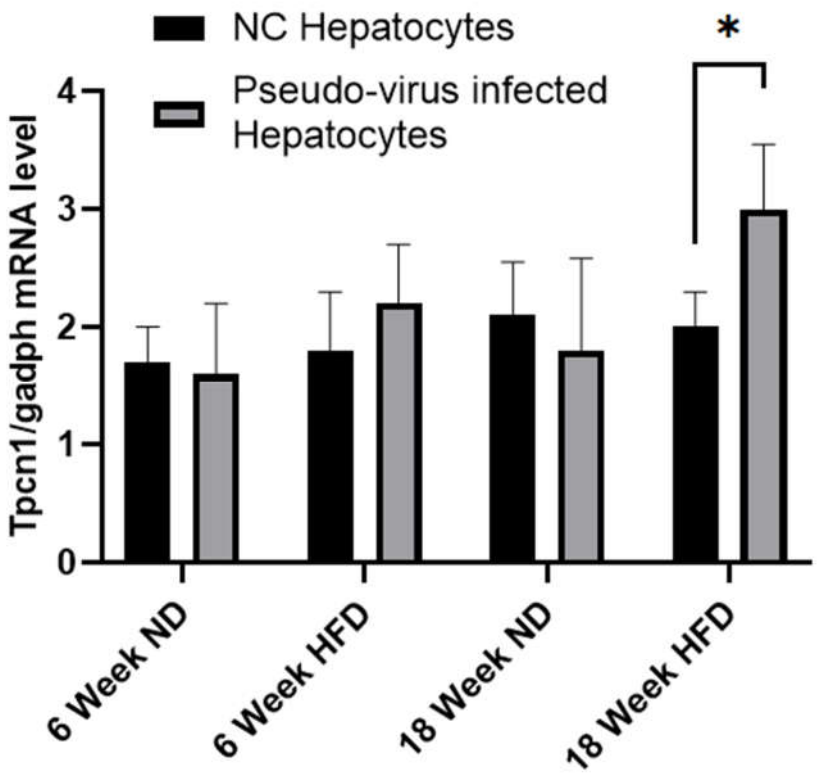


Figure 47. Hepatocyte survival curve detected by colorimetric MTT assay; cells were collected after centrifugation and medium was changed on day 1.

5.2 Pseudo-virus infected hepatocytes from female senile mice on a high-fat-diet show higher Tpcn2 mRNA levels.

Tpcn1 and Tpcn2 mRNA levels in hepatocytes were determined by RT-qPCR in natural control hepatocytes vs. pseudo-virus infected hepatocytes, with consideration of factors such as age and life habits. Four groups of mice were used which were 6-week-old mice with normal diet, 6-week-old mice with high fat diet, 18-week-old mice with normal diet, and 18-week-old mice with high fat diet. We can see from the results that Tpcn1 and Tpcn2 changes in expression were not regular. The only significant difference is in

the hepatocytes of 18-week-old high-fat-diet mice, in which Tpcn1 expression was higher in pseudo-virus infected hepatocytes than in natural control hepatocytes (Figure 48).



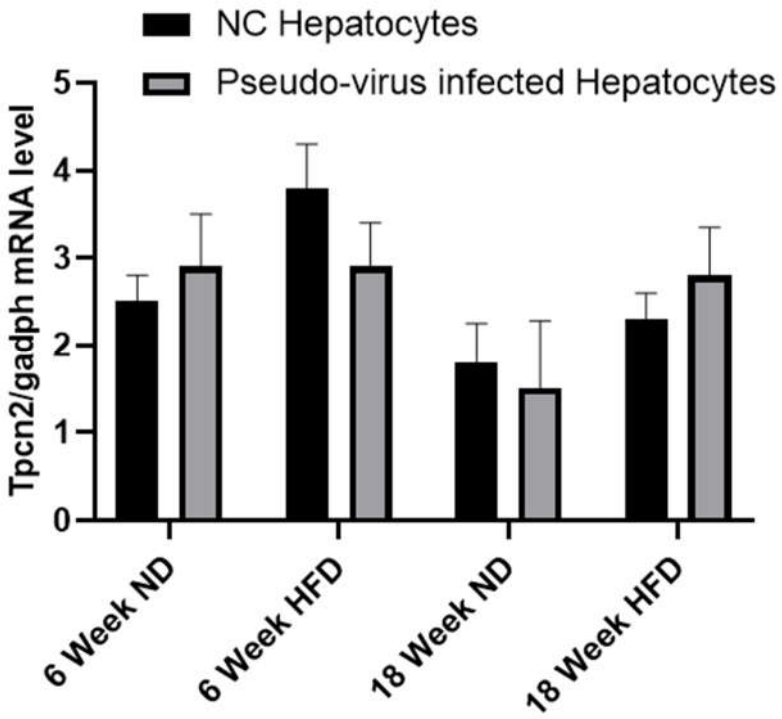


Figure 48. A) Tpcn1 mRNA (vs. gadph) in natural control vs pseudo-virus infected hepatocytes in four groups of mice. B) Tpcn1 mRNA (vs. gadph) in natural control vs pseudo-virus infected hepatocytes in four groups of mice. Multiple unpaired t-test was used for significancy analysis (* means $p < 0.01$).

5.3 Previous research has shown that TIMP1 plays an important role in SARS-CoV-2 infection.

The TIMP (matrix metalloproteinase inhibitor) family is a group of glycoproteins expressed in tissues of various organisms. They act as endogenous protease inhibitors that bind matrix metalloproteinases (MMPs) in 1:1 to form complexes that regulate the

activation or function of MMPs.[206]

There are four TIMPs in human cells. TIMP-1 was first purified in 1981, TIMP-2 was cloned in 1990, TIMP-3 in 1992, and TIMP-4 was identified in 1996. TIMP-1 and TIMP-3 are glycoproteins, while TIMP-2 and TIMP-4 contain no carbohydrates. TIMP-1, TIMP-2, and TIMP-4 are secretory proteins, while TIMP-3 is membrane-bound (Figure 49).[206]

Here we focus on TIMP-1 which is a peptidase containing Zn^{2+} and Ca^{2+} and is involved in the metabolism and degradation of extracellular matrix. Studies have shown that the major function of TIMP-1 includes protection of cell adhesion and blocking of invasion. Recently research has shown that TIMP-1 levels were enhanced in the serum of patients with Covid-19, suggesting that TIMP-1 was associated with the infection by coronavirus and was related to the severity of Covid-19. Researchers suggested that targeting matrix metalloproteases could be a method of treatment of Covid-19 (Figure 50).[207]

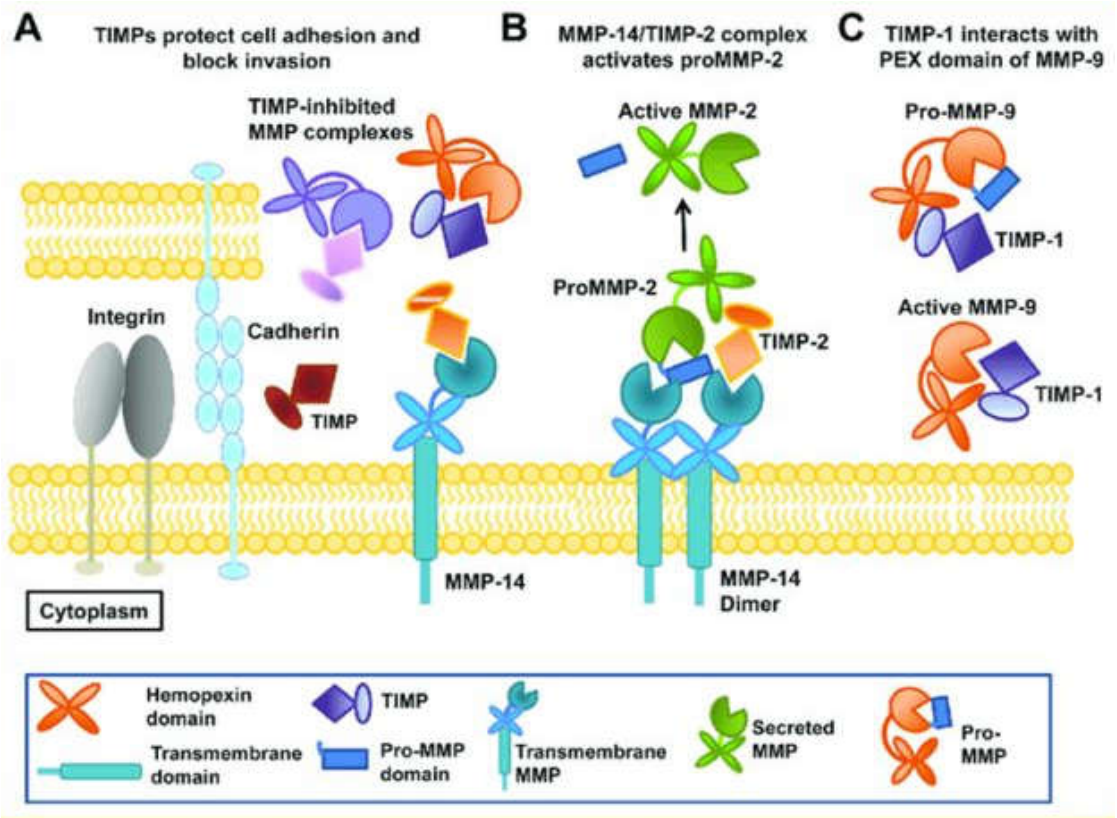


Figure 49. A) The primary function of TIMPs is to protect cell adhesion and block invasion. B) TIMP-2/MMP-14 complex activates proMMP-2. 3) TIMP-1 interacts with the PEX domain of MMP-9.

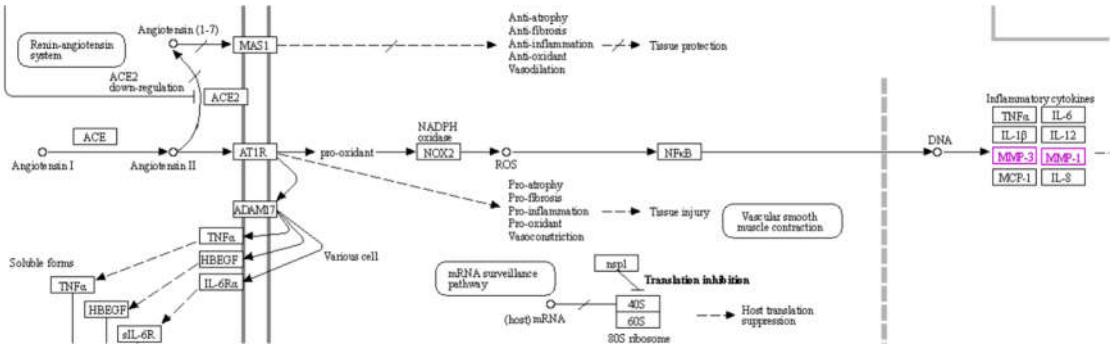


Figure 50. Coronavirus disease reference pathway with MMPs as inflammatory cytokines and with TIMP1 as a mediator.

5.4 Pseudo-virus infection triggered TIMP1 up-regulation which was rescued by Tpcn1 KD in hepatocytes.

In order to see whether the up-regulation of Tpcn1 in senile mice on a high fat diet has any relationship with TIMP-MMP signalling pathways, the TIMP-1 expression level was analysed by western blot in Tpcn1 KD vs. WT hepatocytes infected with SARS-COV-2 pseudo-virus.

The results of the western blot showed that after 48 hours of pseudo-virus (PSV) infection, TIMP-1 was indeed up-regulated in hepatocytes. In addition, if we compared the degree of the TIMP1 enhancement, WT hepatocytes showed a higher level of TIMP-1 up-regulation than Tpcn1 KD hepatocytes, which means that Tpcn1 knockdown somehow prevents the TIMP-1 enhancement triggered by pseudo-virus (PSV) infection (Figure 51, 52).

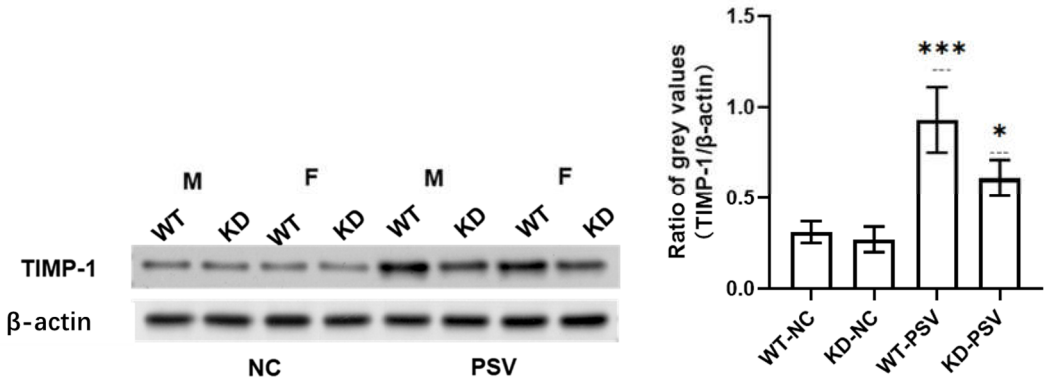
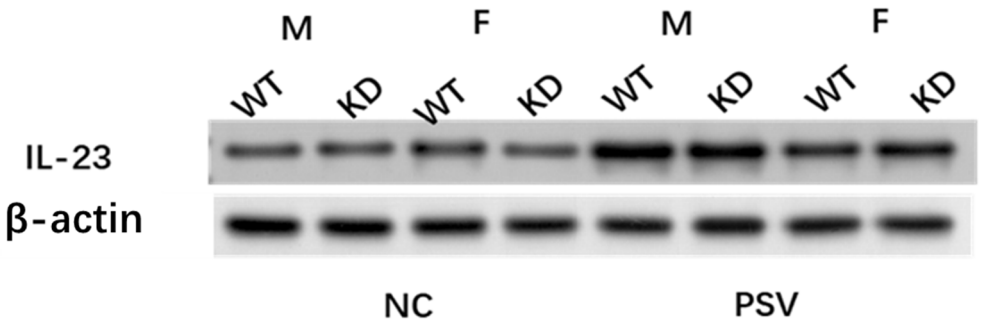


Figure 51. TIMP-1 vs GAPDH expression in WT vs. Tpcn1 knockdown hepatocytes with or without pseudo-virus (PSV) infection. (WT-wild-type, KD-Tpcn1 knock-down, NC-natural control, PSV-pseudo-virus.) Grey values were measured using Fiji/Image J software. Significance was measured by two-way ANOVA, *P≤0.01, ***P≤0.0001.



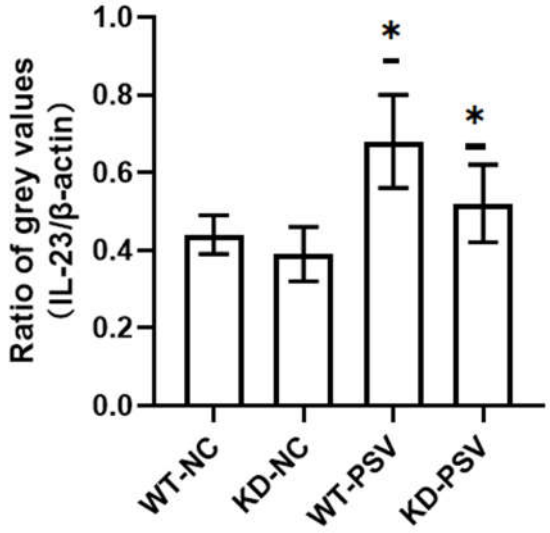


Figure 52. IL-23 vs GAPDH expression in WT vs. Tpcn1 knock-down hepatocytes with or without pseudo-virus (PSV) infection. (WT-wild-type, KD-Tpcn1 knock-down, NC-natural control, PSV-pseudo-virus.) Grey values were measured using Fiji/Image J software. Significance was measured by two-way ANOVA, *P≤0.01.

5.5 Discussion.

Ca^{2+} signalling triggered by NAADP and mediated by TPCs is regarded as an important mechanism in many types of viral infections which can be targeted by drugs. This initiated my interest in investigating a similar involvement in SARS-CoV-2 infection.

Previously, most studies have used mice or human cell lines for pseudo virus infection. This is the first research that used freshly isolated hepatocytes as a model for a SARS-CoV-2 infection study. The advantage of this is that freshly isolated primary cells remain in normal cell cycles and can better mimic *in vivo* physiological cell functions. Although the results of this part of study are very preliminary, there are some interesting points that warrant further exploration.

First, the up regulation of Tpcn1 mRNA by SARS-CoV-2 pseudo virus infection in senile high-fat-diet fed mice but not in younger and normal diet fed mice, may indicate that TPC1 exerts certain effects on pseudo virus infection but the effects seem to be related to age and health. However, how age influences the phenotype of the infected hepatocytes is unclear. At this stage, we cannot assume that age is affecting infection at the cellular level. Since the experiments were duplicated with the same mice, further experiments should involve larger sample numbers. But the trend of high Tpcn1 mRNA expression in pseudo virus infected hepatocytes seems solid and worthy of further exploration.

Second, it has been shown in clinical samples that SARS-CoV-2 infection up regulates the circulating levels of TIMP-1, which is an endogenous protease inhibitor regulating matrix metalloproteinases (MMPs). The possible relationship between TIMP-1 expression in hepatocytes and lysosomal Ca^{2+} signalling was therefore studied. TIMP-1 has been well studied in the fields of cell growth, apoptosis, angiogenesis, oncogenesis, and heart failure, but few studies have looked at its role in viral infection. It therefore seems worth further exploring why TIMP-1 expression was affected by pseudo virus infection and seemed to be rescued by TPC1 knockdown.

Angiotensin-converting enzyme 2 (ACE2) and transmembrane serine protease 2 (TMPRSS2), which are crucial proteins needed for SARS-COV-2 viral entry, were shown to be significantly up-regulated in pneumonocytes upon exposure to high-fat-diet.[208] Since the up-regulation of TPC1 mRNA level can hardly be directly mediated by virus infection, it will be very interesting to further investigate whether this could be mediated by high-fat-diet-induced up-regulation of ACE2 and TMPRSS2. To be more specific, future studies could investigate whether there is a specific transcription factor regulating Tpcn1 expression that could be modulated by ACE2 and TMPRSS2.[209]

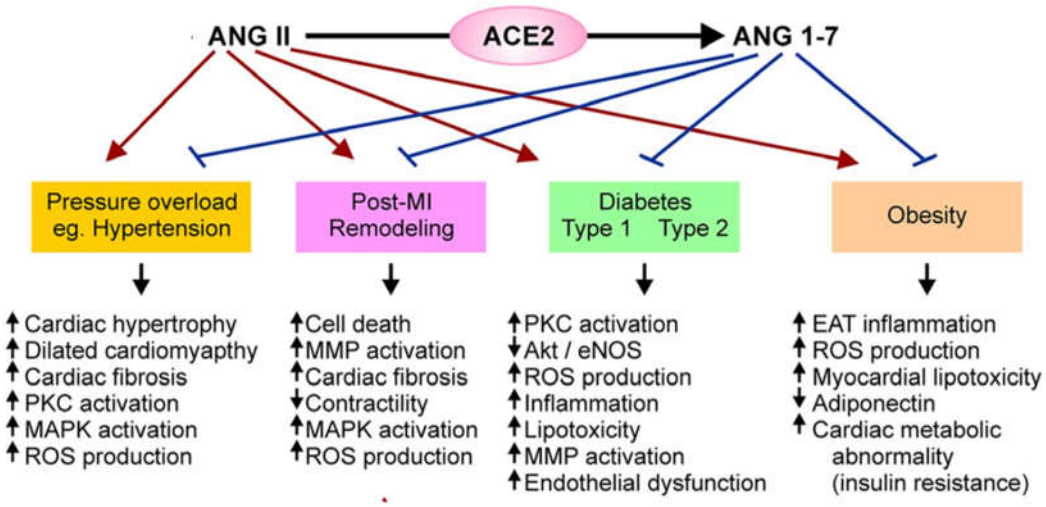


Figure 53. The physiological functions of angiotensin II (AngII), angiotensin1-7 (Ang1-7), and angiotensin-converting enzyme 2 (ACE2). [210,211]

Angiotensin II (AngII) is the core effector molecule of the RAS system. Generally, ACE2 cleats AngII into Ang1-7 polypeptide, which has the effects of protecting the heart, dilating blood vessels, is anti-growth and anti-proliferation, and can also enhance the activity of bradykinin (Figure 53). Future studies can focus on whether these processes regulated by ACE2 are related to a specific transcription factor that regulates Tpcn1 expression. The possibility exists that ACE2 modulates Tpcn1 levels by regulating the activation of a certain MMP involved in the transcription of Tpcn1.[210,211]

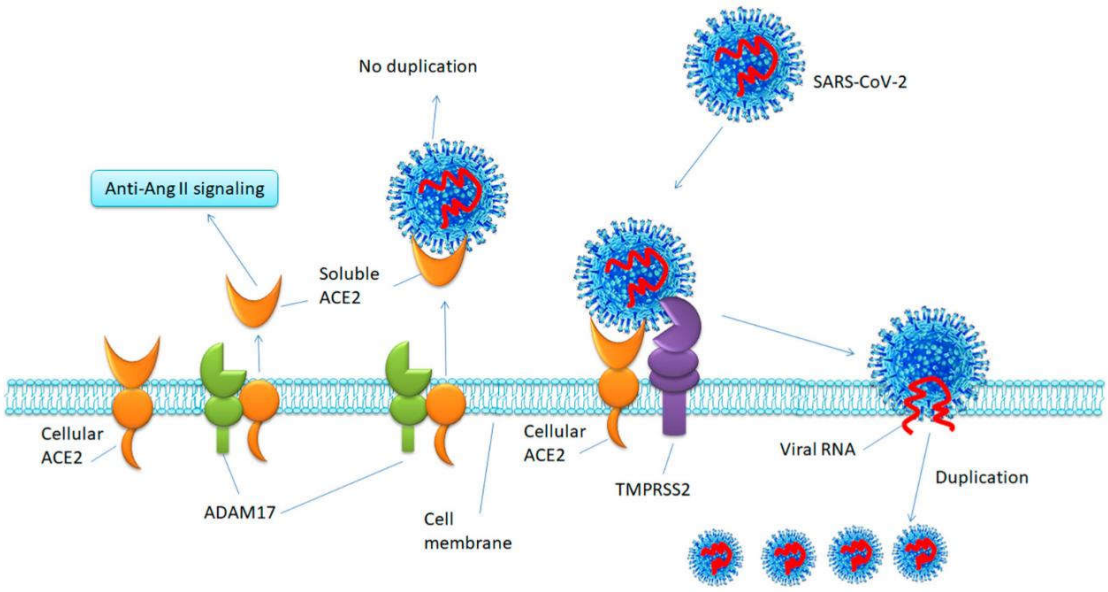


Figure 54. The function of angiotensin-converting enzyme 2 (ACE2) and transmembrane serine protease 2 (TMPRSS2) in the physiological process of SARS-CoV-2 viral entry. [209]

TMPRSS2 is a member of the serine protease family. It is known that serine proteases play key roles in many physiological and pathological processes such as protein catabolism, blood clotting, cell growth and migration, tissue development, and tumour growth and metastasis. The main function of TMPRSS2 in SAR-COV-2 viral entry is that TMPRSS2 cleaves ACE2 and results in an increase in the number of SARS-COV-2 virions entering the cells (Figure 54). Unfortunately, until now, other cellular functions of TMPRSS2 have been seldom studied, thus, we know little about the potential link between TMPRSS2 and Ca^{2+}. Since it seems that Tpcn1 transcription could be up-regulated by the viral infection of hepatocytes, the possibility exists that the TMPRSS2 overexpression could be mediating this up-regulation of Tpcn1 upon

exposure to a high-fat-diet. Future studies can focus on whether TPC1 has any link with TMPRSS2 at the genetic or protein level. [209]

Chapter 6: Conclusion and future work

6.1 Conclusion.

Calcium (Ca^{2+}) signals and their cellular functions are extremely complex and they have been investigated from various aspects in the past few decades. Endolysosomal Ca^{2+} release is especially complicated because of the small amount of Ca^{2+} released and its spatiotemporal character. For commercial purposes, interest in developing Ca^{2+} signalling proteins as drug targets has declined because of the involvement of too many physiological and pathological processes that have caused difficulties in balancing efficacy and side effects. However, for academic purposes, investigations into how Ca^{2+} signals are generated continue to generate important new insights. Two pore channels (TPCs), a type of cation channel on endolysosomes, were shown to mediate NAADP triggered Ca^{2+} release, as well as other forms of ion transport. As the molecular characters of TPCs are increasingly clear after the disclosure of their structures, their functions (how they work) and mechanisms (how are they regulated) in a variety of diseases are arousing much interest. TPC gene-edited animal and cell models have been well studied with regard to various physiological and pathological processes such as apoptosis, oncogenesis, neurogenesis, and cardiovascular function. In my study, I put emphasis on the investigation of TPCs in lipid metabolism, and at the same time, I also investigated the function of TPCs in SARS-CoV-2 infection. For the first time, my study has revealed that TPCs take part in the activation of various enzymes in pancreatic

acinar cells which are involved in diverse cellular functions, particularly fatty acid β-oxidation. Also, this is the first study that reveals the relationship between the Ca^{2+} release mediated by TPCs and cytochrome C, Lsm12, and TIMP-1 expression in the cytosol under particular physiological conditions. In addition, my study is the first to report that calpain and CREB are the downstream effectors of TPCs in the process of adipocyte differentiation.

Previously, unpublished studies had reported that Tpcn1 knockout alters the process of granulate zymogen exocytosis in pancreatic acinar cells by impairing Ca^{2+} release from acidic stores, which was regarded as the reason why Tpcn1-null mice have abnormal lipid absorption. In Chapter Three, I have further shown that the activity of lipase as well as other digestive enzymes is also impaired by Tpcn1 knockout, and this effect seems to be age-related. In addition, my proteomic sequencing results have shown that the activities of some critical enzymes other than digestive enzymes were also impaired in TPC1 knockout pancreatic acinar cells, which resulted in deficiencies of various physiological processes especially fatty acid β-oxidation. These deficiencies at cellular level further may have implications for the progression of various neurodegenerative diseases, potentially by the mechanisms of mitochondrial Ca^{2+} overload. In fact, Gene Ontology analysis of the proteomic results also revealed that a few other biological processes were affected by the absence of TPC1; these include the acylglycerol metabolic process, lipoxygenase pathway, fatty acid elongation, lipid oxidation, and the

tricarboxylic acid cycle. Similarly, molecular functions including oxidoreductase activity, fatty acid derivative binding, and the activity of various enzymes are also modified by TPC1 loss. Although these points are not deeply investigated in my study, they are very interesting and worth of exploration in future. Finally, further investigation of TPCs in pancreatic acinar cells showed that the abundance and expression of cytochrome C, a critical regulator of apoptosis, were suppressed by TPC1/2 double-knockout. This is the first study that employed Raman Spectra microscopy to see the components of pancreatic acinar cells and showed that the expression of cytochrome C is related to the pathways of Ca^{2+} signalling, particularly Ca^{2+} release from intracellular stores through TPCs. This may open a new horizon for future studies in the investigation of both cytochrome C and TPCs. Also, the expression of Lsm12, which was recently identified as an NAADP binding protein, is impaired in TPC1/2 double-knockout pancreatic acinar cells. Most studies in this field focus on the molecular function of Lsm12 and this is the first study showing that the abundance of Lsm12 was affected by TPC loss. These results in pancreatic acinar cells help to reveal the function of TPCs in digestive enzyme activation as well as other physiological and pathological processes.

In Chapter Four, I have investigated the function of TPC2 in adipocyte differentiation extending from previous unpublished findings in our lab. During adipocyte differentiation, TPC2 was up regulated by IBMX, one of the ingredients in the

adipocyte differentiation medium which induces cAMP signalling with involvement of PKA and EPAC. In my studies, I have further identified calpain and CREB as the downstream effectors in this process, with the evidence showing that the activity of calpain was partly inhibited, and CREB phosphorylation was suppressed during the differentiation process of preadipocytes isolated from Tpcn2-null mice. Unfortunately, the calpain activity was tested by the detection of cleavage of calpain substrate Ac-LLY-AFC which reacts with both calpain-1 and calpain-2, thus my study here did not reveal which subtype of calpain was involved in the cAMP signalling and plays a role in adipocyte differentiation with the involvement of TPCs. This could be an important focus for future work. Furthermore, I have performed a study of clinical data showing that the minor allele of a common intronic SNV at human TPCN2 is associated with increased WHRadjBMI. All these results reveal an interesting story about TPC2's role in adipogenesis indicating that TPC2 may limit adipose tissue expansion, thereby promoting upper-body fat accumulation, by altering mesenchymal stem cell fate and promoting adipogenesis at the expense of osteoblast genesis.

In Chapter Five, I describe how a SARS-CoV-2 pseudo-virus was employed to investigate the SARS-CoV-2 infection process in freshly isolated hepatocytes. Previous studies have revealed that TPC-mediated Ca^{2+} release from acidic stores regulates the process of entry of the virus into cells in SARS-CoV-2 infection. Clinical data also showed that serum TIMP-1 has been up regulated by SARS-CoV-2 infection. In my

study, my results show a trend of high Tpcn1 mRNA expression in pseudo-virus infected hepatocytes especially in high-fat diet fed senile mice. In addition, the up regulation of TIMP-1 expression in the cytosol by pseudo-virus infection was partly rescued by TPC1 knockdown. This suggests that TPC1 may play an important role in the high expression of TIMP-1 induced by SARS-CoV-2 pseudo-virus infection. These results may indicate that TPC1 regulates the process of viral entry through a pathway with the involvement of TIMP-1.

In summary, this study has brought several new ideas to the investigation of the function of TPCs in various physiological and pathological processes. Although many of the investigations are preliminary at the current stage, they provide a very good basis for new directions in further studies in this field.

6.2 Future work.

The results of my study have established a solid foundation for further research. With regard to pancreatic functions, the digestive enzyme secretion and activation should be detected using fresh pancreatic juice and pancreas tissues. Also, the relationship between mitochondrial Ca^{2+} overload and Ca^{2+} release from acidic stores should be clarified. In addition, the upstream modulators of the expression of cytochrome C should be investigated to see if they have any link with TPCs or NAADP triggered Ca^{2+} signalling. In the long term, there are more details to be investigated in the results of proteomic analysis, for example, the mechanism of some other biological processes that were affected by TPC1 loss such as the acylglycerol metabolic process, the lipoxygenase pathway, and fatty acid elongation, all of these being interesting points for future investigation.

With regard to adipocyte differentiation, different TPC gene-edited mice models should be used to compare their actual health conditions and body fat percentages since previous study reported that Tpcn2-null mice are more susceptible to fatty liver disease.[212] For the same reason, a Tpcn1/2-null high-fat diet fed mice model should be established. In addition, the actual location of calpain in the cAMP signalling pathway, and also, which subtype of calpain (calpain-1 or calpain-2 or both) is involved in the adipocyte differentiation and was affected by the absence of TPCs, are very interesting points for future investigation. Calpain activities could be studied in the process of

adipocyte differentiation without IBMX as a cAMP inducer. Moreover, cell models other than mesenchymal stem cells and preadipocytes should be also employed to see whether calpain takes part in cAMP signalling in such cells and is deactivated by TPC-KO, and whether this ends up leading to changes in other physiological processes.

In terms of infection, *in vivo* studies should be carried out to see if TPC gene-editing has any effect on serum TIMP-1 levels. It will also be interesting to investigate whether serum TIMP-1 levels are related to the expression of TIMP-1 in cells, especially regarding to SARS-CoV-2 infection.

References.

1. M. Hofer, A. Interactions Between Calcium and cAMP Signalling. *CMC* **19**, 5768–5773 (2012).

2. Daverkausen-Fischer, L. & Pröls, F. Regulation of calcium homeostasis and flux between the endoplasmic reticulum and the cytosol. *Journal of Biological Chemistry* **298**, 102061 (2022).

3. Römling, U. Cyclic di-GMP, an established secondary messenger still speeding up: Cyclic di-GMP signalling. *Environmental Microbiology* **14**, 1817–1829 (2012).

4. Iqbal, J., Zaidi, M. & Avadhani, N. G. Cell signalling: Iqbal et al. *Annals of the New York Academy of Sciences* **1211**, 3–8 (2010).

5. Wang, Q., Yang, S., Wan, S. & Li, X. The Significance of Calcium in Photosynthesis. *IJMS* **20**, 1353 (2019).

6. Paredes-Gamero, E. J. Calcium signalling as a regulator of hematopoiesis. *Front Biosci* **E4**, 1375–1384 (2012).

7. Sukumaran, P. *et al.* Calcium Signalling Regulates Autophagy and Apoptosis. *Cells* **10**, 2125 (2021).

8. Weiser, A., Feige, J. N. & De Marchi, U. Mitochondrial Calcium Signalling in Pancreatic β-Cell. *IJMS* **22**, 2515 (2021).

9. Morgan, A. J. Ca^{2+} dialogue between acidic vesicles and ER. *Biochemical Society Transactions* **44**, 546–553 (2016).

10. Prakriya, M. & Lewis, R. S. Store-Operated Calcium Channels. *Physiological Reviews* **95**, 1383–1436 (2015).

11. Thul, R. Translating Intracellular Calcium Signalling into Models. *Cold Spring Harb Protoc* **2014**, pdb.top066266 (2014).

12. Woll, K. A. & Van Petegem, F. Calcium-release channels: structure and function of IP_3 receptors and ryanodine receptors. *Physiological Reviews* **102**, 209–268 (2022).

13. Mikoshiba, K. & Hattori, M. IP_3 Receptor-Operated Calcium Entry. *Sci. STKE* **2000**, (2000).

14. Astigiano, C. *et al.* Paracrine ADP Ribosyl Cyclase-Mediated Regulation of Biological Processes. *Cells* **11**, 2637 (2022).

15. Lee, H. C. Cyclic ADP-ribose and Nicotinic Acid Adenine Dinucleotide Phosphate (NAADP) as Messengers for Calcium Mobilization. *Journal of Biological Chemistry* **287**, 31633–31640 (2012).

16. Galione, A. & Ruas, M. NAADP receptors. *Cell Calcium* **38**, 273–280 (2005).

17. Albrieux, M., Lee, H. C. & Villaz, M. Calcium Signalling by Cyclic ADP-ribose, NAADP, and Inositol Trisphosphate Are Involved in Distinct Functions in Ascidian Oocytes. *Journal of Biological Chemistry* **273**, 14566–14574 (1998).

18. Lee, H. C. & Aarhus, R. A Derivative of NADP Mobilizes Calcium Stores Insensitive to Inositol Trisphosphate and Cyclic ADP-ribose. *Journal of Biological Chemistry* **270**, 2152–2157 (1995).

19. Mojžišová, A., Križanová, O., Žáčiková, Ľ., Komínková, V. & Ondriaš, K. Effect of nicotinic acid adenine dinucleotide phosphate on ryanodine calcium release channel in heart. *Pflügers Arch - Eur J Physiol* **441**, 674–677 (2001).

20. Cancela, J. M., Churchill, G. C. & Galione, A. Coordination of agonist-induced Ca^{2+}-signalling patterns by NAADP in pancreatic acinar cells. *Nature* **398**, 74–76 (1999).

21. Gerasimenko, J. V. *et al.* NAADP mobilizes Ca^{2+} from a thapsigargin-sensitive store in the nuclear envelope by activating ryanodine receptors. *Journal of Cell Biology* **163**, 271–282 (2003).

22. Ogunbayo, O. A. *et al.* Cyclic Adenosine Diphosphate Ribose Activates Ryanodine Receptors, whereas NAADP Activates Two-pore Domain Channels. *Journal of Biological Chemistry* **286**, 9136–9140 (2011).

23. Calcraft, P. J. *et al.* NAADP mobilizes calcium from acidic organelles through two-pore channels. *Nature* **459**, 596–600 (2009).

24. Brailoiu, E. *et al.* Essential requirement for two-pore channel 1 in NAADP-mediated calcium signalling. *Journal of Cell Biology* **186**, 201–209 (2009).

25. Wang, X. *et al.* TPC Proteins Are Phosphoinositide- Activated Sodium-Selective Ion Channels in Endosomes and Lysosomes. *Cell* **151**, 372–383 (2012).

26. Zhang, X. *et al.* Agonist-specific voltage-dependent gating of lysosomal two-pore Na^{+} channels. *eLife* **8**, e51423 (2019).

27. Lin-Moshier, Y. *et al.* Photoaffinity Labeling of Nicotinic Acid Adenine Dinucleotide Phosphate (NAADP) Targets in Mammalian Cells*. *Journal of*

Biological Chemistry **287**, 2296–2307 (2012).

28. Walseth, T. F. *et al.* Photoaffinity Labeling of High Affinity Nicotinic Acid Adenine Dinucleotide Phosphate (NAADP)-Binding Proteins in Sea Urchin Egg. *Journal of Biological Chemistry* **287**, 2308–2315 (2012).

29. Roggenkamp, H. G. *et al.* HN1L/JPT2: A signalling protein that connects NAADP generation to Ca^{2+} microdomain formation. *Sci. Signal.* **14**, eabd5647 (2021).

30. Zhang, J., Guan, X., Shah, K. & Yan, J. Lsm12 is an NAADP receptor and a two-pore channel regulatory protein required for calcium mobilization from acidic organelles. *Nat Commun* **12**, 4739 (2021).

31. Zhu, M. X., Ma, J., Parrington, J., Galione, A. & Mark Evans, A. TPCs: Endolysosomal channels for Ca^{2+} mobilization from acidic organelles triggered by NAADP. *FEBS Letters* **584**, 1966–1974 (2010).

32. Catterall, W. A. Voltage-Gated Calcium Channels. *Cold Spring Harbor Perspectives in Biology* **3**, a003947–a003947 (2011).

33. Furukawa, T. Types of Voltage-Gated Calcium Channels: Molecular and Electrophysiological Views. *CHYR* **9**, 170–181 (2014).

34. Catterall, W. A. Signalling complexes of voltage-gated sodium and calcium channels. *Neuroscience Letters* **486**, 107–116 (2010).

35. Trebak, M. & Putney, J. W. ORAI Calcium Channels. *Physiology* **32**, 332–342 (2017).

36. Morgan, A. J., Martucci, L. L., Davis, L. C. & Galione, A. Two-pore channels:

going with the flows. *Biochemical Society Transactions* **50**, 1143–1155 (2022).

37. Ishibashi, K., Suzuki, M. & Imai, M. Molecular Cloning of a Novel Form (Two-Repeat) Protein Related to Voltage-Gated Sodium and Calcium Channels. *Biochemical and Biophysical Research Communications* **270**, 370–376 (2000).

38. Patel, S. *et al.* Electrophysiology of Endolysosomal Two-Pore Channels: A Current Account. *Cells* **11**, 2368 (2022).

39. Zong, X. *et al.* The two-pore channel TPCN2 mediates NAADP-dependent Ca^{2+}-release from lysosomal stores. *Pflugers Arch - Eur J Physiol* **458**, 891–899 (2009).

40. Brailoiu, E. *et al.* Essential requirement for two-pore channel 1 in NAADP-mediated calcium signalling. *Journal of Cell Biology* **186**, 201–209 (2009).

41. Calcraft, P. J. *et al.* NAADP mobilizes calcium from acidic organelles through two-pore channels. *Nature* **459**, 596–600 (2009).

42. Zhu, M. X., Evans, M. D., Ma, J., Parrington, J. & Galione, A. Two-pore channels for integrative Ca^{2+} signalling. *Communicative & Integrative Biology* **3**, 12–17 (2010).

43. Galione, A. *et al.* The acid test: the discovery of two-pore channels (TPCs) as NAADP-gated endolysosomal Ca^{2+} release channels. *Pflugers Arch - Eur J Physiol* **458**, 869–876 (2009).

44. Rahman, T. *et al.* Two-pore channels provide insight into the evolution of voltage-gated Ca^{2+} and Na^{+} channels. *Sci. Signal.* **7**, (2014).

45. Guo, J. *et al.* Structure of the voltage-gated two-pore channel TPC1 from

Arabidopsis thaliana. *Nature* **531**, 196–201 (2016).

46. She, J. *et al.* Structural insights into the voltage and phospholipid activation of the mammalian TPC1 channel. *Nature* **556**, 130–134 (2018).

47. She, J. *et al.* Structural mechanisms of phospholipid activation of the human TPC2 channel. *eLife* **8**, e45222 (2019).

48. Milenkovic, S. *et al.* The mechanism and energetics of a ligand-controlled hydrophobic gate in a mammalian two pore channel. *Phys. Chem. Chem. Phys.* **22**, 15664–15674 (2020).

49. Zhang, X. *et al.* Agonist-specific voltage-dependent gating of lysosomal two-pore Na^+ channels. *eLife* **8**, e51423 (2019).

50. Straub, I. *et al.* Citrus fruit and fabacea secondary metabolites potently and selectively block TRPM3: Identification of novel TRPM3 blockers. *Br J Pharmacol* **168**, 1835–1850 (2013).

51. Waheed, A. *et al.* Naringenin inhibits the growth of *Dictyostelium* and MDCK-derived cysts in a TRPP2 (polycystin-2)-dependent manner: Naringenin inhibits TRPP2-dependent growth. *Br J Pharmacol* **171**, 2659–2670 (2014).

52. Pafumi, I. *et al.* Naringenin Impairs Two-Pore Channel 2 Activity And Inhibits VEGF-Induced Angiogenesis. *Sci Rep* **7**, 5121 (2017).

53. Benkerrou, D. *et al.* A perspective on the modulation of plant and animal two pore channels (TPCs) by the flavonoid naringenin. *Biophysical Chemistry* **254**, 106246 (2019).

54. Gerndt, S. *et al.* Agonist-mediated switching of ion selectivity in TPC2 differentially promotes lysosomal function. *eLife* **9**, e54712 (2020).

55. Müller, M. *et al.* Gene editing and synthetically accessible inhibitors reveal role for TPC2 in HCC cell proliferation and tumor growth. *Cell Chem Biol* **28**, 1119-1131.e27 (2021).

56. Naylor, E. *et al.* Identification of a chemical probe for NAADP by virtual screening. *Nat Chem Biol* **5**, 220–226 (2009).

57. Sakurai, Y. *et al.* Two-pore channels control Ebola virus host cell entry and are drug targets for disease treatment. *Science* **347**, 995–998 (2015).

58. Davidson, S. M. *et al.* Inhibition of NAADP signalling on reperfusion protects the heart by preventing lethal calcium oscillations via two-pore channel 1 and opening of the mitochondrial permeability transition pore. *Cardiovasc Res* **108**, 357–366 (2015).

59. Clementi, N. *et al.* Naringenin is a powerful inhibitor of SARS-CoV-2 infection in vitro. *Pharmacol Res* **163**, 105255 (2021).

60. Ruas, M. *et al.* TPC1 has two variant isoforms, and their removal has different effects on endo-lysosomal functions compared to loss of TPC2. *Mol Cell Biol* **34**, 3981–3992 (2014).

61. Ruas, M. *et al.* Purified TPC isoforms form NAADP receptors with distinct roles for $Ca^{(2+)}$ signalling and endolysosomal trafficking. *Curr Biol* **20**, 703–709 (2010).

62. Fraldi, A., Klein, A. D., Medina, D. L. & Settembre, C. Brain Disorders Due to Lysosomal Dysfunction. *Annu. Rev. Neurosci.* **39**, 277–295 (2016).

63. Tong, B. C.-K. *et al.* Lysosomal TPCN (two pore segment channel) inhibition ameliorates beta-amyloid pathology and mitigates memory impairment in Alzheimer disease. *Autophagy* **18**, 624–642 (2022).

64. Kilpatrick, B. S. *et al.* Endoplasmic reticulum and lysosomal Ca^{2+} stores are remodelled in GBA1-linked Parkinson disease patient fibroblasts. *Cell Calcium* **59**, 12–20 (2016).

65. Hockey, L. N. *et al.* Dysregulation of lysosomal morphology by pathogenic LRRK2 is corrected by two-pore channel 2 inhibition. *Journal of Cell Science* jcs.164152 (2014) doi:10.1242/jcs.164152.

66. Favia, A. *et al.* NAADP-Dependent $Ca(^{2+})$ Signalling Controls Melanoma Progression, Metastatic Dissemination and Neoangiogenesis. *Sci Rep* **6**, 18925 (2016).

67. Nguyen, O. N. P. *et al.* Two-Pore Channel Function Is Crucial for the Migration of Invasive Cancer Cells. *Cancer Res* **77**, 1427–1438 (2017).

68. Netcharoensirisuk, P. *et al.* Flavonoids increase melanin production and reduce proliferation, migration and invasion of melanoma cells by blocking endolysosomal/melanosomal TPC2. *Sci Rep* **11**, 8515 (2021).

69. Wang, X. *et al.* TPC Proteins Are Phosphoinositide- Activated Sodium-Selective Ion Channels in Endosomes and Lysosomes. *Cell* **151**, 372–383 (2012).

70. Cang, C. *et al.* mTOR Regulates Lysosomal ATP-Sensitive Two-Pore Na^{+} Channels to Adapt to Metabolic State. *Cell* **152**, 778–790 (2013).

71. Patel, S. Function and dysfunction of two-pore channels. *Sci. Signal.* **8**, (2015).

72. Sulem, P. *et al.* Two newly identified genetic determinants of pigmentation in Europeans. *Nat Genet* **40**, 835–837 (2008).

73. Huang, X., Godfrey, T. E., Gooding, W. E., McCarty, K. S. & Gollin, S. M. Comprehensive genome and transcriptome analysis of the 11q13 amplicon in human oral cancer and synteny to the 7F5 amplicon in murine oral carcinoma. *Genes Chromosom. Cancer* **45**, 1058–1069 (2006).

74. Hu, M., Chen, J., Liu, S. & Xu, H. The Acid Gate in the Lysosome. *Autophagy* **19**, 1368–1370 (2023).

75. van Weely, S. *et al.* Role of pH in determining the cell-type-specific residual activity of glucocerebrosidase in type 1 Gaucher disease. *J. Clin. Invest.* **91**, 1167–1175 (1993).

76. Schneider, P. B. & Kennedy, E. P. Sphingomyelinase in normal human spleens and in spleens from subjects with Niemann-Pick disease. *J Lipid Res* **8**, 202–209 (1967).

77. Alexandre-Heymann, L., Mallone, R., Boitard, C., Scharfmann, R. & Larger, E. Structure and function of the exocrine pancreas in patients with type 1 diabetes. *Rev Endocr Metab Disord* **20**, 129–149 (2019).

78. Helmberger, T. K. & Manfredi, R. Diseases of the Pancreas. in *Diseases of the Abdomen and Pelvis 2018-2021: Diagnostic Imaging - IDKD Book* (eds. Hodler, J., Kubik-Huch, R. A. & von Schulthess, G. K.) (Springer, 2018).

79. Leung, P. S. Physiology of the Pancreas. in *The Renin-Angiotensin System: Current Research Progress in The Pancreas* vol. 690 13–27 (Springer Netherlands, 2010).

80. Patricia, J. J. & Dhamoon, A. S. Physiology, Digestion. in *StatPearls* (StatPearls Publishing, 2022).

81. Benjamin, O. & Lappin, S. L. Chronic Pancreatitis. in *StatPearls* (StatPearls Publishing, 2022).

82. Dolenšek, J., Rupnik, M. S. & Stožer, A. Structural similarities and differences between the human and the mouse pancreas. *Islets* **7**, e1024405 (2015).

83. Fish, E. M. & Burns, B. Physiology, Small Bowel. in *StatPearls* (StatPearls Publishing, 2022).

84. Leung, P. S. & Ip, S. P. Pancreatic acinar cell: Its role in acute pancreatitis. *The International Journal of Biochemistry & Cell Biology* **38**, 1024–1030 (2006).

85. Petersen, O. H. Stimulus-secretion coupling: cytoplasmic calcium signals and the control of ion channels in exocrine acinar cells. *The Journal of Physiology* **448**, 1–51 (1992).

86. Kasai, H., Li, Y. X. & Miyashita, Y. Subcellular distribution of Ca^{2+} release channels underlying Ca^{2+} waves and oscillations in exocrine pancreas. *Cell* **74**, 669–677 (1993).

87. Zeng, Q., Ou, L., Wang, W. & Guo, D.-Y. Gastrin, Cholecystokinin, Signalling, and Biological Activities in Cellular Processes. *Front. Endocrinol.* **11**, 112 (2020).

88. Chandra, R. & Liddle, R. A. Recent advances in the regulation of pancreatic secretion. *Curr Opin Gastroenterol* **30**, 490–494 (2014).

89. Wäsle, B. & Edwardson, J. M. The regulation of exocytosis in the pancreatic

acinar cell. *Cellular Signalling* **14**, 191–197 (2002).

90. Leung, P. S. The physiology of a local renin-angiotensin system in the pancreas: Physiology of the local pancreatic RAS. *The Journal of Physiology* **580**, 31–37 (2007).

91. Tsang, S. W., Cheng, C. H. K. & Leung, P. S. The role of the pancreatic renin-angiotensin system in acinar digestive enzyme secretion and in acute pancreatitis. *Regul Pept* **119**, 213–219 (2004).

92. Leung, P. & Carlsson, P. Tissue renin-angiotensin system: its expression, localization, regulation and potential role in the pancreas. *Journal of Molecular Endocrinology* **26**, 155–164 (2001).

93. Kasai, H. & Augustine, G. J. Cytosolic Ca^{2+} gradients triggering unidirectional fluid secretion from exocrine pancreas. *Nature* **348**, 735–738 (1990).

94. Yule, D. I., Ernst, S. A., Ohnishi, H. & Wojcikiewicz, R. J. Evidence that zymogen granules are not a physiologically relevant calcium pool. Defining the distribution of inositol 1,4,5-trisphosphate receptors in pancreatic acinar cells. *J Biol Chem* **272**, 9093–9098 (1997).

95. Kim, M. S. *et al.* Deletion of TRPC3 in Mice Reduces Store-Operated Ca^{2+} Influx and the Severity of Acute Pancreatitis. *Gastroenterology* **137**, 1509–1517 (2009).

96. Li, J., Zhou, R., Zhang, J. & Li, Z.-F. Calcium signalling of pancreatic acinar cells in the pathogenesis of pancreatitis. *WJG* **20**, 16146 (2014).

97. Schulz, I., Thévenod, F. & Dehlinger-Kremer, M. Modulation of intracellular free Ca^{2+} concentration by IP3-sensitive and IP3-insensitive nonmitochondrial Ca^{2+}

pools. *Cell Calcium* **10**, 325–336 (1989).

98. Gerasimenko, O. V., Gerasimenko, J. V., Belan, P. V. & Petersen, O. H. Inositol trisphosphate and cyclic ADP-ribose-mediated release of Ca^{2+} from single isolated pancreatic zymogen granules. *Cell* **84**, 473–480 (1996).

99. Murphy, J. A. *et al.* Direct activation of cytosolic Ca^{2+} signalling and enzyme secretion by cholecystokinin in human pancreatic acinar cells. *Gastroenterology* **135**, 632–641 (2008).

100. Cosker, F. *et al.* The Ecto-enzyme CD38 Is a Nicotinic Acid Adenine Dinucleotide Phosphate (NAADP) Synthase That Couples Receptor Activation to Ca^{2+} Mobilization from Lysosomes in Pancreatic Acinar Cells. *Journal of Biological Chemistry* **285**, 38251–38259 (2010).

101. Cancela, J. M., Churchill, G. C. & Galione, A. Coordination of agonist-induced Ca^{2+}-signalling patterns by NAADP in pancreatic acinar cells. *Nature* **398**, 74–76 (1999).

102. Guse, A. H. & Lee, H. C. NAADP: A Universal Ca $^{2+}$ Trigger. *Sci. Signal.* **1**, (2008).

103. Gerasimenko, J. V. *et al.* Both RyRs and TPCs are required for NAADP-induced intracellular Ca^{2+} release. *Cell Calcium* **58**, 237–245 (2015).

104. Kershaw, E. E. & Flier, J. S. Adipose Tissue as an Endocrine Organ. *The Journal of Clinical Endocrinology & Metabolism* **89**, 2548–2556 (2004).

105. Young, H. E. *et al.* Mesenchymal stem cells reside within the connective tissues of many organs. *Dev Dyn* **202**, 137–144 (1995).

106. Pairault, J. & Green, H. A study of the adipose conversion of suspended 3T3 cells by using glycerophosphate dehydrogenase as differentiation marker. *Proc Natl Acad Sci U S A* **76**, 5138–5142 (1979).

107. Yeh, W. C., Bierer, B. E. & McKnight, S. L. Rapamycin inhibits clonal expansion and adipogenic differentiation of 3T3-L1 cells. *Proc. Natl. Acad. Sci. U.S.A.* **92**, 11086–11090 (1995).

108. Tang, Q.-Q., Otto, T. C. & Lane, M. D. Mitotic clonal expansion: A synchronous process required for adipogenesis. *Proc. Natl. Acad. Sci. U.S.A.* **100**, 44–49 (2003).

109. Reichert, M. & Eick, D. Analysis of cell cycle arrest in adipocyte differentiation. *Oncogene* **18**, 459–466 (1999).

110. Lai, C.-S. *et al.* Bisdemethoxycurcumin Inhibits Adipogenesis in 3T3-L1 Preadipocytes and Suppresses Obesity in High-Fat Diet-Fed C57BL/6 Mice. *J. Agric. Food Chem.* **64**, 821–830 (2016).

111. Zhang, J.-W., Tang, Q.-Q., Vinson, C. & Lane, M. D. Dominant-negative C/EBP disrupts mitotic clonal expansion and differentiation of 3T3-L1 preadipocytes. *Proc Natl Acad Sci U S A* **101**, 43–47 (2004).

112. Lin, F. T. & Lane, M. D. CCAAT/enhancer binding protein alpha is sufficient to initiate the 3T3-L1 adipocyte differentiation program. *Proc. Natl. Acad. Sci. U.S.A.* **91**, 8757–8761 (1994).

113. Ossipow, V., Descombes, P. & Schibler, U. CCAAT/enhancer-binding protein mRNA is translated into multiple proteins with different transcription activation potentials. *Proc Natl Acad Sci U S A* **90**, 8219–8223 (1993).

114. Yeh, W. C., Cao, Z., Classon, M. & McKnight, S. L. Cascade regulation of terminal adipocyte differentiation by three members of the C/EBP family of leucine zipper proteins. *Genes Dev.* **9**, 168–181 (1995).

115. Li, X. *et al.* O-linked N-acetylglucosamine modification on CCAAT enhancer-binding protein beta: role during adipocyte differentiation. *J Biol Chem* **284**, 19248–19254 (2009).

116. Tanaka, T. Defective adipocyte differentiation in mice lacking the C/EBPbeta and/or C/EBPdelta gene. *The EMBO Journal* **16**, 7432–7443 (1997).

117. Tang, Q.-Q. *et al.* Sequential phosphorylation of CCAAT enhancer-binding protein beta by MAPK and glycogen synthase kinase 3beta is required for adipogenesis. *Proc Natl Acad Sci U S A* **102**, 9766–9771 (2005).

118. Li, X. *et al.* Role of cdk2 in the sequential phosphorylation/activation of C/EBPbeta during adipocyte differentiation. *Proc Natl Acad Sci U S A* **104**, 11597–11602 (2007).

119. Ron, D. & Habener, J. F. CHOP, a novel developmentally regulated nuclear protein that dimerizes with transcription factors C/EBP and LAP and functions as a dominant-negative inhibitor of gene transcription. *Genes Dev.* **6**, 439–453 (1992).

120. Schoonjans, K. *et al.* Induction of the Acyl-Coenzyme A Synthetase Gene by Fibrates and Fatty Acids Is Mediated by a Peroxisome Proliferator Response Element in the C Promoter. *Journal of Biological Chemistry* **270**, 19269–19276 (1995).

121. Tontonoz, P. *et al.* Adipocyte-specific transcription factor ARF6 is a heterodimeric complex of two nuclear hormone receptors, PPAR gamma and RXR alpha.

Nucleic Acids Res **22**, 5628–5634 (1994).

122. Tontonoz, P., Hu, E., Graves, R. A., Budavari, A. I. & Spiegelman, B. M. mPPAR gamma 2: tissue-specific regulator of an adipocyte enhancer. *Genes Dev.* **8**, 1224–1234 (1994).

123. Schoonjans, K. *et al.* PPARalpha and PPARgamma activators direct a distinct tissue-specific transcriptional response via a PPRE in the lipoprotein lipase gene. *EMBO J* **15**, 5336–5348 (1996).

124. Barak, Y. *et al.* PPARγ Is Required for Placental, Cardiac, and Adipose Tissue Development. *Molecular Cell* **4**, 585–595 (1999).

125. Kim, J. B., Wright, H. M., Wright, M. & Spiegelman, B. M. ADD1/SREBP1 activates PPARγ through the production of endogenous ligand. *Proc. Natl. Acad. Sci. U.S.A.* **95**, 4333–4337 (1998).

126. Reznikoff, C. A., Brankow, D. W. & Heidelberger, C. Establishment and characterization of a cloned line of C3H mouse embryo cells sensitive to postconfluence inhibition of division. *Cancer Res* **33**, 3231–3238 (1973).

127. Taylor, S. M. & Jones, P. A. Multiple new phenotypes induced in 10T1/2 and 3T3 cells treated with 5-azacytidine. *Cell* **17**, 771–779 (1979).

128. Pinney, D. F. & Emerson, C. P. 10T1/2 cells: an in vitro model for molecular genetic analysis of mesodermal determination and differentiation. *Environmental Health Perspectives* **80**, 221–227 (1989).

129. Davis, R. L., Weintraub, H. & Lassar, A. B. Expression of a single transfected cDNA converts fibroblasts to myoblasts. *Cell* **51**, 987–1000 (1987).

130. Sabourin, L. A. & Rudnicki, M. A. The molecular regulation of myogenesis: The molecular regulation of myogenesis. *Clinical Genetics* **57**, 16–25 (2000).

131. Hanamura, H. & Urist, M. R. Osteogenesis and chondrogenesis in transplants of Dunn and Ridgway osteosarcoma cell cultures. *Am J Pathol* **91**, 277–298 (1978).

132. Hogan, B. L. Bone morphogenetic proteins in development. *Current Opinion in Genetics & Development* **6**, 432–438 (1996).

133. Ahrens, M. *et al.* Expression of human bone morphogenetic proteins-2 or -4 in murine mesenchymal progenitor C3H10T1/2 cells induces differentiation into distinct mesenchymal cell lineages. *DNA Cell Biol* **12**, 871–880 (1993).

134. Wang, E. A., Israel, D. I., Kelly, S. & Luxenberg, D. P. Bone Morphogenetic Protein-2 Causes Commitment and Differentiation in C3Hl0T1/2 and 3T3 Cells. *Growth Factors* **9**, 57–71 (1993).

135. Shea, C. M., Edgar, C. M., Einhorn, T. A. & Gerstenfeld, L. C. BMP treatment of C3H10T1/2 mesenchymal stem cells induces both chondrogenesis and osteogenesis. *J. Cell. Biochem.* **90**, 1112–1127 (2003).

136. Date, T., Doiguchi, Y., Nobuta, M. & Shindo, H. Bone morphogenetic protein-2 induces differentiation of multipotent C3H10T1/2 cells into osteoblasts, chondrocytes, and adipocytes in vivo and in vitro. *Journal of Orthopaedic Science* **9**, 503–508 (2004).

137. Bowers, R. R., Kim, J. W., Otto, T. C. & Lane, M. D. Stable stem cell commitment to the adipocyte lineage by inhibition of DNA methylation: Role of the BMP-4 gene. *Proc. Natl. Acad. Sci. U.S.A.* **103**, 13022–13027 (2006).

138. McBeath, R., Pirone, D. M., Nelson, C. M., Bhadriraju, K. & Chen, C. S. Cell Shape, Cytoskeletal Tension, and RhoA Regulate Stem Cell Lineage Commitment. *Developmental Cell* **6**, 483–495 (2004).

139. Huang, H. *et al.* BMP signalling pathway is required for commitment of C3H10T1/2 pluripotent stem cells to the adipocyte lineage. *Proc Natl Acad Sci U S A* **106**, 12670–12675 (2009).

140. Wang, W. & Seale, P. Control of brown and beige fat development. *Nat Rev Mol Cell Biol* **17**, 691–702 (2016).

141. Davidson, S. M. *et al.* Progress in cardiac research: from rebooting cardiac regeneration to a complete cell atlas of the heart. *Cardiovascular Research* **117**, 2161–2174 (2021).

142. Ntambi, J. M. & Takova, T. Role of Ca^{2+} in the early stages of murine adipocyte differentiation as evidenced by calcium mobilizing agents. *Differentiation* **60**, 151–158 (1996).

143. Patel, Y. M. & Lane, M. D. Role of calpain in adipocyte differentiation. *Proc. Natl. Acad. Sci. U.S.A.* **96**, 1279–1284 (1999).

144. Zhang, F. *et al.* Calcium Supplementation Enhanced Adipogenesis and Improved Glucose Homeostasis Through Activation of Camkii and PI3K/Akt Signalling Pathway in Porcine Bone Marrow Mesenchymal Stem Cells (pBMSCs) and Mice Fed High Fat Diet (HFD). *Cell Physiol Biochem* **51**, 154–172 (2018).

145. Neal, J. W. & Clipstone, N. A. Calcineurin Mediates the Calcium-dependent Inhibition of Adipocyte Differentiation in 3T3-L1 Cells. *Journal of Biological Chemistry* **277**, 49776–49781 (2002).

146. Galione, A. & Chuang, K.-T. Pyridine Nucleotide Metabolites and Calcium Release from Intracellular Stores. in *Calcium Signalling* (ed. Islam, Md. S.) vol. 1131 371–394 (Springer International Publishing, 2020).

147. Galione, A. NAADP Receptors. *Cold Spring Harb Perspect Biol* **11**, a035071 (2019).

148. Galione, A. & Churchill, G. C. Interactions between calcium release pathways: multiple messengers and multiple stores. *Cell Calcium* **32**, 343–354 (2002).

149. Morgan, A. J. *et al.* Bidirectional Ca^{2+} signalling occurs between the endoplasmic reticulum and acidic organelles. *J Cell Biol* **200**, 789–805 (2013).

150. Brailoiu, E. *et al.* Essential requirement for two-pore channel 1 in NAADP-mediated calcium signalling. *J Cell Biol* **186**, 201–209 (2009).

151. Calcraft, P. J. *et al.* NAADP mobilizes calcium from acidic organelles through two-pore channels. *Nature* **459**, 596–600 (2009).

152. Ruas, M. *et al.* Purified TPC isoforms form NAADP receptors with distinct roles for $Ca(^{2+})$ signalling and endolysosomal trafficking. *Curr Biol* **20**, 703–709 (2010).

153. Jin, X. *et al.* Targeting Two-Pore Channels: Current Progress and Future Challenges. *Trends Pharmacol Sci* **41**, 582–594 (2020).

154. Ruas, M. *et al.* Expression of Ca^{2+}-permeable two-pore channels rescues NAADP signalling in TPC-deficient cells. *EMBO J* **34**, 1743–1758 (2015).

155. Brini, M., Ottolini, D., Calì, T. & Carafoli, E. Calcium in health and disease. *Met Ions Life Sci* **13**, 81–137 (2013).

156. Saurav, S., Tanwar, J., Ahuja, K. & Motiani, R. K. Dysregulation of host cell calcium signalling during viral infections: Emerging paradigm with high clinical relevance. *Molecular Aspects of Medicine* **81**, 101004 (2021).

157. Nieto-Torres, J. L. *et al.* Severe acute respiratory syndrome coronavirus E protein transports calcium ions and activates the NLRP3 inflammasome. *Virology* **485**, 330–339 (2015).

158. Broz, P. & Dixit, V. M. Inflammasomes: mechanism of assembly, regulation and signalling. *Nat Rev Immunol* **16**, 407–420 (2016).

159. Lee, G.-S. *et al.* The calcium-sensing receptor regulates the NLRP3 inflammasome through Ca^{2+} and cAMP. *Nature* **492**, 123–127 (2012).

160. Murakami, T. *et al.* Critical role for calcium mobilization in activation of the NLRP3 inflammasome. *Proc. Natl. Acad. Sci. U.S.A.* **109**, 11282–11287 (2012).

161. Lai, A. L. & Freed, J. H. SARS-CoV-2 Fusion Peptide has a Greater Membrane Perturbating Effect than SARS-CoV with Highly Specific Dependence on Ca^{2+}. *Journal of Molecular Biology* **433**, 166946 (2021).

162. Berlansky, S. *et al.* Calcium Signals during SARS-CoV-2 Infection: Assessing the Potential of Emerging Therapies. *Cells* **11**, 253 (2022).

163. Sakurai, Y. *et al.* Ebola virus. Two-pore channels control Ebola virus host cell entry and are drug targets for disease treatment. *Science* **347**, 995–998 (2015).

164. Simmons, J. A. *et al.* Ebolavirus Glycoprotein Directs Fusion through NPC1 $^{+}$ Endolysosomes. *J Virol* **90**, 605–610 (2016).

165. Penny, C. J. *et al.* Mining of Ebola virus entry inhibitors identifies approved drugs as two-pore channel pore blockers. *Biochim Biophys Acta Mol Cell Res* **1866**, 1151–1161 (2019).

166. Das, D. K. *et al.* Conformational changes in the Ebola virus membrane fusion machine induced by pH, Ca^{2+}, and receptor binding. *PLoS Biol* **18**, e3000626 (2020).

167. Gunaratne, G. S., Yang, Y., Li, F., Walseth, T. F. & Marchant, J. S. NAADP-dependent Ca^{2+} signalling regulates Middle East respiratory syndrome-coronavirus pseudovirus translocation through the endolysosomal system. *Cell Calcium* **75**, 30–41 (2018).

168. Ou, X. *et al.* Characterization of spike glycoprotein of SARS-CoV-2 on virus entry and its immune cross-reactivity with SARS-CoV. *Nat Commun* **11**, 1620 (2020).

169. Dobson, S. J., Mankouri, J. & Whitehouse, A. Identification of potassium and calcium channel inhibitors as modulators of polyomavirus endosomal trafficking. *Antiviral Research* **179**, 104819 (2020).

170. Ruas, M., Galione, A. & Parrington, J. Two-Pore Channels: Lessons from Mutant Mouse Models. *Messenger* **4**, 4–22 (2015).

171. De Sá, P. M., Richard, A. J., Hang, H. & Stephens, J. M. Transcriptional Regulation of Adipogenesis. in *Comprehensive Physiology* (ed. Terjung, R.) 635–674 (Wiley, 2017). doi:10.1002/cphy.c160022.

172. Sorisky, A. From Preadipocyte to Adipocyte: Differentiation-Directed Signals of Insulin from the Cell Surface to the Nucleus. *Critical Reviews in Clinical Laboratory Sciences* **36**, 1–34 (1999).

173. Siersbæk, R., Nielsen, R. & Mandrup, S. Transcriptional networks and chromatin remodeling controlling adipogenesis. *Trends in Endocrinology & Metabolism* **23**, 56–64 (2012).

174. Petri, S. & Meister, G. siRNA Design Principles and Off-Target Effects. in *Target Identification and Validation in Drug Discovery* (eds. Moll, J. & Colombo, R.) vol. 986 59–71 (Humana Press, 2013).

175. Visvanathan, R. *et al.* Critical review on conventional spectroscopic *α* -amylase activity detection methods: merits, demerits, and future prospects. *J Sci Food Agric* **100**, 2836–2847 (2020).

176. Lorentz, K. Routine α-Amylase Assay Using Protected 4-Nitrophenyl-1,4-α-d-maltoheptaoside and a Novel α-Glucosidase. *Clinical Chemistry* **46**, 644–649 (2000).

177. *http://www.oxfordbiobank.org.uk*. http://www.oxfordbiobank.org.uk.

178. Collins, J. M., Neville, M. J., Hoppa, M. B. & Frayn, K. N. De novo lipogenesis and stearoyl-CoA desaturase are coordinately regulated in the human adipocyte and protect against palmitate-induced cell injury. *J Biol Chem* **285**, 6044–6052 (2010).

179. Xu, J., Webb, I., Poole, P. & Huang, W. E. Label-Free Discrimination of Rhizobial Bacteroids and Mutants by Single-Cell Raman Microspectroscopy. *Anal. Chem.* **89**, 6336–6340 (2017).

180. Fayad, S., Morin, P. & Nehmé, R. Use of chromatographic and electrophoretic tools for assaying elastase, collagenase, hyaluronidase, and tyrosinase activity. *Journal of Chromatography A* **1529**, 1–28 (2017).

181. https://www.kegg.jp/.

182. http://geneontology.org/.

183. Prat Castro, S. *et al.* Neurodegenerative Lysosomal Storage Disorders: TPC2 Comes to the Rescue! *Cells* **11**, 2807 (2022).

184. Krogsaeter, E., Rosato, A. S. & Grimm, C. TRPMLs and TPCs: Targets for lysosomal storage and neurodegenerative disease therapy? *Cell Calcium* **103**, 102553 (2022).

185. Terrar, D. A. Endolysosomal calcium release and cardiac physiology. *Cell Calcium* **104**, 102565 (2022).

186. Halestrap, A. P. What is the mitochondrial permeability transition pore? *Journal of Molecular and Cellular Cardiology* **46**, 821–831 (2009).

187. Santucci, R., Sinibaldi, F., Cozza, P., Polticelli, F. & Fiorucci, L. Cytochrome c: An extreme multifunctional protein with a key role in cell fate. *International Journal of Biological Macromolecules* **136**, 1237–1246 (2019).

188. Pessoa, J. Live-cell visualization of cytochrome *c* : a tool to explore apoptosis. *Biochemical Society Transactions* **49**, 2903–2915 (2021).

189. Zhang, J., Guan, X., Shah, K. & Yan, J. Lsm12 is an NAADP receptor and a two-pore channel regulatory protein required for calcium mobilization from acidic organelles. *Nat Commun* **12**, 4739 (2021).

190. Sun, X., Zhang, J., Xiao, C. & Ge, Z. Expression profile and prognostic values of LSM family in skin cutaneous melanoma. *BMC Med Genomics* **15**, 238 (2022).

191. Taylor, S. M. & Jones, P. A. Multiple new phenotypes induced in and 3T3 cells treated with 5-azacytidine. *Cell* **17**, 771–779 (1979).

192. Lo Furno, D. *et al.* Decrease of apoptosis markers during adipogenic differentiation of mesenchymal stem cells from human adipose tissue. *Apoptosis* **18**, 578–588 (2013).

193. Thompson, W. J. CYCLIC NUCLEOTIDE PHOSPHODIESTERASES: PHARMACOLOGY, BIOCHEMISTRY AND FUNCTION. in *Intracellular Messengers* 287–313 (Elsevier, 1993). doi:10.1016/B978-0-08-042184-1.50015-9.

194. Siersbæk, R., Nielsen, R. & Mandrup, S. Transcriptional networks and chromatin remodeling controlling adipogenesis. *Trends in Endocrinology & Metabolism* **23**, 56–64 (2012).

195. Laurenza, A., Sutkowski, E. M. & Seamon, K. B. Forskolin: a specific stimulator of adenylyl cyclase or a diterpene with multiple sites of action? *Trends in Pharmacological Sciences* **10**, 442–447 (1989).

196. Haslam, R. J., Davidson, M. M. L. & Desjardins, J. V. Inhibition of adenylate cyclase by adenosine analogues in preparations of broken and intact human platelets. Evidence for the unidirectional control of platelet function by cyclic AMP. *Biochemical Journal* **176**, 83–95 (1978).

197. Cheng, X., Ji, Z., Tsalkova, T. & Mei, F. Epac and PKA: a tale of two intracellular cAMP receptors. *ABBS* **40**, 651–662 (2008).

198. Patel, Y. M. & Lane, M. D. Role of calpain in adipocyte differentiation. *Proc. Natl. Acad. Sci. U.S.A.* **96**, 1279–1284 (1999).

199. Moens, U. Multisite phosphorylation of the cAMP response element-binding protein CREB by a diversity of protein kinases. *Front Biosci* **12**, 1814–1832 (2007).

200. Tokumitsu, H. & Sakagami, H. Molecular Mechanisms Underlying Ca^{2+}/Calmodulin-Dependent Protein Kinase Kinase Signal Transduction. *IJMS* **23**, 11025 (2022).

201. Johnson, C. N. *et al.* The CaMKII inhibitor KN93-calmodulin interaction and implications for calmodulin tuning of NaV1.5 and RyR2 function. *Cell Calcium* **82**, 102063 (2019).

202. www.gtexportal.org.

203. Pulit, S. L. *et al.* Meta-analysis of genome-wide association studies for body fat distribution in 694 649 individuals of European ancestry. *Hum Mol Genet* **28**, 166–174 (2019).

204. (www.muther.ac.uk/).

205. Chen, M. & Zhang, X.-E. Construction and applications of SARS-CoV-2 pseudoviruses: a mini review. *Int. J. Biol. Sci.* **17**, 1574–1580 (2021).

206. Nagase, H., Visse, R. & Murphy, G. Structure and function of matrix metalloproteinases and TIMPs. *Cardiovascular Research* **69**, 562–573 (2006).

207. Brusa, S. *et al.* Circulating tissue inhibitor of metalloproteinases 1 (TIMP-1) at COVID-19 onset predicts severity status. *Front. Med.* **9**, 1034288 (2022).

208. Da Eira, D., Jani, S. & Ceddia, R. B. Obesogenic and Ketogenic Diets Distinctly

Regulate the SARS-CoV-2 Entry Proteins ACE2 and TMPRSS2 and the Renin-Angiotensin System in Rat Lung and Heart Tissues. *Nutrients* **13**, 3357 (2021).

209. Xiao, L., Sakagami, H. & Miwa, N. ACE2: The key Molecule for Understanding the Pathophysiology of Severe and Critical Conditions of COVID-19: Demon or Angel? *Viruses* **12**, 491 (2020).

210. Alenina, N. & Bader, M. ACE2 in Brain Physiology and Pathophysiology: Evidence from Transgenic Animal Models. *Neurochem Res* **44**, 1323–1329 (2019).

211. Patel, V. B., Zhong, J.-C., Grant, M. B. & Oudit, G. Y. Role of the ACE2/Angiotensin 1–7 Axis of the Renin–Angiotensin System in Heart Failure. *Circ Res* **118**, 1313–1326 (2016).

212. Grimm, C. *et al.* High susceptibility to fatty liver disease in two-pore channel 2-deficient mice. *Nat Commun* **5**, 4699 (2014).

Supplementary Materials.

A prognostic dynamic model applicable to infectious diseases providing easily visualized guides: a case study of COVID-19 in the UK.

Abstract

A reasonable prediction of infectious diseases' transmission process under different disease control strategies is an important reference point for policy makers. Here we established a dynamic transmission model via Python and realized comprehensive regulation of disease control measures. We classified government interventions into three categories and introduced three parameters as descriptions for the key points in disease control, these being intraregional growth rate, interregional communication rate, and detection rate of infectors. Our simulation predicts the infection by COVID-19 in the UK would be out of control in 73 days without any interventions; at the same time, herd immunity acquisition will begin from the epicentre. After we introduced government interventions, a single intervention is effective in disease control but at huge expense, while combined interventions would be more efficient, among which, enhancing detection number is crucial in the control strategy for COVID-19. In addition, we calculated requirements for the most effective vaccination strategy based on infection numbers in a real situation. Our model was programmed with iterative algorithms and visualized via cellular automata; it can be applied to similar epidemics in other regions if the basic parameters are inputted, and is able to synthetically mimic the effect of multiple factors in infectious disease control.

Introduction

Coronavirus disease (COVID-19) is an infectious respiratory syndrome caused by severe acute respiratory syndrome coronavirus 2 (SARS-CoV-2) and characterised by high overall human-to-human transmission potential.[1] The epidemic rapidly spread regionally at the end of 2019 and subsequent follow on caused a global pandemic and left the world facing a grave social as well as economic crisis.[2] Yet until an effective vaccination for all populations or specific medicine to combat COVID-19 is realised, it is likely that the possibility of a resurgence in contagion will exist so that disease control may become a normal part of everyday life.[3] In most world regions, the initial basic reproduction number (R_0) of COVID-19 was around 2.2-6.47.[4–9] In comparison, for MERS and SARS, the overall R_0 values were 0.47 and 0.95, respectively,[10] indicating that the transmissibility of COVID-19 is up to 10 times higher than that of previous coronavirus-caused infectious respiratory syndromes. Besides, the complex epidemiological properties of COVID-19 which include a long infectious period (infectiousness during the incubation period),[11] the existence of asymptomatic infectors who have a similar infection capacity (30%-60%),[10,12] a high overall self-healing rate (80%),[13] yet clinical severity in a minority of individuals,[14] have made the disease different from other antecedent epidemics. As such the unprecedentedly enormous infection scale and limited healthcare system capacity makes it challenging to formulate a proper disease control strategy in the COVID-19 era.

Over the last year, many previous epidemic studies have successfully provided insights for understanding, predicting and simulating the development of COVID-19 from multiple perspectives, such as calculating and predicting the evolving basic reproduction number;[6] quantitively predicting epidemiological

characteristics;[10,15] evaluating particular disease control measures such as social distancing,[16] controlling mobility;[17–20] analysing transmission dynamics in special populations such as the elderly, obese individuals, and diabetics;[3,21,22] evaluating various factors affecting disease transmission from urban health, meteorological and geo-environmental perspectives, such as water system, wind speed, and air pollution;[23–25] and also forecasting the subsequent impacts on the social environment and economy.[26,27] Epidemic models evaluating the effect and efficiency of disease control measures have provided good reference points for policy makers,[7,17,21,28,29] and in this study we aim to establish such a model to systematically simulate different measures, and with consideration of the special epidemiology characters. Most of the existing models follow the existing principle of susceptible-infectious-recovered (SIR);[9] here we established a novel infectious-hospitalized-self-heal (IHS) model, with application of iterative algorithm; asymptomatic infectors, hospitalized infectors, and self-heal infectors were analysed separately. This new principle makes our model more applicable to COVID-19 when considering its huge infection scale and its contagiosity in asymptomatic and pre-symptomatic infectors. With the involvement of some region-specific parameters such as population density, mobility, and hospital capacity, our model is also flexible for application to different global regions where COVID-19 is unlikely to follow an identical path.[15] With the platform of cellular automata, the simulation results are visualized and accessible. In this article, we simulate the development and recovery processes in the UK for 100 days since the first outbreak, and we discuss what is the optimum plan for early-stage disease control, and also the optimal vaccination strategy based on the updated conditions, which will effectively bring the pandemic to an end.

Results

Dynamic transmission model

In this article we summarised governmental interventions into three key strategies. First, the intraregional transmission probability has been lowered by protective measures or vaccinations, which aim to reduce the possibility of people contracting the disease.[24,30] Second, the mobility of the population has been reduced by government-level measures like city lock-down, border sealing, and compulsory stay-at-home policies.[19] Last but not least, healthcare system capacity has been enhanced to make sure as many patients as possible are quarantined and treated, while enhancement of detection capacity has aided early detection and immediate isolation.[31] We introduced interregional communication rate (c) to describe the coefficient of disease transmission between communities to take the impact of population mobility into consideration. Initial intraregional growth rate (m) was introduced to describe internal infection among communities, which indicates the influence of personal protection measures such as keeping a social distance and face covering. During the simulated transmission process, intraregional growth rate (m) changes continuously as it is affected by patient recovery and thus gain of immunity. Detection rate of infectors (k) was introduced to describe the possibility of an infector (including asymptomatic and pre-symptomatic individuals) being detected.

$$N_5(t+1) = \left[N_5(t) + \left(N_{2,4,6,8}(t) - 4N_5(t)\right) \cdot c + \left(N_{1,3,7,9}(t) - 4N_5(t)\right) \cdot b\right] \cdot \left(1 + m_5(t)\right) - H_5(t) - S_5(t)$$

$$H_5(t) = N_5(t - t_h) \cdot m_5(t - t_h) \cdot s \cdot (1 - 4c)^{t_h} + N_{2,4,6,8}(t - t_h) \cdot m_5(t - t_h) \cdot h \cdot c \cdot \frac{1 - (1 - 4c)^{t_h}}{4c} + N_{1,3,7,9}(t - t_h) \cdot h \cdot b \cdot \frac{1 - (1 - 4c)^{t_h}}{4c}$$

$$S_5(t) = N_5(t - t_s) \cdot m_5(t - t_s) \cdot s \cdot (1 - 4c)^{t_s} + m_5(t - t_s) \cdot s \cdot \left[N_{2,4,6,8}(t - t_s) \cdot c \cdot \frac{1 - (1 - 4c)^{t_s}}{4c} + N_{1,3,7,9}(t - t_s) \cdot b \cdot \frac{1 - (1 - 4c)^{t_s}}{4c} \right]$$

$$m_5(t + 1) = m \cdot \left(1 - \frac{1}{p_5} \cdot \left[\sum_{i=1}^{t} H_5(i) + \sum_{i=1}^{t} S_5(i) + N_5(t) \right] \right)$$

N: Daily infection number

c: Interregional communication coefficient (Travel rate over 15 km²)

m: Self-growth rate (Intraregional spreading coefficient)

h: General percentage of hospitalization (including death)

s: General percentage of self-healing

t_h: Average latent period

t_s: Average self-heal period

H: Daily hospitalization number

S: Daily self-healing number

p: Population

We use cellular automata as a platform of modelling; in cellular automata, cells are arranged as matrixes such as: $\begin{matrix}1 & 2 & 3\\ 4 & 5 & 6\\ 7 & 8 & 9\end{matrix}$; each cell represent a region and people tend to migrate between two adjacent cells (details provided in Supplementary Information, Figure S1). In the equations, N5(t^+1) is the daily infection number on day t^+1 in cell 5, which equals the daily infection number on day t added to the effect of migration in and out, then multiplied by the intraregional spreading coefficient, and subtraction of the day's number going to hospital and self-healing. The percentage of people who migrate out of a square cell from one side is *c*, therefore, the percentage of people who migrate out of a whole square is 4c.

Then we introduce controlled parameters to describe the situation after interventions (details in Methods). To be realistic, controlled interregional communication rate (c_c) and detection rate of infectors (k) are steady state values while controlled intraregional growth rate (m_c) is an initial value varying with the immunity acquisition number.

$$N_5(t+1) = \left\{\left[N_5(t) + \left(N_{2,4,6,8}(t) - 4N_5(t)\right)\cdot c_c + \left(N_{1,3,7,9}(t) - 4N_5(t)\right)\right.\right.$$
$$\left.\left.\cdot b\right]\cdot\left(1 + m_5(t)\right) - H_5(t) - S_5(t)\right\}\cdot(1-k)$$

$$H_5(t) = N_5(t-t_h)\cdot m_5(t-t_h)\cdot h\cdot(1-c_c)^{t_h} + N_{2,4,6,8}(t-t_h)$$
$$\cdot m_5(t-t_h)\cdot h\cdot c_c\cdot\frac{1-(1-c_c)^{t_h}}{c_c} + N_{1,3,7,9}(t-t_h)\cdot m_5(t$$
$$-t_h)\cdot h\cdot b\cdot\frac{1-(1-c_c)^{t_h}}{c_c}$$

$$S_5(t) = N_5(t-t_s)\cdot m_5(t-t_s)\cdot s\cdot(1-c_c)^{t_s} + N_{2,4,6,8}(t-t_s)\cdot m_5(t-t_s)$$
$$\cdot s\cdot c_c\cdot\frac{1-(1-c_c)^{t_s}}{c_c} + N_{1,3,7,9}(t-t_s)\cdot m_5(t-t_s)\cdot s\cdot b$$
$$\cdot\frac{1-(1-c_c)^{t_s}}{c_c}$$

$$m_5(t+1) = min\left\{m\cdot\left(1-\frac{1}{p_5}\cdot\left[\sum_{i=1}^{t}H_5(i)+\sum_{i=1}^{t}S_5(i)+N_5(t)\right]\right), m_c\right\}$$

m_c: Initial value of controlled intraregional growth rate

c_c: Controlled interregional communication rate

k: Detection rate of infectors

p: Regional population

We also take advantage of the definition of m which initially relies on R_0 and changes with the percentage of immunization to calculate the number of vaccinations required in disease control.

$$m_c = m\cdot\left(1-\frac{v_r+v+i}{p}\right)$$

v_r: Required vaccinations

v: Received vaccinations

i: Cumulative number of infections

Visualised transmission process of COVID-19 in the UK.

Videos showing the prognostic transmission process on the UK and London maps were generated by Python 3 based on our model (details shown in Methods and Supplementary Information). Here we present the infection curves (Figure 1) and visualised transmission maps (Figure 2) based on our simulation of the infection which starts with the initial daily infection number of each region in the UK on 4th March 2020.[32] Due to the limitations of the iterative algorithm, the earliest date we can start simulating disease control interventions is one day after the first self-heal period. Therefore, in the first 15 days (a self-heal period) of the simulation, we use the initial parameters according to COVID-19 epidemiological characteristics, the initial intraregional growth rate as 0.4,[4,33] the interregional travel rate as 0.1,[38,] and the detection rate of infectors as 0 (Table 1, data resources presented in Method). Without any governmental intervention, the accumulated infection number in 100 days may exceed 70% of the UK population (Figure 1A). Since the simulation was interrupted when the cumulative infection number exceeds the local population, COVID-19 transmission in the UK suspends on the 73rd day (Figure 1A). The daily infection scale will exceed 14.8 million people on the 60th day of domestic infection (Figure 1B), which accounts for nearly a quarter of the UK population.[34] When we look at the regional infection curves, we can see that the epidemic in London develops differently from other regions in that the infection in the former increases sharply during the 30th to 58th day, then decreases rapidly (Figure 1C). This indicates that, without interventions, the infection will first be eliminated in London while the conditions are still getting worse in other regions.

From the visualized transmission maps we can also see that when the infection peak is reached, the COVID-19 outbreak will ameliorate in the epicentre while it is still developing in surrounding regions (Figure 2A). As shown in the

screenshots of the simulation videos (Supplementary video files), the epidemic spreads from the epicentre to the periphery and surprisingly leaves the centre epiclean (Figure 2A). Here we also simulated the COVID-19 transmission process in London based on the initial daily infection number of each borough on 11th March (Figure 2B) which shows similar results.[32] Despite the fact that a second wave of infection may occur from the epicentre of the outbreak once again, the periphery may be the place hit by the epidemic more severely in a later period.

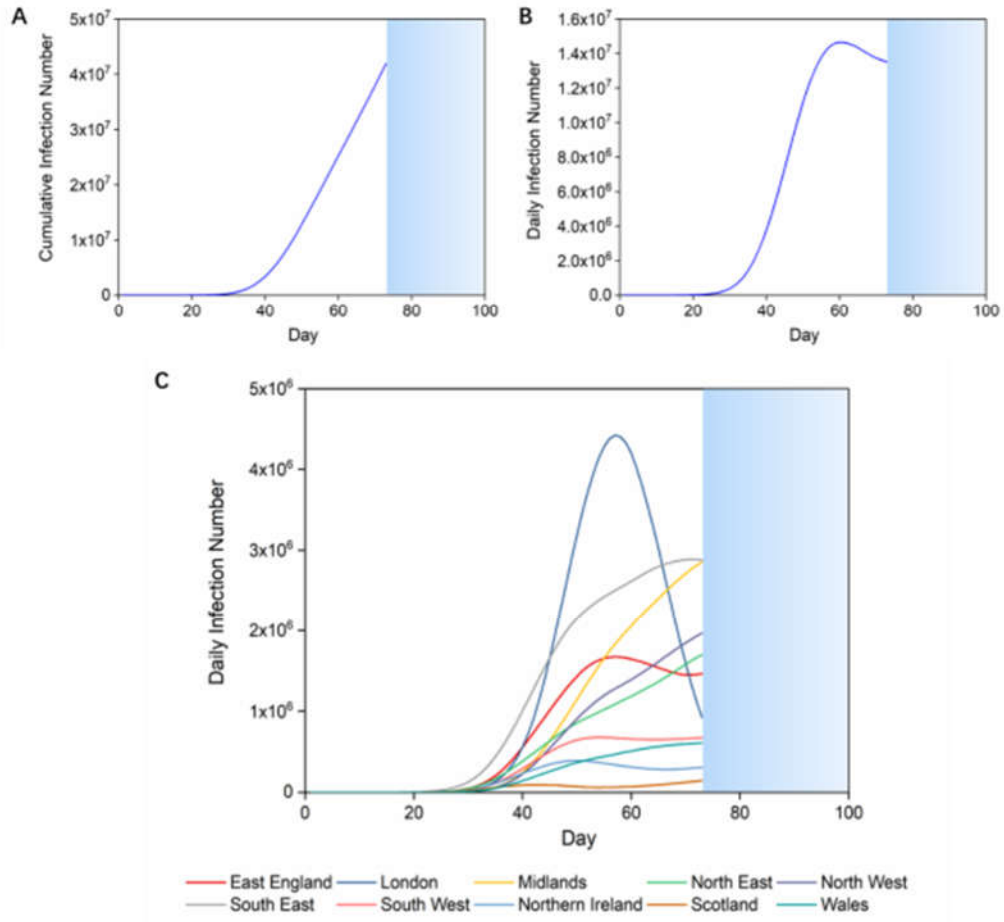


Figure 1. Infection curves without interventions in the UK. (A/B) The cumulative/daily infection curve without interventions in the UK. The simulation stops when cumulative infection number exceeds the regional population (blue sections).

(C) The daily infection curves for regions in the UK without interventions. The simulation stops when cumulative infection number exceeds the regional population.

COVID-19 can be brought under control by a single intervention at the early stage, but at huge expense.

We ran simulations to see how effective single interventions are in flattening the daily infection curves. When the controlled intraregional growth rate (m_c) was in the range of 0.05-0.4 ($0.75<R_0<6$, $m = R_0/15\ days$, details in the Methods),[14,35] the daily infection curve became progressively flatter with reduced m_c while the period of the epidemic became longer. When the controlled intraregional growth rate was lower than 0.1 ($R_0<1.5$), this was effective in controlling the propagation tendency, but a second infection wave was likely to occur. In addition, it was not possible to completely eliminate infection cases within a 100-day period by only controlling m_c, and the epidemic would thus last for a longer time (Figure 3A). When the controlled travel parameter (c_c) was in the range of 0.0125-0.01, the overall infection trends were downward but it was not possible to control the daily infection scale to an acceptable level (Figure 3B). An increasing detection rate of infectors (k) was capable of controlling the infection scales stably and efficiently as well as eliminating the infection within a short period (Figure 3C). The daily infection number dropped while k was enhanced, and as shown in Figure 3, controlling k brings better disease control results than controlling m_c and c_c. When k is as high as 0.175, it was possible to maintain the daily infection number curve at a flat level.

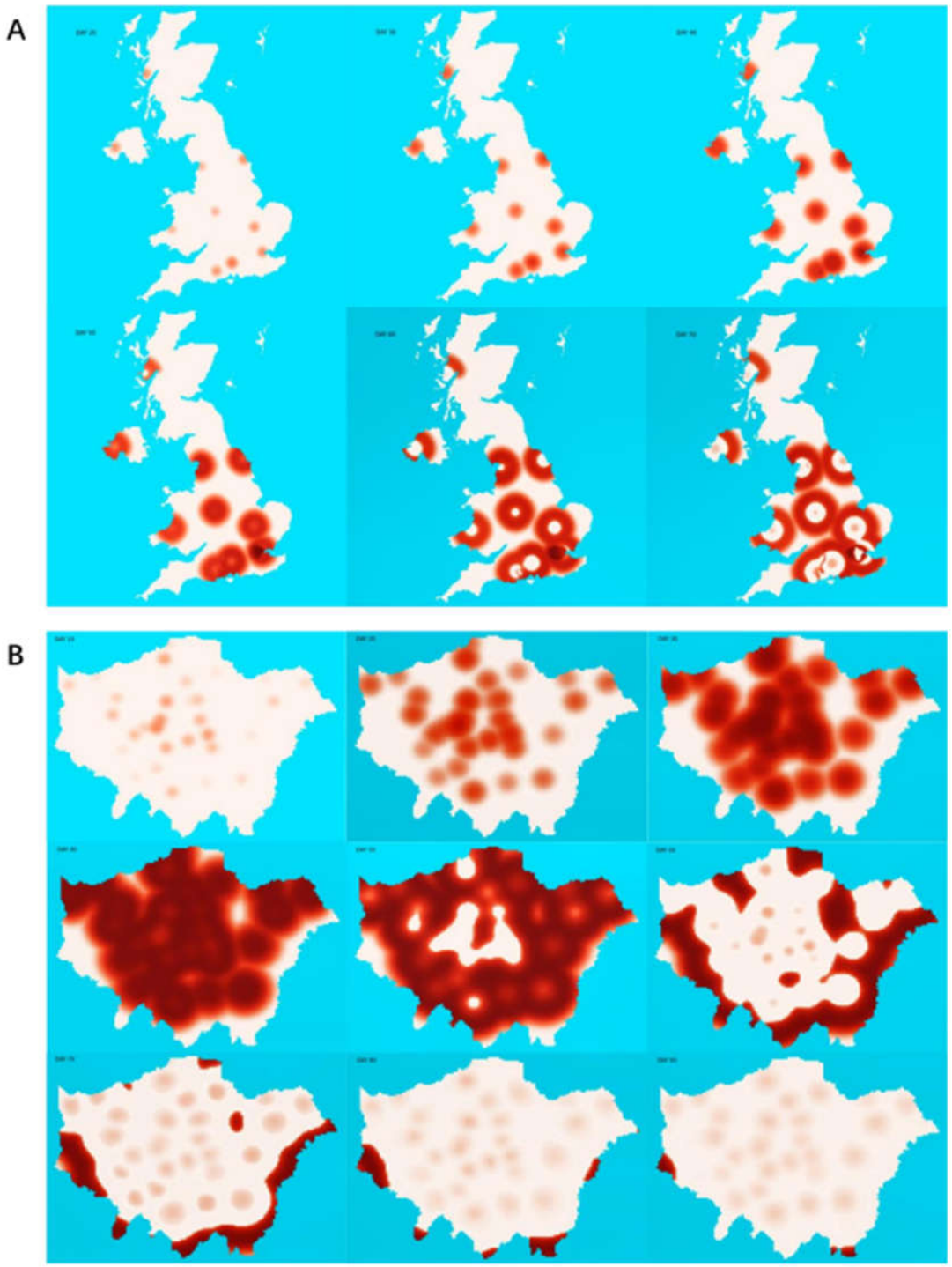


Figure 2. Visualized COVID-19 transmission without interventions in the UK and London. (A) Screenshots of visualized dynamic model of transmission in the UK from day 10 to day 60. The red saturation represents the severity of COVID-19. COVID-19

starts from a random spot in each region and spreads rapidly. In the outbreak centre, COVID-19 infection will reach a peak on day 50 and will be cleared on day 60 when it is out of control in the whole country. (B) Screenshots of visualized dynamic model of transmission in London from day 10 to day 90. (Day-by-day transmission videos were generated by Pythons 3 https://www.python.org using python package matplotlib https://matplotlib.org with initial maps from open-source software WordPress.org. Screenshots were generated by Windows10, more details were shown in Results——Technical details.)

Combined interventions will significantly enhance disease control efficiency.

As shown in Figure 3, with achievable single interventions, it is hard to contain the peak daily infection number to acceptable levels. Therefore, as shown in Figure 4, combined interventions were applied to seek for optimum disease control strategies.

The average length of the hospital stay for COVID-19 patients is 7 days.[36] The number of inpatient beds available for COVID-19 patients at the early stage of COVID-19 in the UK was around 6,000-7,000.[32] So the daily number of hospitalizations should be kept at around 1,000, which is a premise for our optimum disease control strategies. As shown in mobility trend reports by Apple Maps, the general mobility in the UK was reduced by 20%-50% during the COVID-19 lockdowns (Jan 2020 - Jan 2021).[37] Hence, we suppose the interregional communication rate in the UK to be reduced from 0.1 to 0.08~0.05,[38] indicating that 20%~32% people can travel beyond 2.5 miles every day. We selected several representative conditions to quantify the UK tier system, according to this tier system being based on the mobility trends and four-tier alert levels: m_c=0.17 (R_0=2.5), m_c=0.23 (R_0=3.5) and m_c=0.3 (R_0=4.5) with c_c in the range of 0.08-0.05 (Table 2);[32,35,37] then we ran simulations and found proper

relevant detection rates. The disease control process occurring systematically with three interventions was simulated and presented as transmission curves (Figure 4A/4B/4C). With regard to these different combinations of interventions, we can conclude that when tier 1, tier 2, and tier 3 lockdown measures are implemented, the detection rate should be ensured as 16%, 11.5% and 4.5%, and as shown in Figure 4D/4E/4F, the highest daily numbers to hospital (H) under these conditions do not exceed hospital capacity.

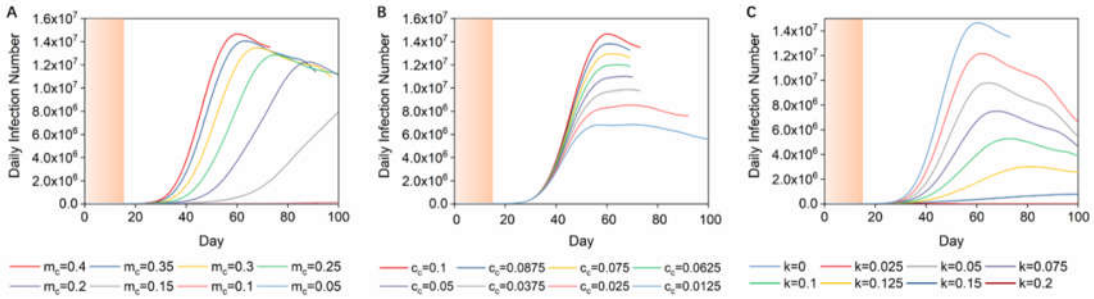


Figure 3. Impact of single interventions on daily infection curves. A) Daily infection curves for the UK with intraregional growth rates varying from 0.4 to 0.05. The orange section means no interventions were taken. B) Daily infection curves for the UK with interregional communication rates varying from 0.1 to 0.0125. C) Daily infection curves for the UK with detection rates of infectors varying from 0 to 0.2.

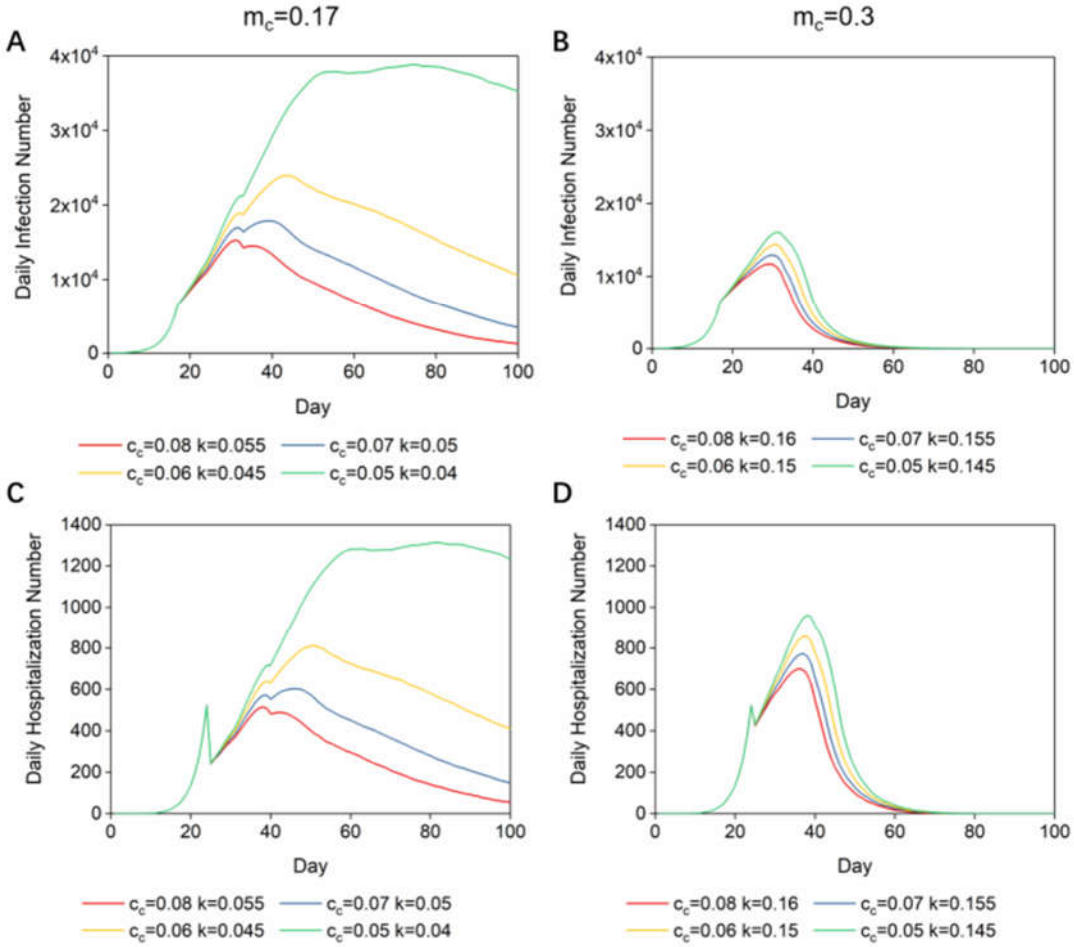


Figure 4. Daily infection curve and daily hospitalization curve with combined interventions. mc was in the range of 0.3-0.17 (initial R0 in the range of 4.5-2.5), and cc was in the range 0.05-0.08 (20%-32% people in the UK can travel over 2.5 miles a day). (A) Daily infection curves when mc was initially controlled at 0.17 (R0=2.5). (B) Daily infection curves when mc was initially controlled at 0.23 (R0=3.5). (C) Daily infection curves when mc was initially controlled at 0.3 (R0=4.5). (D) When mc=0.17, cc=0.08-0.05, the number to hospital can be controlled at around 1000 when k is controlled at 0.055-0.045. (E) When mc=0.23, cc=0.08-0.05, the number to hospital can be controlled at around 1000 when k is controlled at 0.105-0.12. (F) When mc=0.3, cc=0.08-0.05, the number to hospital can be controlled around 1000 when k is controlled at 0.16-0.145.

Application on calculating vaccination demand to end COVID-19.

A key current strategy to combat COVID-19 is the development of an effective vaccine. We thereby provided a method of calculating the required vaccination numbers based on this model. We started the simulation with the current infection number as an initial condition, and intraregional growth rate was influenced by vaccination and existing natural immunity. For example, in early January 2021, the average daily infection cases in the UK were around 35,000 with 3,300 being in London.[39] Considering the average infection period of COVID-19 which is 2-15 days,[10] we assume the real infection number in the UK and London to be 220,000 and 22,000,[32] accordingly. With the premise of controlling the pandemic within two months, and controlling m_c solely with vaccinations, we simulated the disease control process with the initial infection number of 220,000 and 22,000 in the UK and London and calculated the required number of vaccinations based on optimized m_c values (Figure 5) by applying the equation of $m_c = m \cdot \left(1 - \frac{v_r+v+i}{p}\right)$ as presented in earlier paragraph.[32] The required number of vaccinations should be not less than 43 million in the UK and 4.2 million in London (Table 2).

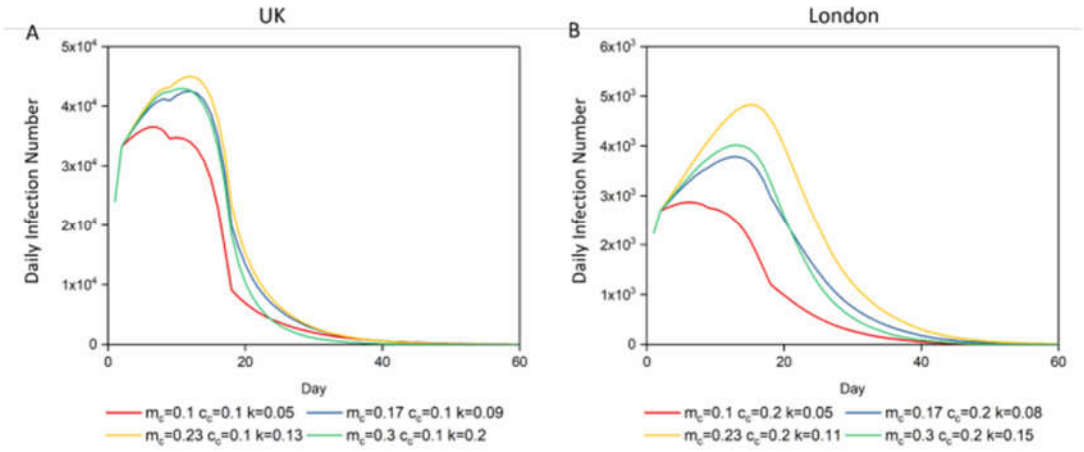


Figure 5. The daily infection curves at the recovery stage with proper control strategies. (A/B) Ideal daily infection curves starting with a daily infection number of 220,000 in the UK / 22,000 in London.

Discussion

As we have summarised, intervention measures have focused on three aspects: the intraregional spreading rate, detection rate of infectors and interregional communication rate. Long-duration intraregional lockdown effectively reduced the burden of the pandemic,[19,20] however, without cutting off the source of infection, the epidemic will not be eliminated in 100 days, even if the R_0 number is very low (Figure 3A). With respect to interregional communication rate, during the first round lockdown and associated impact on travel, 46% of driving, 62% of public transport and 33% walking trips were reduced on the days of lock-down compared to normal days.[37] However, the data shows the reduction started from 21st March,[37] when the cases of infection had already spread all over the country, therefore intraregional growth was already occurring at this point.[35] This also matches our simulation results and shows that it is difficult to control the infectious trend by simply reducing the travel parameter once the infection has spread to all regions. We then considered rate of detection and quarantine for infectors. In our simulation, around one fifth of infectors must be detected and strictly isolated even if they are in the latent period of the disease or asymptomatic and enhancing detection rate of infectors (k) is shown to be the most efficient intervention to bring the infection scale down as well as shorten the intervention period.

However, controlling all the single disease control parameters to ideal values is difficult in real conditions because of the special characteristics of COVID-19. Detection and isolation of early-stage and asymptomatic infectors is a big challenge for healthcare systems, and this was particularly the case with the unmatured detection technologies and limited resources in the first phase of the COVID-19 outbreak.[14,15] Therefore, our findings support the conclusion that

COVID-19 spread must be controlled by multiple combined strategies and as early as possible. The initial R_0 value was around 5.81 in the UK.[5] To reduce the social burden as well as balance the needs of the economy and disease control, we believe that controlling R_0 within the range of 2.5-4.5 and mobility reduced by 20%-32% (tier 1-3) is a reachable goal with proper control measures taken at the beginning of the period of interventions.[17,32,35] To keep the peak daily number of hospitalizations within acceptable levels when R_0 is immediately controlled at 2.5 (tier 3), with intermediate travelling control policy, 5% of infectors must be detected and quarantined. When R_0 is controlled at 4.5 (tier 1), our recommendation is that the detection rate should be enhanced to at least 20%.

Moreover, our simulation showed that the location at which the epidemic is most severe, was where the epidemic first began to disappear. So we suggest that instead of gathering all detection systems and resources to the main areas affected by the epidemic, distributing these resources to the peripheral regions will be a more efficient way to save resources and bring the epidemic under control. We also provided a potential method of calculating required vaccination numbers based on the actual infection number, for example, our simulation shows that when the infection number is around 220,000 in the UK and 22,000 in London,[32] the number of vaccinations in the UK should not be less than 45 million in the UK and 6.6 million in London.

Our study presents a few limitations due to model design as well as the nature of cellular automata. One such limitation is the inability of cellular automata to mimic long-distance migrations like trips by plane during the early stage of the disease transmission, as the chroma are only transmitted between two adjacent cells at a time. Another limitation is that mimicking the change of R_0 through the process of viral mutation is not applicable. Future optimizations of such modelling studies may focus on plugging evolving parameters relating to the

variations in the virus in the longer term.[40] It is also interesting to introduce new parameters to quantify other critical factors affecting epidemic transmission from social, economic, environmental, demographic, climatological, and health risk angles.[23,25,26,41]

Conclusion

This study is a prognostic analysis of infectious disease development on the strength of an infectious-hospitalized-self-heal (IHS) mathematic model with the first wave of COVID-19 in the UK as an example. The model is designed to match the epidemiological characteristics of infectious diseases with similarities to COVID-19, in particular ones with asymptomatic and pre-symptomatic infectivity.

Through Python designing, we realized the systematic regulation of intraregional growth rate, interregional communication coefficient, and detection rate. It is easy to evaluate the disease control effect by adjusting parameters and thus we can seek optimal solutions. In addition, we have found that to achieve better control effects in the mid-term of the epidemic, more attention should be paid to the surrounding areas of the epicentre. Moreover, our model can also be applied to estimate the quantity of vaccination demand based on realistic situations to provide guidance for vaccination production.

This model can also be applied in the future to predict the spread of similar infectious diseases in different regions. It only needs to input specific disease parameters in the system, such as incubation period, self-healing period, self-healing rate and so on. This model makes it convenient to quickly find the optimal solutions for comprehensive interventions and take action, which can be helpful in future public health decision-making to reduce morbidity and mortality.

Methods

Assumptions

1. The population is approximated to be constant and evenly distributed within each geographical region.
2. Death rate is counted as a part of the percentage of cases that are admitted to hospital.
3. Infected people are contagious constantly from the beginning to the end of the incubation period as well as during the illness stage.
4. All the population are at the same risk of infection.
5. All patients have contracted the virus through secondary infection; considering the high population mobility, primary infected patients, which represent a tiny percentage, are omitted.

Automata cell establishment

Cellular automata is a dynamic system that is discrete in time and space; it consists of a regular grid of cells, with each one being in a finite number of states. In our model, the disease transmission was described by partial cellular interaction leading to global change. A geographical region was regarded as a two-dimension network. To input this into cellular automata, each network was deemed as a cell while each cell stands for the location of a group of people. Pixels were downscaled to correspond to the area of the cells. Each cell was selected and separated according to the red, green, blue (RGB) value of the map (Supplementary Information Figure S1). Red colour chromatic value in the pixels represents the severity of the epidemic in the corresponding regions. The minimum value (r=0) means no cases while the maximum value (re=225) represents the population of the cell.

The epidemic information and regional population of each cell was set initially,[32,34] and the number of people who migrate each day depends on the interregional communication coefficient and the local population.

A method of convolution kernel was applied for calculation of migrating cases. We suppose that infection starts from one cell in each region, which was represented as a red dot on the map. The location of the dot was randomly chosen, and pseudo-random number seeds were fixed. The epidemic is assumed not to transmit to non-populated areas outside the coast where the infection number was forcibly set as zero.

Dynamical equations

Infectors go to the hospital and become self-healed only after the appearance of symptoms, and thus the precise number that go to hospital and self-heal depends on the infection number one period previously. The day's number to hospital in the cell is dependent on the daily infection number that occurred six days (the average latent period) previously in local and surrounding regions. Considering that some infectors will continually migrate between regions, these infectors who are infected 6 days previously and are currently in cell 5 can be divided into two parts: infectors who were infected in cell 5 and remained in cell 5 (local infectors who never migrate), and infectors who were infected in other cells and moved into the cell 5 in the previous 6 days. Assuming the number of infectors in cell 5 at the beginning is Y_5.

Day	Number of local infectors in cell *5*
1	$Y_5(1-4c)$

2	$Y_5(1-4c)^2$
3	$Y_5(1-4c)^3$
.	
T	$Y_5(1-4c)^t$

Therefore, replacing Y with the exact number of infectors, the daily number to hospital of local infectors in cell 5 on day t is calculated as

$$N_5(t-t_h)\cdot m_5(t-t_h)\cdot h\cdot(1-4c)^{t_h}$$

Next, we consider the number of infectors who move into cell *5*. Suppose the number of people in group *Y* in adjacent cells of Y_5 are Y_2, Y_4, Y_6, Y_8, and add up to $Y_{2,4,6,8}$. Since each cell has only one side in contact with cell *5*, on the first day the number of people in group *Y* who move into cell *5* is $Y_{2,4,6,8}\cdot c$. Meanwhile people also move out from cell *5*, so on the second day the number of people in group *Y* who move into cell *5* is $Y_{2,4,6,8}\cdot c\cdot(1-4c)$. The rest can be calculated in the same manner.

Day	Number of people in group *Y* who move into cell *5*
1	$Y_{2,4,6,8}\cdot c$
2	$Y_{2,4,6,8}\cdot c(1-4c)$
3	$Y_{2,4,6,8}\cdot c(1-4c)^2$

.

t $Y_{2,4,6,8} \cdot c(1-4c)^{t-1}$

Hence, the total number of people in group *Y* who moved into cell *5* on day *t* is

$$\sum_{i=0}^{t-1} Y_{2,4,6,8} \cdot c(1-4c)^{i} = Y_{2,4,6,8} \cdot c \cdot \frac{1-(1-4c)^{t}}{1-(1-4c)} = Y_{2,4,6,8} \cdot c \cdot \frac{1-(1-4c)^{t}}{4c}$$

If we replace *Y* with the exact number of infectors, the daily number of infectors who move into hospital in cell 5 on day t is calculated as

$$N_{2,4,6,8}(t-t_h) \cdot m_5(t-t_h) \cdot h \cdot c \cdot \frac{1-(1-4c)^{t}}{4c}$$

Therefore, the daily increase in the number of hospitalizations in cell *5* on day *t* is

$$H_5(t) = N_5(t-t_h) \cdot m_5(t-t_h) \cdot s \cdot (1-4c)^{t_h} + N_{2,4,6,8}(t-t_h) \cdot m_5(t - t_h) \cdot h \cdot c \cdot \frac{1-(1-4c)^{t_h}}{4c}$$

In a similar way, the daily increase in the number that self-heal (S) is calculated as

$$S_5(t) = N_5(t-t_s) \cdot m_5(t-t_s) \cdot s \cdot (1-4c)^{t_s} + N_{2,4,6,8}(t-t_s) \cdot m_5(t-t_s) \cdot s \cdot c \cdot \frac{1-(1-4c)^{t_s}}{4c}$$

Data sources

We used an initial spreading coefficient to explain the daily percentage increase;

in the UK the initial R_0 value was 5.81,[4,5] the infection period (including incubation period) was 15 days, and the incidence number doubled every 1.8 to 2.8 days (Table 1). So the value of the initial growth rate can be calculated as 0.4 ($m = R_0/15\ days$).

We set 16183 pixels, for the areas of the UK. Therefore, on the UK map, each pixel represents a 15 km^2 geographic area, and people who travel over a 4 km (2.5 mile) straight-line distance are considered as migrants. The percentage of people migrating between cells in the UK is around 40% as roughly estimated based on available worldwide and domestic travel and transport statistics (Table 1).[38,42] Since there are four directions in which people in one square cell can migrate, the number will be divided by 4, and the travel parameter was estimated to be 0.1, standing for 10% people in one cell migrating between certain two adjacent cells every day (Table 1).

The general percentage of hospitalization means the possibility of infectors being accepted to the hospital and thus strictly isolated. We consulted the cumulative death rate which is estimated at 15.4%, and the number of beds occupied by confirmed COVID-19 patients according to the NHS statistics in July, which showed that 2,000 beds were occupied by COVID-19 patients.[43] Moreover, in early April the number of hospitalizations was estimated at around 7,000-8,000.[44] Considering there to be 200% undetected cases, as the number of undetected patients is estimated to be more than two times that of the confirmed patients, the percentage to hospital including death rate is 20% (Table 1).[45]

Since the illness period is estimated at 15 days, the controlled spreading coefficient can be calculated as $m = R_0/15\ days$, which means the average number of people who can contract COVID-19 from one patient in one day during his/her illness period.[46]

The detection rate of infectors stands for the possibility of an infector being detected as well as isolated. For instance, if the healthcare system provides no detection service, the detection rate of infectors is equal to 0. If the healthcare system provides enough detection for all patients with severe symptoms and immediately isolates them, the detection rate of infectors is equal to the rate of occurrence of severe symptoms (13.8%).[46] If the healthcare system provides general, extensive and compulsive detection services for all citizens, the detection rate of infectors will be close to 1.

An approximate validation of the accuracy of the model was based on the early statistics from the UK government, although this was hard to do in practice because the real transmission dynamic and infection scale were difficult to determine at the early stage of the pandemic (Supplementary Table S1).

Technical details

All source codes are generated by Python 3 (https://www.python.org) and Jupyter Notebook (jupyter.org). Videos are produced by python package matplotlib (https://matplotlib.org) using "Animation" Class. Initial UK and London maps were download from open-source software WordPress.org which was released under a General Public License (GPLv2) from the Free Software Foundation,[47,48] and are pre-processed by python package scikit-image (https://scikit-image.org) so that all boundaries between regions/boroughs are smoother for mimicking population migration. All codes are publicly available on GitHub (https://github.com/daweiliucsd/Cov19-model). In order to run all example codes, prebuilt Python distributions such as Anaconda are strongly recommended.

References

1. WHO. Report of the WHO-China Joint Mission on Coronavirus Disease 2019 (COVID-19). (2020).

2. WHO. Archived: WHO Timeline - COVID-19. https://www.who.int/news-room/detail/27-04-2020-who-timeline---covid-19.

3. Kissler, S. M., Tedijanto, C., Goldstein, E., Grad, Y. H. & Lipsitch, M. Projecting the transmission dynamics of SARS-CoV-2 through the postpandemic period. *Science* eabb5793 (2020) doi:10.1126/science.abb5793.

4. Sanche, S. *et al.* High Contagiousness and Rapid Spread of Severe Acute Respiratory Syndrome Coronavirus 2. *Emerg. Infect. Dis.* **26**, (2020).

5. Dropkin, G. COVID-19 UK Lockdown Forecasts and R0. *Front. Public Health* **8**, 256 (2020).

6. Chintalapudi, N., Battineni, G., Sagaro, G. G. & Amenta, F. COVID-19 outbreak reproduction number estimations and forecasting in Marche, Italy. *Int. J. Infect. Dis.* **96**, 327–333 (2020).

7. Koo, J. R. *et al.* Interventions to mitigate early spread of SARS-CoV-2 in Singapore: a modelling study. *Lancet Infect. Dis.* **20**, 678–688 (2020).

8. Wu, J. T., Leung, K. & Leung, G. M. Nowcasting and forecasting the potential domestic and international spread of the 2019-nCoV outbreak originating in Wuhan, China: a modelling study. *The Lancet* **395**, 689–697 (2020).

9. Gatto, M. *et al.* Spread and dynamics of the COVID-19 epidemic in Italy: Effects of emergency containment measures. *Proc. Natl. Acad. Sci.* **117**, 10484–10491 (2020).

10. Cevik, M. *et al.* SARS-CoV-2, SARS-CoV, and MERS-CoV viral load dynamics, duration of viral shedding, and infectiousness: a systematic review and meta-analysis. *Lancet Microbe* **2**, e13–e22 (2021).

11. Linton, N. M. *et al.* Incubation Period and Other Epidemiological Characteristics of 2019 Novel Coronavirus Infections with Right Truncation: A Statistical Analysis of Publicly Available Case Data. *J. Clin. Med.* **9**, 538 (2020).

12. Kwok, K. O., Lai, F., Wei, W. I., Wong, S. Y. S. & Tang, J. W. T. Herd immunity – estimating the level required to halt the COVID-19 epidemics in affected countries. *J. Infect.* **80**, e32–e33 (2020).

13. Wilder-Smith, A., Chiew, C. J. & Lee, V. J. Can we contain the COVID-19 outbreak with the same measures as for SARS? *Lancet Infect. Dis.* **20**, e102–e107 (2020).

14. Stawicki, S. *et al.* The 2019–2020 novel coronavirus (severe acute respiratory syndrome coronavirus 2) pandemic: A joint american college of academic international medicine-world academic council of emergency medicine multidisciplinary COVID-19 working group consensus paper. *J. Glob. Infect. Dis.* **12**, 47 (2020).

15. Jewell, N. P., Lewnard, J. A. & Jewell, B. L. Predictive Mathematical Models of the COVID-19 Pandemic: Underlying Principles and Value of Projections. *JAMA* **323**, 1893 (2020).

16. Farboodi, M., Jarosch, G. & Shimer, R. *Internal and External Effects of Social Distancing in a Pandemic*. w27059 http://www.nber.org/papers/w27059.pdf (2020) doi:10.3386/w27059.

17. Li, Y. *et al.* The Impact of Policy Measures on Human Mobility, COVID-19 Cases, and Mortality in the US: A Spatiotemporal Perspective. *Int. J. Environ. Res. Public. Health* **18**, 996 (2021).

18. Chang, S. *et al.* Mobility network models of COVID-19 explain inequities and inform reopening. *Nature* **589**, 82–87 (2021).

19. Imperial College COVID-19 Response Team *et al.* Estimating the effects of non-pharmaceutical interventions on COVID-19 in Europe. *Nature* **584**, 257–261 (2020).

20. Islam, N. *et al.* Physical distancing interventions and incidence of coronavirus disease 2019: natural experiment in 149 countries. *BMJ* m2743 (2020) doi:10.1136/bmj.m2743.

21. Kucharski, A. J. *et al.* Early dynamics of transmission and control of COVID-19: a mathematical modelling study. *Lancet Infect. Dis.* **20**, 553–558 (2020).

22. CMMID COVID-19 working group *et al.* Age-dependent effects in the transmission and control of COVID-19 epidemics. *Nat. Med.* (2020) doi:10.1038/s41591-020-0962-9.

23. Coccia, M. How do low wind speeds and high levels of air pollution support the spread of COVID-19? *Atmospheric Pollut. Res.* (2020) doi:10.1016/j.apr.2020.10.002.

24. Gormley, M., Aspray, T. J. & Kelly, D. A. COVID-19: mitigating transmission via wastewater plumbing systems. *Lancet Glob. Health* **8**, e643 (2020).

25. Coccia, M. An index to quantify environmental risk of exposure to future

epidemics of the COVID-19 and similar viral agents: Theory and practice. *Environ. Res.* **191**, 110155 (2020).

26. Yang, C. *et al.* Taking the pulse of COVID-19: a spatiotemporal perspective. *Int. J. Digit. Earth* **13**, 1186–1211 (2020).

27. Wolf M. The risks of lifting lockdowns prematurely are very large. *Financial Times*.

28. Kraemer, M. U. G. *et al.* The effect of human mobility and control measures on the COVID-19 epidemic in China. *Science* **368**, 493–497 (2020).

29. Prem, K. *et al.* The effect of control strategies to reduce social mixing on outcomes of the COVID-19 epidemic in Wuhan, China: a modelling study. *Lancet Public Health* **5**, e261–e270 (2020).

30. Greenhalgh, T., Schmid, M. B., Czypionka, T., Bassler, D. & Gruer, L. Face masks for the public during the covid-19 crisis. *BMJ* m1435 (2020) doi:10.1136/bmj.m1435.

31. Peck, K. R. Early diagnosis and rapid isolation: response to COVID-19 outbreak in Korea. *Clin. Microbiol. Infect.* S1198743X20302330 (2020) doi:10.1016/j.cmi.2020.04.025.

32. https://coronavirus.data.gov.uk/. Coronavirus (COVID-19) in the UK.

33. Tang, B. *et al.* Estimation of the Transmission Risk of 2019-nCov and Its Implication for Public Health Interventions. *SSRN Electron. J.* (2020) doi:10.2139/ssrn.3525558.

34. *Population of England in 2019, by region*. https://www.statista.com/statistics/294681/population-england-united-kingdom-uk-regional/.

35. Hale, T., Petherick, A., Phillips, T. & Webster, S. Variation in government responses to COVID-19. *Version 2.0. Blavatnik School of Government Working Paper*.

36. Rees, E. M. *et al. COVID-19 length of hospital stay: a systematic review and data synthesis*. http://medrxiv.org/lookup/doi/10.1101/2020.04.30.20084780 (2020) doi:10.1101/2020.04.30.20084780.

37. APPLE MAPS. Mobility Trends Reports. https://www.apple.com/covid19/mobility.

38. UK.GOV. Transport Statistics Great Britain: 2019. https://www.gov.uk/government/statistics/transport-statistics-great-britain-2019.

39. Coronavirus (COVID-19) Cases. https://data.london.gov.uk/dataset/coronavirus--covid-19--cases.

40. Volz, E. *et al.* Evaluating the Effects of SARS-CoV-2 Spike Mutation D614G on Transmissibility and Pathogenicity. *Cell* **184**, 64-75.e11 (2021).

41. Coccia, M. Factors determining the diffusion of COVID-19 and suggested strategy to prevent future accelerated viral infectivity similar to COVID. *Sci. Total Environ.* **729**, 138474 (2020).

42. London Datastore. Coronavirus (COVID-19) Mobility Report. https://data.london.gov.uk/dataset/coronavirus-covid-19-mobility-report.

43. NHS. Bed Availability and Occupancy. https://www.england.nhs.uk/statistics/statistical-work-areas/bed-availability-and-occupancy/.

44. NHS. COVID-19 Hospital Activity. https://www.england.nhs.uk/statistics/statistical-work-areas/covid-19-hospital-activity/.

45. Böhning, D., Rocchetti, I., Maruotti, A. & Holling, H. Estimating the undetected infections in the Covid-19 outbreak by harnessing capture–recapture methods. *Int. J. Infect. Dis.* **97**, 197–201 (2020).

46. Chen, J. *et al.* Clinical progression of patients with COVID-19 in Shanghai, China. *J. Infect.* **80**, e1–e6 (2020).

47. GNU General Public License, version 2.

48. *Interactive UK Map*. https://wordpress.org/plugins/interactive-uk-map/.